

Johannes Gutenberg-Universität Mainz
Fachbereich 08 für Physik, Mathematik und Informatik

The Impact of Ice Crystals on Radiative Forcing and Remote Sensing of Arctic Boundary-Layer Mixed-Phase Clouds

DISSERTATION

zur Erlangung des akademischen Grades

Doktor der Naturwissenschaften

(Dr. rer. nat.)

vorgelegt von

Dipl.-Met. André Ehrlich

geboren am 3. Mai 1980 in Köthen/Anhalt

Mainz, den 2. März 2009

1. Gutachter:
2. Gutachter:

Datum der mündlichen Prüfung: 13. Mai 2009

Summary

This PhD thesis is embedded into the Arctic Study of Tropospheric Aerosol, Clouds and Radiation (ASTAR) and investigates the radiative transfer through Arctic boundary-layer mixed-phase (ABM) clouds. For this purpose airborne spectral solar radiation measurements and simulations of the solar and thermal infrared radiative transfer have been performed. This work reports on measurements with the Spectral Modular Airborne Radiation measurement system (SMART-Albedometer) conducted in the framework of ASTAR in April 2007 close to Svalbard. For ASTAR the SMART-Albedometer was extended to measure spectral radiance. The development and calibration of the radiance measurements are described in this work. In combination with in situ measurements of cloud particle properties provided by the Laboratoire de Météorologie Physique (LaMP) and simultaneous airborne lidar measurements by the Alfred Wegener Institute for Polar and Marine Research (AWI) ABM clouds were sampled. The SMART-Albedometer measurements were used to retrieve the cloud thermodynamic phase by three different approaches. A comparison of these results with the in situ and lidar measurements is presented in two case studies. Beside the dominating mixed-phase clouds pure ice clouds were found in cloud gaps and at the edge of a large cloud field. Furthermore the vertical distribution of ice crystals within ABM clouds was investigated. It was found that ice crystals at cloud top are necessary to describe the observed SMART-Albedometer measurements. The impact of ice crystals on the radiative forcing of ABM clouds is investigated by extensive radiative transfer simulations. The solar and net radiative forcing was found to depend on the ice crystal size, shape and the mixing ratio of ice crystals and liquid water droplets.

Zusammenfassung

Diese Dissertation ist innerhalb eines Teilprojekts des Internationalen Polarjahres (IPY) namens ASTAR (Arctic Study of Tropospheric Aerosol, Clouds and Radiation) entstanden. Dabei wurde der Strahlungstransfer in arktischen Mischphasenwolken untersucht. Zu diesem Zweck wurden flugzeuggetragenen Messungen der spektral aufgelösten solaren Strahlung durchgeführt. Desweiteren wurde der solare sowie langwellige Strahlungstransfer mittels Modellen simuliert. In dieser Arbeit werden Messungen mit dem SMART-Albedometer (Spectral Modular Airborne Radiation measurement system) präsentiert, die im Rahmen von ASTAR im April 2007 in der Umgebung von Spitzbergen aufgezeichnet wurden. Für ASTAR wurde das SMART-Albedometer für Messungen der spektralen Strahlungsflussdichte (Radianz) erweitert. Die Entwicklung und Kalibrierungen der Radianzmessungen sind in der Arbeit beschrieben. In Kombination mit In-Situ-Messungen der Eigenschaften von Wolkenpartikeln, zur Verfügung gestellt durch das Laboratoire de Météorologie Physique (LAMP), und gleichzeitigen flugzeuggetragenen Lidarmessungen durch das Alfred-Wegener Institut for Polar- und Meeresforschung (AWI) wurden arktische Grenzschichtwolken untersucht. Die Messungen des SMART-Albedometer wurden zur Identifizierung der Wolkenphase (Eis, flüssig Wasser) genutzt. Für diesen Zweck wurden drei verschiedenen Methoden entwickelt und auf die Messungen angewandt. Für zwei Fallstudien werden Vergleiche zwischen den Ergebnissen dieser Methoden und der In-Situ- bzw. Lidarmessungen präsentiert. Neben dem vorherrschenden Mischphasenwolken wurden reine Eiswolken im Bereich von Wolkenlücken und am Rand eines größeren Wolkenfeldes identifiziert. Weiterhin wurde die vertikale Verteilung von Eiskristallen in arktischen Mischphasenwolken untersucht. Es wird gezeigt, dass das Vorhandensein von Eiskristallen nahe der Wolkenoberkante notwendig ist, um die beobachteten Strahlungsmessungen durch Simulationen zu reproduzieren. Der Einfluss der Eiskristalle auf den Strahlungsantrieb dieser Wolken wurde mittels umfassenden Strahlungsübertragungsrechnungen ermittelt. Es wird gezeigt, dass der solare und netto Strahlungsantrieb von dem Mischungsverhältnis von Eiskristallen und Wassertröpfchen abhängt. Dieser Zusammenhang wird zusätzlich durch die Größe und Form der Eiskristalle beeinflusst.

Contents

1	Introduction of Arctic Boundary-Layer Mixed-Phase Clouds	1
1.1	Importance	1
1.2	Formation Mechanism	3
2	Motivation and Objectives	7
2.1	Remote Sensing	7
2.2	Radiative Budget	8
3	Radiative Transfer in Clouds	10
3.1	Base Quantities	10
3.2	Cloud Optical Quantities	11
3.3	Single Scattering Properties of Cloud Particles	13
3.4	Practical Treatment of Scattering Phase Function	16
3.4.1	Truncation of Forward Scattering Peak	17
3.4.2	Delta-M Method	18
3.4.3	Delta-Fit Method	19
3.5	Cloud Volume Scattering Properties	20
3.6	Radiative Transfer Equation	21
4	Measurements	23
4.1	SMART-Albedometer	23
4.1.1	Optical Inlet for Radiance Measurements	25
4.1.2	Radiometric Calibration of Radiance Measurements	30
4.1.3	Integration on POLAR 2	31
4.1.4	Configuration	32
4.1.5	Measurement Uncertainties	34
4.2	Supplementary Instrumentation	38
4.3	Overview of ASTAR 2007	41
4.3.1	<i>In Situ</i> Measurements	41
4.3.2	Airborne Lidar Measurements	45
4.3.3	Radiation Measurements	45
5	Radiative Transfer in Arctic Boundary-Layer Mixed-Phase Clouds	48
5.1	Radiative Transfer Model	48
5.1.1	Basic Model Input	48
5.1.2	Surface Albedo	49
5.1.3	Cloud Properties	50
5.2	Optical Properties of Individual Ice Crystals	51
5.3	Cloud Microphysical Properties	51
5.3.1	Liquid Water Mode	52

5.3.2	Ice Mode	54
5.4	Mixing of Ice and Liquid Water Mode	54
5.5	Cloud Radiative Forcing	58
5.5.1	Solar Radiative Forcing	58
5.5.2	IR and Total Radiative Forcing	61
5.6	Impact of Ice Crystals Shape on Cloud Optical Properties	62
5.7	Spectral Cloud Top Reflectance	64
6	Remote Sensing of Cloud Thermodynamic Phase	66
6.1	Spectral Slope Ice Index I_S	66
6.2	Principle Component Analysis (PCA) Ice Index I_P	68
6.3	Anisotropy Ice Index I_A	70
6.4	Sensitivity Studies	72
6.4.1	Cloud Optical Properties	73
6.4.2	Vertical Distribution	74
6.5	Case Study on Flight # 5	75
6.6	Case Study on Flight # 9	78
7	Vertical Structure of Arctic Boundary-Layer Mixed-Phase Clouds	82
7.1	Closure of Cloud Optical Thickness	82
7.2	Closure of Ice Optical Fraction	84
7.3	Vertical Footprint of Radiance Measurements	87
7.4	Ice Crystals at Cloud Top	91
7.5	Observation of Glory	93
8	Summary, Conclusions and Outlook	97
	List of Symbols	104
	List of Abbreviations	108
	List of Figures	111
	List of Tables	112
	Bibliography	113

1 Introduction of Arctic Boundary-Layer Mixed-Phase Clouds

1.1 Importance

In 2007–2008 the third International Polar Year (IPY) concentrate the efforts of the science community to improve our understanding of the Arctic and Antarctic climate, cryosphere, flora and fauna and their impact on the society in polar areas (Allison *et al.*, 2007). The relevance of the IPY was amplified by the current discussion on a dramatic climate change in Arctic regions related to the most prominent consequence the melting of the Arctic sea ice, which reaches in summer 2007 an all time minimum extend since the beginning of the records (*e.g.*, Smedsrud *et al.*, 2008; Giles *et al.*, 2008; Kay *et al.*, 2008).

A key point for a better understanding of the Arctic climate is to improve the quantification of the regional Arctic energy budget. The Earth's energy budget is defined by the difference of the incoming solar (wavelength range of 0.2–5 μm) and outgoing thermal infrared (IR; 5–100 μm) radiant flux densities (called irradiances). It is modified by several processes such as scattering, absorption and emission of radiation by atmospheric constituents and the Earth's surface. The energy budget of Arctic regions differs essentially from the globally and annually averaged schema as shown by Serreze *et al.* (2007).

In Figure 1.1 the energy budget of the Arctic ocean domain for January and July derived from reanalysis data is compared to the global mean energy budget of the Earth as presented by Trenberth *et al.* (2009). The major difference between the global and regional Arctic energy budget is the imbalance between net incoming solar and net outgoing IR irradiance. In July the net incoming irradiance is enhanced due to polar day and exceeds the net outgoing IR irradiance by 10 W m^{-2} . During polar night in January the net incoming solar irradiance is zero. Therefore, the net outgoing IR irradiance dominates the energy budget. In total, Arctic areas emit more energy by IR radiation than received by solar radiation. In contrast to the energy gain at lower latitudes Arctic areas act as major energy sink of the Earth's radiative budget. This imbalance is leveled by meridional heat transport from lower latitudes. Annually averaged 84 W m^{-2} are transported within the atmosphere and 6 W m^{-2} within the ocean. This meridional transport defines the characteristics of the global atmospheric circulation and related weather processes.

Furthermore, the Arctic energy budget shows a high seasonal variability. The energy gained in summer is temporarily stored in the Arctic ocean and atmosphere and leads to a melting of the Arctic sea ice. In July 105 W m^{-2} are stored in the ocean and 2 W m^{-2} in the atmosphere. This energy is released in winter which results in the formation of sea ice. For January 52 W m^{-2} are released from the Arctic ocean and 4 W m^{-2} from the atmosphere.

In Arctic regions clouds in general, and boundary-layer clouds in particular are of special importance in this regard and play a crucial role in the predicted Arctic climate warming

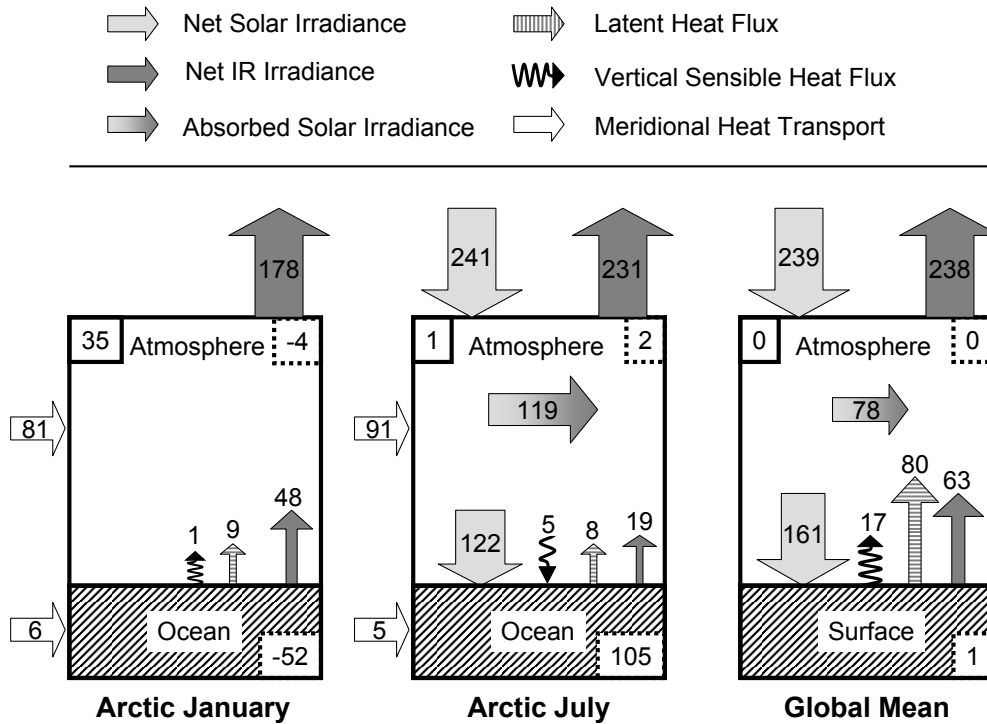


Figure 1.1: Energy budget of the Arctic ocean domain for January and July as derived from reanalysis data (Serreze *et al.*, 2007). The global mean energy budget of the Earth is shown on the right panel as presented by Trenberth *et al.* (2009). The different energy fluxes are illustrated by arrows. The arrow size is proportional to the magnitude of the energy flux (irradiance). Numbers give the values of the irradiance in units of W m^{-2} . The number in the upper and lower right corner of each panel give the net energy stored in the atmosphere and ocean. The degree of closure of the energy budget (or lack thereof) is indicated by the residual of the energy budget given in the upper left corners of each panel.

as reported in the Arctic Climate Impact Assessment (ACIA, Corell, 2004):

“... *Specific cloud types observed in the Arctic atmospheric boundary-layer present a serious challenge for atmospheric models. Parameterizing low-level Arctic clouds is particularly difficult because of the complex radiative and turbulent interactions with the surface ...*”

As shown by Shupe and Intrieri (2004) boundary-layer clouds are the most important contributors to the Arctic surface radiation budget. Generally Arctic boundary-layer clouds act (annually averaged) similar to warming greenhouse gases (Intrieri *et al.*, 2002). The warming by absorption of upwelling IR radiation and emission at lower temperatures exceeds the cooling due to reflection of solar radiation. In detail their radiative impact is highly variable and depends on surface albedo, aerosol particles, cloud water content, cloud particle size and cloud thermodynamic phase (Curry *et al.*, 1996; Shupe and Intrieri, 2004). Additionally, the long periods of permanent polar day and polar night strongly

modify the competition between IR and solar radiative effects. For instance, a low surface albedo in summer leads to a temporary cooling effect of Arctic clouds (Freese and Kottmeier, 1998; Dong and Mace, 2003; Kay *et al.*, 2008). Changing either of those cloud parameters will impact the radiative effects of the clouds.

Mixed-phase clouds are common in the Arctic due to the low temperatures. They consist of both supercooled liquid water particles and solid ice crystals simultaneously and were observed and investigated during numerous Arctic field experiments. For example, Turner *et al.* (2003) have analyzed ground-based remote sensing data during the Surface Heat Budget of the Arctic Ocean experiment (SHEBA) and identified 6–20% of the observed clouds as mixed-phase clouds. Even higher portions (26–46%) of mixed-phase clouds were observed during the First and Third Canadian Freezing Drizzle Experiments I/III (CFDE I/III; Cober *et al.*, 2001). 33% of the observed clouds were identified as mixed-phase clouds during the Arctic Cloud Experiment of the First International Satellite Cloud Climatology Project Regional Experiment (FIRE-ACE; McFarquhar and Cober, 2004). While SHEBA, CFDE I/III and FIRE-ACE analyzed clouds in winter and spring the Mixed-Phase Arctic Clouds Experiment (M-PACE) confirmed the existence of mixed-phase clouds in Arctic autumn (Verlinde *et al.*, 2007; Shupe *et al.*, 2008a).

As it is not trivial that mixed-phase clouds may exist, in the following Section 1.2 the physics which explain the coexistence of liquid water and ice particles in these clouds are briefly introduced. The detailed objectives addressed by this work are motivated in Section 2.

1.2 Formation Mechanism

Water droplets can exist in a metastable liquid phase (so-called supercooled liquid water droplets) at temperatures below zero down to about -40°C (Pruppacher and Klett, 1997). This wide temperature range allows that ice crystals and liquid water droplets may coexist. In fact Korolev *et al.* (2003) observed supercooled liquid water droplets in clouds down to temperatures of -35°C . However, the coexistence of ice and liquid water is unstable as described by the Wegener-Bergeron-Findeisen (WBF) mechanism (Wegener, 1911; Bergeron, 1935; Findeisen, 1938).

The basis of the WBF mechanism is that for a particular temperature the water vapor pressure over an plane ice surface is smaller than over a plane liquid water surface. This is described by the saturation vapor pressure illustrated in the phase diagram of water in Figure 1.2. Consequently, water vapor saturation with respect to ice is reached easier than over liquid water surfaces. Only for conditions that both ice and liquid water saturation is reached ice crystals and liquid water crystals can grow simultaneously (gray area in Figure 1.2). However, often conditions in between with ice saturation but subsaturation for liquid water are observed (light gray area in Figure 1.2). In this case, the water vapor prefers to evaporate from the liquid water droplets and to condensate on the ice crystals. The ice crystals grow on the expense of the liquid water droplets which shrink until there is no more liquid water available in the considered volume. Consequently, on a longer time

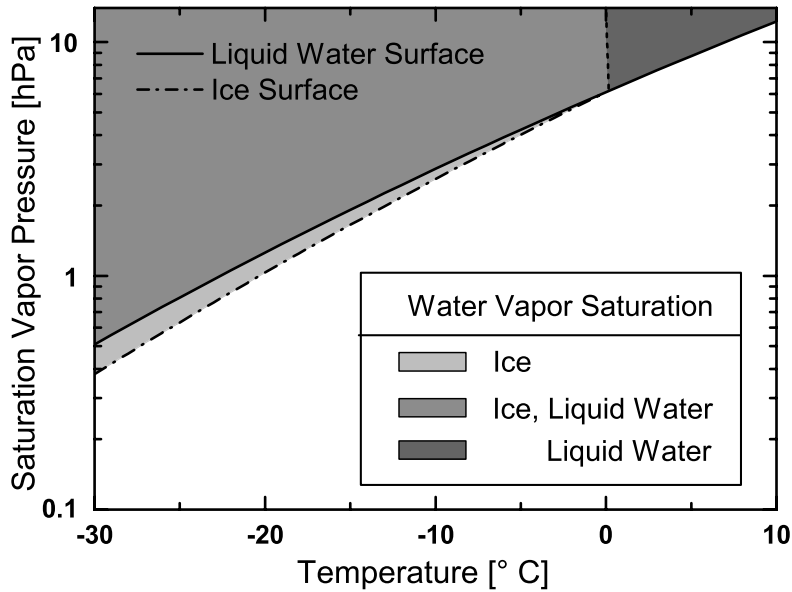


Figure 1.2: Saturation vapor pressure of water with respect to plane ice and liquid water surfaces. Conditions for saturation with respect to both ice and liquid water surfaces are marked gray. Conditions for saturation with respect to exclusively ice or liquid water surfaces are marked light gray and dark gray, respectively.

scale the coexistence of ice crystals and liquid water droplets is impossible. The time scale in which a mixed-phase cloud with ice crystal number concentrations of 10^2 – 10^3 l^{-1} and liquid water content below 0.5 $g\ m^{-3}$ undergoes a total glaciation is estimated by Korolev and Isaac (2003) with 20–40 min. From these considerations the existence of mixed-phase clouds in general is not obvious, as stated by Harrington *et al.* (1999):

“... *Since the mixed-phase system is colloidally unstable, one expects that the coexistence of liquid water and ice will cause the depletion of the liquid over a certain period of time ...*”

However, in fact boundary-layer mixed-phase clouds have been observed frequently over Arctic areas (*e.g.*, Cober *et al.*, 2001; Korolev *et al.*, 2003; Turner *et al.*, 2003; McFarquhar and Cober, 2004).

An explanation of why indeed in Arctic boundary-layer mixed-phase clouds (ABM) clouds ice crystals and liquid water droplets may coexist over longer time periods is given by Korolev and Mazin (2003); Korolev and Field (2008). Korolev and Mazin (2003) included the vertical wind velocity in the consideration of the WBF mechanism. Due to the temperature decrease caused by adiabatic lifting the probability that both ice and liquid water saturation is reached increases. Depending on the ice crystal number concentration, effective diameter, temperature and pressure a threshold velocity is defined. For vertical velocities exceeding this threshold liquid water droplets and ice crystals may grow simultaneously. In a subsequent study Korolev and Field (2008) add a second condition for the coexistence of ice and liquid water. A threshold vertical distance defines how high a

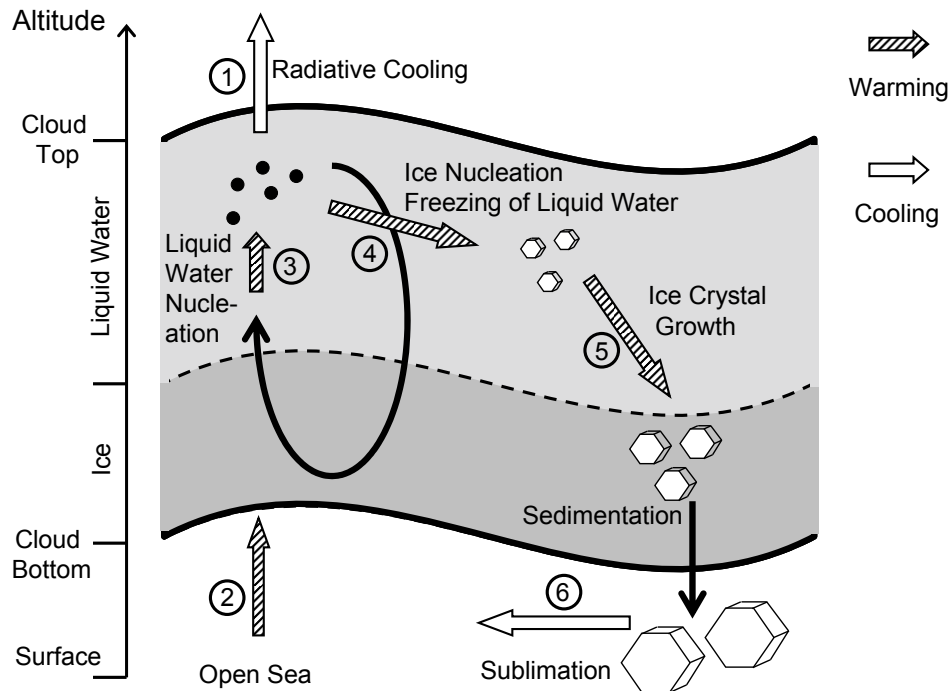


Figure 1.3: Illustration of the relevant processes present in ABM clouds. Processes that cause a cooling of the surrounding air are indicated by empty arrows; processes which lead to a warming are plotted with filled arrows.

cloud parcel has to be lifted until saturation with respect to liquid water is reached. However, ABM clouds can not fully be explained by the WBF mechanism and the updraft velocity. Radiation effects, the ice crystal shape, aggregation and sedimentation rates which have been neglected for simplification by Korolev and Field (2008) are crucial for the existence of mixed-phase clouds. A more complex overview on the self-maintaining processes in ABM clouds is given by Harrington *et al.* (1999). A scheme of their considerations is given in Figure 1.3.

In this scheme the coexistence of ice and liquid water relies on the balance between the condensation rate of liquid water droplets (LWC rate), the ice crystal growth rate (IWC rate), and the removal of ice nuclei (IN) by precipitating ice crystals. The unstable temperature layering above the open sea induces convection by which liquid water nucleation occurs in the updrafts (increase of LWC). As the concentration of cloud condensation nuclei (CCN) is typically lower than the concentration of IN (*e.g.*, Fridlind *et al.*, 2007; Morrison *et al.*, 2008), the liquid water nucleation exceeds the ice crystal nucleation in this part of the cloud (LWC rate $>$ IWC rate). However, once ice crystals have formed from IN or by freezing of liquid water droplets, they grow due to the WBF mechanism at the expense of the liquid water droplets. Finally, the ice crystals start to sediment which removes ice mass (IWC) and IN from the cloud system. The removal of IN due to the

precipitating ice crystals reduces the ice crystal number concentration and prevents for total glaciation of the ABM clouds.

This process leads to the typical vertical structure of ABM clouds with a liquid water layer at cloud top and an ice layer with precipitating ice crystals below (*e.g.*, Pinto, 1998; Shupe *et al.*, 2006; McFarquhar *et al.*, 2007).

The single processes included in the scheme of ABM clouds are related to cooling or warming of the cloud as indicated by open (cooling) and full arrows (warming) in Figure 1.3. The persistence of the updrafts responsible for the formation of liquid water droplets is ensured by radiative cooling at the cloud top (1, cooling) and the heat release of the open sea (2, warming). As Curry *et al.* (1988); Olsson *et al.* (1998) showed the cloud-scale circulations are primarily driven by radiative cooling which decreases the stability of the temperature layering and maintains the updrafts. In competition with the radiative cooling other processes stabilize the temperature layering. Latent heat release by liquid water droplet nucleation (3, warming), ice crystal nucleation (4, warming), freezing of liquid water droplets (4, warming) and ice crystal growth (5 warming) heats the cloud top, whereas sublimation of ice crystals (6, cooling) reduces the temperatures at cloud bottom.

This simplified scheme presented in Figure 1.3 is altered by a number of factors which have to be in equilibrium to assure the persistence of the ABM clouds. Only slight changes may result in a total glaciation of the ABM cloud as shown by Harrington *et al.* (1999). In this regard ice crystals and ice nuclei play a crucial part. However, the nucleation, growth and sedimentation of ice crystals are still not well understood which leads to discrepancies between observed and simulated ice crystal number concentrations (*e.g.*, Morrison *et al.*, 2008; Fan *et al.*, 2008). As a consequence the results of cloud resolving dynamical models are highly sensitive to the parameterizations of these processes as shown by *e.g.*, Harrington *et al.* (1999); Morrison *et al.* (2005); Prenni *et al.* (2007). Morrison *et al.* (2005) analyzed the importance of different ice production processes while Harrington *et al.* (1999) investigated the dependence of the life time of ABM clouds on temperature, ice crystal number concentration and ice crystal shape and found that the concentration of ice nuclei is the most determining parameter. An increase of the ice nuclei concentration results in a rapid glaciation of ABM clouds and reduces their life times.

2 Motivation and Objectives

2.1 Remote Sensing

As shown above the ice crystal properties are one essential parameter affecting the life time of ABM clouds. Therefore, information on the ice crystal properties is needed. *In situ* measurements of cloud microphysical properties such as ice crystal size, number concentration and shape have been conducted since many years. For example, parameterizations of the ice volume fraction (ratio of ice to total water content) as a function of cloud temperature have been obtained from *in situ* measurements by Boudala *et al.* (2004); Korolev *et al.* (2003). However, due to the limitations in time and space *in situ* measurements can only give a snapshot of the complexity of Arctic clouds (Lawson *et al.*, 2001; Cober *et al.*, 2001; McFarquhar *et al.*, 2007). To globally and continuously derive information on the ice crystal properties remote sensing technologies on board of satellites or long-range aircrafts have to be applied.

One essential information provided by several cloud retrieval algorithms for different satellite sensors is the cloud particle thermodynamic phase (liquid water or ice). Commonly, before retrieving cloud properties a preselection algorithm distinguishes between ice, mixed-phase and liquid water clouds (Key and Intrieri, 2000; King *et al.*, 2004; Kokhanovsky *et al.*, 2006). This phase discrimination is often based on two methods measuring the radiation emitted by the clouds at IR wavelengths (brightness temperatures) or measuring the radiation reflected by the clouds at wavelengths in the near infrared range (NIR, 700–3000 nm). Further methods are based on radar data (CloudSat, Sassen and Wang, 2008) and polarization measurements, for example using data of the POLarization and Directionality of the Earth’s Reflectances instrument (POLDER, Buriez *et al.*, 1997).

The contrast of brightness temperatures measured at two wavelengths is related to the ice volume fraction due to the spectral differences of the ability of ice and liquid water to emit radiation at wavelengths larger than 10 μm . Similarly, the radiation reflected at NIR wavelengths is affected by the different refractive indices (in particular the imaginary part, *i.e.* absorption index) of ice and liquid water as demonstrated by Pilewskie and Twomey (1987). Therefore, the ratio of reflected radiation measured at two NIR wavelengths can be used to determine the cloud thermodynamic phase (band ratio method). Both methods were compared by Chylek *et al.* (2006) for the Moderate Resolution Imaging Spectroradiometer (MODIS) showing significant discrepancies between the results of the two methods with a tendency of the band ratio method to overestimate the frequency of ice clouds. The authors suggest to improve the band ratio method by using the ratio of highly resolved NIR spectral bands around 1.5 and 1.4 μm .

Recently new remote sensing techniques have become available. Compared to satellite sensors using distinct wavelength bands new hyperspectral cameras cover almost the entire solar radiation with high spectral resolution. For the Scanning Imaging Absorption Spectrometer for Atmospheric CHartography (SCIAMACHY) on board of

ENVISAT (ENViironmental SATellite) Acarreta *et al.* (2004) successfully applied a cloud phase retrieval using the spectral reflectance between 1550 nm and 1670 nm. However, to improve the retrieval algorithms of these hyperspectral cameras new retrieval methods have to be developed and validated.

In this work new data analysis methods to retrieve information on the ice crystal properties are developed and applied to measurements collected with the Spectral Modular Airborne Radiation measurement sysTem (SMART-Albedometer). The SMART-Albedometer was improved to match the characteristics of spaceborne remote sensing techniques. The measurements analyzed and presented within this work were obtained during the Arctic Study of Tropospheric Aerosol, Clouds and Radiation (ASTAR) 2007 campaign. The campaign took place in the vicinity of Svalbard (78° N, 15° E) in March/April 2007 and focused on the sampling of ABM clouds. It included airborne remote sensing measurements by the SMART-Albedometer, as well as airborne lidar and *in situ* measurements of microphysical cloud parameters.

The improvement of the SMART-Albedometer and the measurements obtained during the ASTAR 2007 campaign are described in Section 4. The extensive data set of airborne measurements was used to develop, apply and validate new retrieval methods for the phase discrimination in ABM clouds. For the validation of the retrieved ice crystal properties the results of the *in situ* and the lidar measurements were used.

Three different methods are presented in Section 6 which utilize SMART-Albedometer measurements of cloud radiative properties to retrieve the cloud thermodynamic phase. A new approach to obtain information on the vertical distribution of ice crystals in ABM clouds using the same measurements is described in Section 7.

2.2 Radiative Budget

The first focus of this work is to retrieve information on ice crystal properties of ABM clouds (cloud thermodynamic phase, vertical distribution of ice crystals) from differences in the cloud optical properties obtained from airborne spectral radiation measurements.

For the second objective of this work the argumentation is reversed (ice crystal properties alter the cloud optical properties). From radiative transfer simulations the impact of ice crystal properties in particular the thermodynamic phase, ice crystal shape and dimension on the radiation budget of ABM clouds is quantified. As shown by Prenni *et al.* (2007) the glaciation of ABM clouds may cause errors in the surface radiative energy budget of up to 10–100 W m⁻². For a regional Arctic climate model Rinke and Dethloff (1997) found uncertainties in the incoming solar surface radiation ≤ 60 W m² dependent on parameterizations of ice volume fraction of ABM clouds. Additionally, investigations of Yoshida and Asano (2005) showed, that the radiation reflected by mixed-phase clouds decreases with increasing ice volume fraction in the NIR wavelength region. An increasing amount of large ice crystals, which absorb more radiation compared to water droplets reduces the reflected radiation.

Furthermore, Arctic mixed-phase clouds exhibit a variety of ice crystal shapes as observed by Lawson *et al.* (2001) and Fleishauer *et al.* (2002). Both studies showed crystal habits ranging from regular spheres, columns and plates to irregular aggregates. *In situ* observations reported by Korolev *et al.* (1999) have shown that regular ice crystals are rare in Arctic clouds ($\leq 9\%$). Due to aging processes (alternating growth and sublimation) and coagulation irregular crystals exhibit the majority of ice crystals.

For pure ice clouds several investigations have shown that the impact of crystal shape on radiative transfer actually is important (*e.g.*, Takano and Liou, 1989; Kinne and Liou, 1989; Chou *et al.*, 2002; Key *et al.*, 2002; Wendisch *et al.*, 2005). Wendisch *et al.* (2005) showed that for low solar zenith angles the solar radiative forcing of a cirrus cloud of moderate optical thickness could vary by 26% depending on ice crystal shape. Liou and Takano (1994) used a climate model assuming cirrus clouds with hexagonal plates instead of ice spheres. This resulted in a significant change of mean surface temperature of about 0.4 K. Similar systematic investigations for mixed-phase clouds are sparse.

To estimate the impact of ice crystal properties on the radiative forcing of ABM clouds extensive radiative transfer simulations have been performed within this work. The solar and IR cloud radiative forcing was analyzed as a function of the ice volume fraction, the ice crystal size and shape. The results of these investigations and the radiative transfer model used for the simulations are presented in Section 5. The general terminology of the quantities describing the radiative transfer and the cloud radiative properties are introduced in Section 3. Furthermore, within this section the radiative transfer theory is discussed with regard to the scattering processes of cloud particles. Methods are introduced which are applied in the numerical solution of the radiative transfer necessary to perform simulations including ice crystals.

3 Radiative Transfer in Clouds

3.1 Base Quantities

The power of electromagnetic radiation at a certain position and time is quantified by the radiant energy flux Φ in units of W. With regard to measurements and interpretation Φ is unpracticable. Therefore, two normalized radiant quantities (irradiance and radiance) are introduced (*e.g.*, Bohren and Clothiaux, 2006; Petty, 2006). The irradiance F also called radiant energy flux density is a measure of the radiant power transported through a unit surface dA with orientation \hat{n} in units of W m^{-2} ,

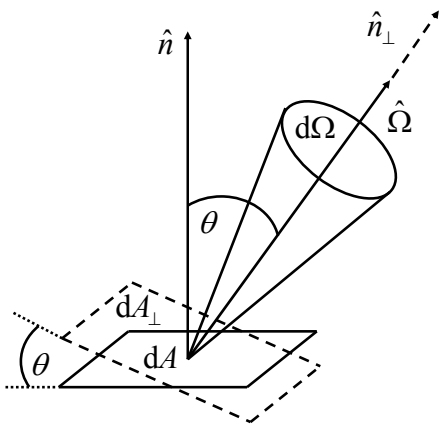


Figure 3.1: Geometry relevant for the definition of irradiance and radiance.

$$F = \frac{d\Phi}{dA} = \frac{d\Phi}{dA_{\perp}} \cos \theta. \quad (3.1)$$

The surface dA can be substituted by a surface $dA_{\perp} = dA \cdot \cos \theta$ perpendicular to the direction $\hat{\Omega}$ that describes the propagation of the radiant energy flux Φ as illustrated in Figure 3.1. The corresponding surface orientation \hat{n}_{\perp} is parallel to $\hat{\Omega}$. The zenith angle θ defines the difference between the orientations of dA_{\perp} (\hat{n}_{\perp}) and dA (\hat{n}).

The radiance $I(\hat{\Omega})$ (in units of $\text{W m}^{-2} \text{sr}^{-1}$) is defined as the radiant power transported within a solid angle $d\Omega$ in a given direction of propagation $\hat{\Omega}$ through an unit area dA_{\perp} or dA ,

$$I(\hat{\Omega}) = \frac{d^2\Phi}{dA_{\perp} d\Omega} = \frac{d^2\Phi}{\cos \theta dA d\Omega}. \quad (3.2)$$

The incremental solid angle $d\Omega$ is expressed by $\mu = \cos \theta$ the cosine of the zenith angle θ and the azimuth angle φ and defined as $d\Omega = d\mu d\varphi = \sin \theta d\theta d\varphi$. From Eqs. 3.1 and 3.2 it follows that F can be derived by integration of $I(\hat{\Omega})$ over $d\Omega$,

$$F = \int I(\hat{\Omega}) \cdot \cos \theta d\Omega \quad (3.3)$$

$$= \int_0^{2\pi} \int_0^{\pi} I(\theta, \varphi) \cdot \cos \theta \cdot \sin \theta d\theta d\varphi. \quad (3.4)$$

For atmospheric applications the surface dA is considered a horizontal plane. Thus F can be split into a downward irradiance F^{\downarrow} and an upward irradiance F^{\uparrow} . Therefore, the integration limits of Eq. 3.3 are substituted by the upper hemisphere ($\theta = 0 \dots \pi/2$, $\varphi = 0 \dots 2\pi$) and the lower hemisphere ($\theta = \pi/2 \dots \pi$, $\varphi = 0 \dots 2\pi$),

$$F^\downarrow = \int_0^{2\pi} \int_0^{\pi/2} I(\theta, \varphi) \cdot \cos \theta \cdot \sin \theta \, d\theta \, d\varphi. \quad (3.5a)$$

$$F^\uparrow = \int_0^{2\pi} \int_{\pi/2}^{\pi} I(\theta, \varphi) \cdot \cos \theta \cdot \sin \theta \, d\theta \, d\varphi. \quad (3.5b)$$

An analytic solution for Eq. 3.5a and 3.5b is derived for the case of an isotropic distribution of radiation. In this case the radiance is independent of the orientation $I(\hat{\Omega}) = I_0$ which results in:

$$F^\downarrow = F^\uparrow = \pi \text{ sr} \cdot I_0. \quad (3.6)$$

However, especially in the direction of the Sun which is included in F^\downarrow , $I(\hat{\Omega})$ is distributed anisotropic. Therefore, F^\downarrow is often divided into the direct solar radiation $F_{\text{dir}}^\downarrow$ and the diffuse sky radiation $F_{\text{diff}}^\downarrow$ with:

$$F^\downarrow = F_{\text{dir}}^\downarrow + F_{\text{diff}}^\downarrow. \quad (3.7)$$

All quantities described above can be converted into spectral quantities related to an infinitesimal wavelength range $d\lambda$ by using the spectral radiant energy flux $\frac{d\Phi}{d\lambda}$ in units of W m^{-1} . The units of the spectral irradiance F_λ and radiance $I_\lambda(\hat{\Omega})$ become $\text{W m}^{-2} \text{ nm}^{-1}$ and $\text{W m}^{-2} \text{ sr}^{-1} \text{ nm}^{-1}$ respectively.

3.2 Cloud Optical Quantities

Clouds strongly interact with solar and IR radiation by scattering, absorption and emission processes. To quantify the cloud optical properties several quantities are introduced. An universal quantity is the bidirectional reflectance distribution function $BRDF$ (Nicodemus *et al.*, 1977; Schaepman-Strub *et al.*, 2006) as illustrated in Figure 3.2a. by the incoming (yellow) and reflected (green) radiation. The $BRDF$ describes how the incident irradiance F_i from one direction (θ_i, φ_i) is reflected by a surface or layer (*e.g.* cloud) into the direction (θ_r, φ_r) . The reflected radiation is defined by the radiance $I_r(\theta_r, \varphi_r)$. The $BRDF$ in units of sr^{-1} is defined by,

$$BRDF(\theta_i, \varphi_i; \theta_r, \varphi_r) = \frac{dI_r(\theta_r, \varphi_r)}{dF_i(\theta_i, \varphi_i)}. \quad (3.8)$$

When reflectance properties are measured the common methods follow the definition of reflectance factors. The dimensionless bidirectional reflectance factor BRF is the ratio of the radiance I_r actually reflected by a sample surface to the radiance $I_{r,L}$ reflected by an ideal (non-absorbing) and diffuse (Lambertian) standard surface for identical irradiation and beam-geometry. With Eq. 3.8 this equals to the ratio between the $BRDF$ of the

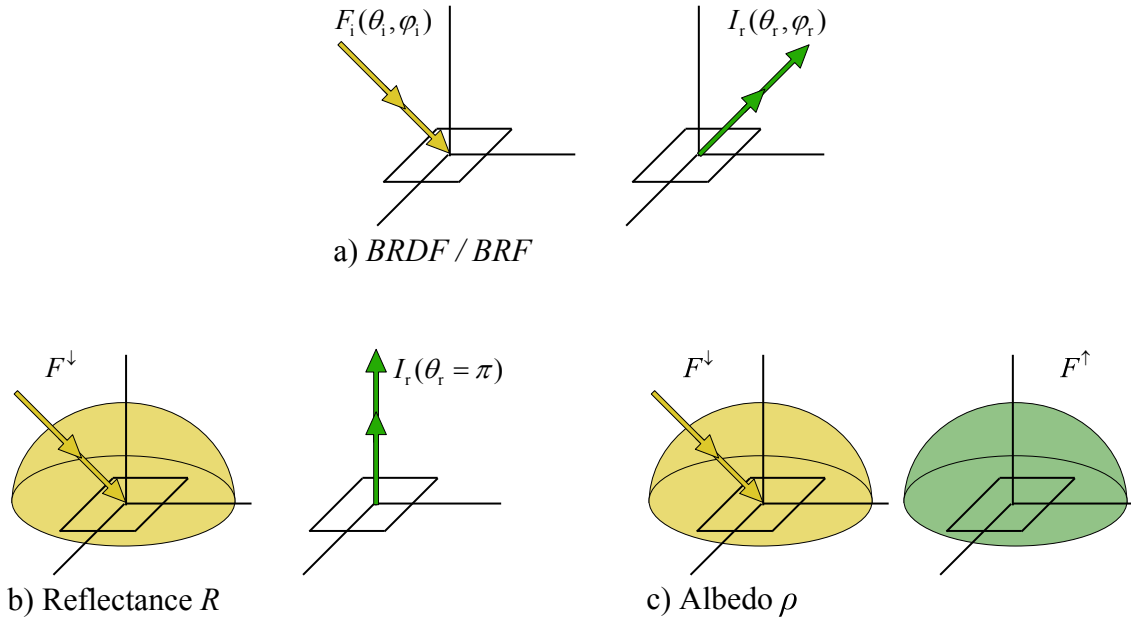


Figure 3.2: Illustration of the incoming (yellow) and reflected radiation (green) used to define the reflectance quantities a) $BRDF$ and BRF , b) cloud top reflectance R and c) albedo ρ .

sample surface and the $BRDF_L$ for Lambertian reflection,

$$BRF(\theta_i, \varphi_i; \theta_r, \varphi_r) = \frac{dI_r(\theta_r, \varphi_r)}{dI_{r,L}(\theta_r, \varphi_r)} = \frac{BRDF(\theta_i, \varphi_i; \theta_r, \varphi_r)}{BRDF_L(\theta_i, \varphi_i; \theta_r, \varphi_r)}. \quad (3.9)$$

An ideal Lambertian surface reflects the radiation isotropically (*cf.* Eq. 3.6) and it holds $BRDF_L = (\pi \text{ sr})^{-1}$. For the general case this leads to the bidirectional reflectance factor

$$BRF(\theta_i, \varphi_i; \theta_r, \varphi_r) = \pi \text{ sr} \cdot BRDF(\theta_i, \varphi_i; \theta_r, \varphi_r). \quad (3.10)$$

The $BRDF$ and BRF are defined for infinitesimal elements of solid angle and therefore can be measured approximately only. By integration of Eq. 3.8 over φ and θ further relevant quantities can be derived. For our purposes the hemispherical-directional reflectance into nadir direction $\theta_r = \pi$ (in case of clouds this is called cloud top reflectance R) and the bihemispherical reflectance, generally called albedo ρ as illustrated in Figure 3.2b and 3.2c are used. For R (dimensionless) the radiance reflected in nadir direction $I_r^\uparrow = I(\theta_r = \pi)$ is related with the downwelling irradiance F^\downarrow . Considering Eq. 3.7, R composes of the BRF for the direct solar beam and the BRF for the diffuse sky radiation both scattered into nadir direction. With $f_{\text{dir}} = F_{\text{dir}}^\downarrow / F^\downarrow$ (the fractional amount of direct downwelling irradiance) it follows:

$$R = BRF\left(\theta_i, \varphi_i; \theta_r = \frac{\pi}{2}\right) \cdot f_{\text{dir}} + BRF\left(2\pi; \theta_r = \frac{\pi}{2}\right) \cdot (1 - f_{\text{dir}}) = \frac{\pi \text{ sr} \cdot I_r^\uparrow(\theta_r = \pi)}{F^\downarrow}. \quad (3.11)$$

In this equation an indication of the azimuth angle φ_r can be omitted as the radiance in

nadir direction is used. In a similar manner the albedo (dimensionless) is defined as ratio of F^\uparrow and F^\downarrow ,

$$\rho = BRF(\theta_i, \varphi_i; 2\pi) \cdot f_{\text{dir}} + BRF(2\pi; 2\pi) \cdot (1 - f_{\text{dir}}) = \frac{F^\uparrow}{F^\downarrow}. \quad (3.12)$$

To guarantee conservation of energy ρ exhibits values between 0 and 1, while R can reach values larger than 1. For a Lambertian reflector it holds $R = \rho$.

From an energy budget point of view cloud optical properties are defined as layer properties correspondent to a layer between cloud top z_{top} and cloud base z_{base} . The advantage of these definitions is that the impact of clouds on the radiative transfer is separated from other processes like scattering of radiation by atmospheric gases and the Earth's surface. The cloud layer reflectance \mathcal{R} , transmittance \mathcal{T} and absorptance \mathcal{A} (all dimensionless) are defined by,

$$\mathcal{R} = \frac{F^\uparrow(z_{\text{top}}) - F^\uparrow(z_{\text{base}})}{F^\downarrow(z_{\text{top}})}, \quad (3.13)$$

$$\mathcal{T} = \frac{F^\downarrow(z_{\text{base}})}{F^\downarrow(z_{\text{top}})}, \quad (3.14)$$

$$\mathcal{A} = \frac{[F^\downarrow(z_{\text{top}}) - F^\uparrow(z_{\text{top}})] - [F^\downarrow(z_{\text{base}}) - F^\uparrow(z_{\text{base}})]}{F^\downarrow(z_{\text{top}})}. \quad (3.15)$$

These definitions hold for any layers: aerosol particles, clouds, whole atmosphere. For the conservation of energy it is:

$$1 = \mathcal{R} + \mathcal{T} + \mathcal{A}. \quad (3.16)$$

3.3 Single Scattering Properties of Cloud Particles

All scattering and absorption processes within the atmosphere are completely described by three quantities the extinction cross section C_{ext} , the single scattering albedo $\tilde{\omega}$ and the scattering phase function \mathcal{P} also called single scattering properties. With regard to the interaction of radiation and cloud particles the single scattering properties of the cloud particles are defined by the mass/cross-section area, spectral refractive index, particle shape and orientation of the cloud particle. For spherical particles like liquid water droplets an analytic solution exists from Mie-theory (Mie, 1908; Bohren and Huffman, 1998). For more complex and irregular shapes of ice crystals rather sophisticated models have to be used. The spectral single-scattering properties of individual nonspherical ice crystals are discussed in several publications, where different computational methods have been used (*e.g.*, Takano and Liou, 1989, 1995; Yang and Liou, 1996b; Macke and Francis, 1998; Grenfell and Warren, 1999; Klotzsche and Macke, 2006).

The data of the ice crystals presented in this work were supplied by Yang and Liou (1996a) and Yang *et al.* (2005). For the single scattering properties of liquid water droplets Mie-theory was applied (Bohren and Huffman, 1998).

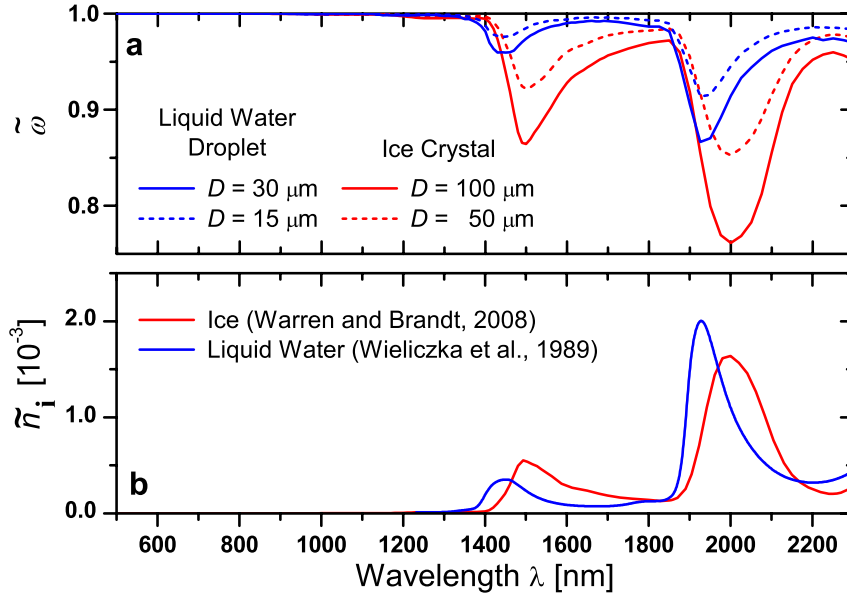


Figure 3.3: Spectral single scattering albedo $\tilde{\omega}$ for liquid water droplets and column shaped ice crystals of different maximum dimension D (panel a). The imaginary part of the spectral refractive index \tilde{n}_i of liquid water and ice is shown in panel b.

The extinction cross section C_{ext} in units of m^2 characterizes the attenuation of radiation by a single cloud particle. It is defined by the sum of the scattering cross section C_{sca} and the absorption cross section C_{abs} (both in units of m^2):

$$C_{\text{ext}} = C_{\text{sca}} + C_{\text{abs}}. \quad (3.17)$$

The probability of how much incident radiation is scattered or absorbed by a cloud particle is characterized by the dimensionless single scattering albedo $\tilde{\omega}$. It is defined by the ratio of the scattering and extinction cross section,

$$\tilde{\omega} = \frac{C_{\text{sca}}}{C_{\text{ext}}} = \frac{1 - C_{\text{abs}}}{C_{\text{ext}}} \quad (3.18)$$

For the fraction of scattered radiation the scattering phase function \mathcal{P} characterizes the angular probability distribution of scattering processes from an incident direction $[\mu_i, \varphi_i]$ into any direction $[\mu, \varphi]$. It is normalized by the following definition,

$$\int_0^{2\pi} \int_{-1}^1 \mathcal{P}([\mu_i, \varphi_i] \longrightarrow [\mu, \varphi]) d\mu d\varphi = 4\pi \text{ sr}. \quad (3.19)$$

For an azimuthal symmetric or azimuthally averaged scattering phase function $\mathcal{P}(\cos \vartheta)$ the scattering direction is described by the scattering angle ϑ , which is related to μ and μ_i by,

$$\cos \vartheta = \mu\mu_i + \sqrt{1 - \mu^2} \cdot \sqrt{1 - \mu_i^2}. \quad (3.20)$$

In Figure 3.3a exemplarily the spectral single scattering albedo for liquid water droplets and column shaped ice crystals of different maximum dimension D are shown. The plot reveals that the particle dimension (cross section) is one determining factor for $\tilde{\omega}$. The larger the particles the higher the absorption and the smaller $\tilde{\omega}$. The spectral characteristics of $\tilde{\omega}$ are caused by the spectral pattern of the imaginary part of the refractive index \tilde{n}_i shown in Figure 3.3b. As the refractive indices of liquid water and ice are shifted, the minima in $\tilde{\omega}$ differ for liquid water droplets and ice crystals.

Differences in \mathcal{P} of liquid and ice crystal cloud particles result mainly from the particle shape and dimension. Examples of azimuthally averaged scattering phase functions at 500 nm wavelength are shown in Figure 3.4 for liquid water droplets and column shaped ice crystals of two different maximum dimensions. The nonspherical ice particles show a strong and narrow forward scattering peak as indicated by the close up for scattering angles $\vartheta = 0-5^\circ$ in panel a. The intensity of these forward peaks, which have their origin in the Fraunhofer diffraction, increases strongly with increasing particle diameter. That is why \mathcal{P} of the small water droplets is less dominated by the forward peak than \mathcal{P} of the larger ice crystals. Additionally, in case of regular ice crystals with plan parallel sides radiation is transmitted through the ice crystals without a change in its direction ($\vartheta = 0^\circ$). This partition of scattered radiation is called Delta-transmission (Takano and Liou, 1989).

Other features of typical ice crystal scattering phase function are halo structures ($\vartheta = 22^\circ/46^\circ$), the enhanced sideward scattering ($\vartheta = 60-130^\circ$) and the intensive backscat-

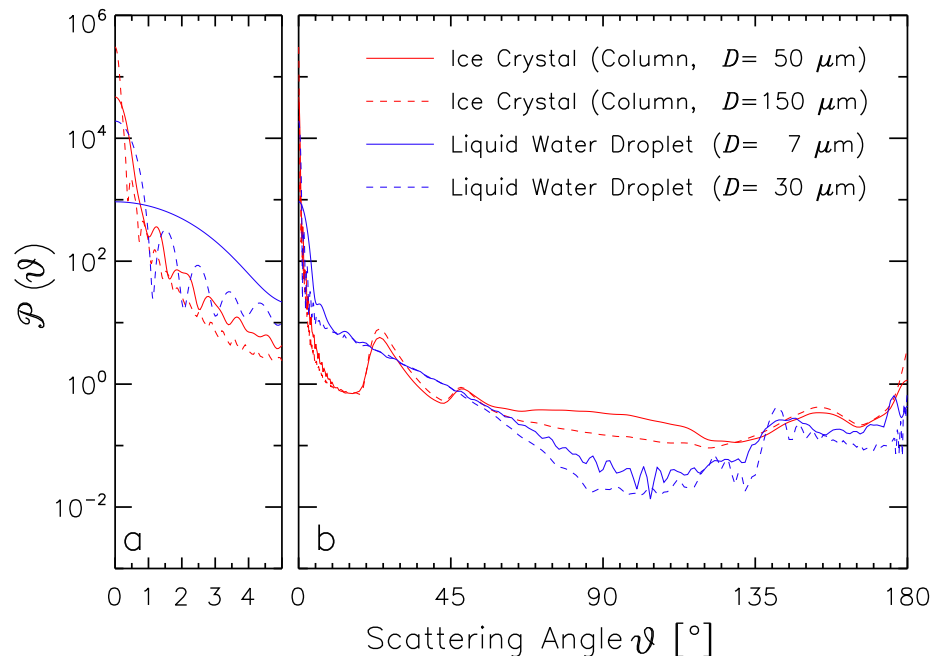


Figure 3.4: Scattering phase function of individual liquid water droplets (blue lines) and column shaped ice crystals (red lines) at 500 nm wavelength (panel b). Panel a shows a close up for scattering angles $\vartheta = 0-5^\circ$.

tering section ($\vartheta = 180^\circ$). The irregular pattern in the scattering phase function of the liquid water droplets results from resonances in the solution of Mie-theory which are not resolved by the angular resolution presented in Figure 3.4. However, a typical feature of small liquid water droplets is the backscatter glory. It is characterized by the local maximum of the scattering phase function ($D = 7 \mu\text{m}$) at 175° .

3.4 Practical Treatment of Scattering Phase Function

The numerical solution of the radiative transfer equation requires the expansion of the scattering phase function $\mathcal{P}(\cos \vartheta)$ into a series of Legendre polynomials,

$$\mathcal{P}(\cos \vartheta) = \sum_{n=0}^{\infty} b_n \cdot P_n(\cos \vartheta). \quad (3.21)$$

The dimensionless Legendre polynomials $P_n(\cos \vartheta)$ are defined by,

$$P_n(\cos \vartheta) = \frac{1}{2^n n!} \frac{d^n}{d \cos^n \vartheta} (\cos^2 \vartheta - 1)^n. \quad (3.22)$$

The dimensionless moments b_n of the Legendre expansion represent the contribution of each Legendre polynomial to the Legendre expansion and are derived from,

$$b_n = \frac{2n+1}{2} \int_{-1}^{+1} \mathcal{P}(\cos \vartheta) \cdot P_n(\cos \vartheta) d \cos \vartheta. \quad (3.23)$$

An example for calculated b_n of a scattering phase function of column shaped ice crystals ($D = 150 \mu\text{m}$, $\lambda = 500 \text{ nm}$) is shown in Figure 3.5a. The original scattering phase function is given in Figure 3.5b as thick dashed line. The calculated b_n decrease asymptotically with the order n from unity to values close to zero for $n \rightarrow \infty$ (not shown here). For large ice crystals with a strong and narrow forward scattering peak like the example shown in Figure 3.5 the decrease of b_n is weak. This reveals that a vast number of high order polynomials are required to accurately represent the scattering phase functions of large ice crystals (Wiscombe, 1977).

Theoretically, the series of Legendre polynomials is infinite. In practice, the number of polynomials is limited by the computing time required for calculating the Legendre moments which escalates roughly with a factor proportional to n^3 (Hansen, 1971). Therefore, the numerical expansion has to be terminated (truncated) at a certain degree of the series Λ ;

$$\mathcal{P}^*(\cos \vartheta) = \sum_{n=0}^{\Lambda-1} b_n \cdot P_n(\cos \vartheta). \quad (3.24)$$

By this truncation information on small scale fluctuations in the scattering phase function is skipped. Especially for large ice crystals with a strong and narrow forward scattering peak this results in an inaccurate representation of the scattering phase function in radiative transfer. In Figure 3.5b–d the scattering phase function \mathcal{P}^* recalculated from

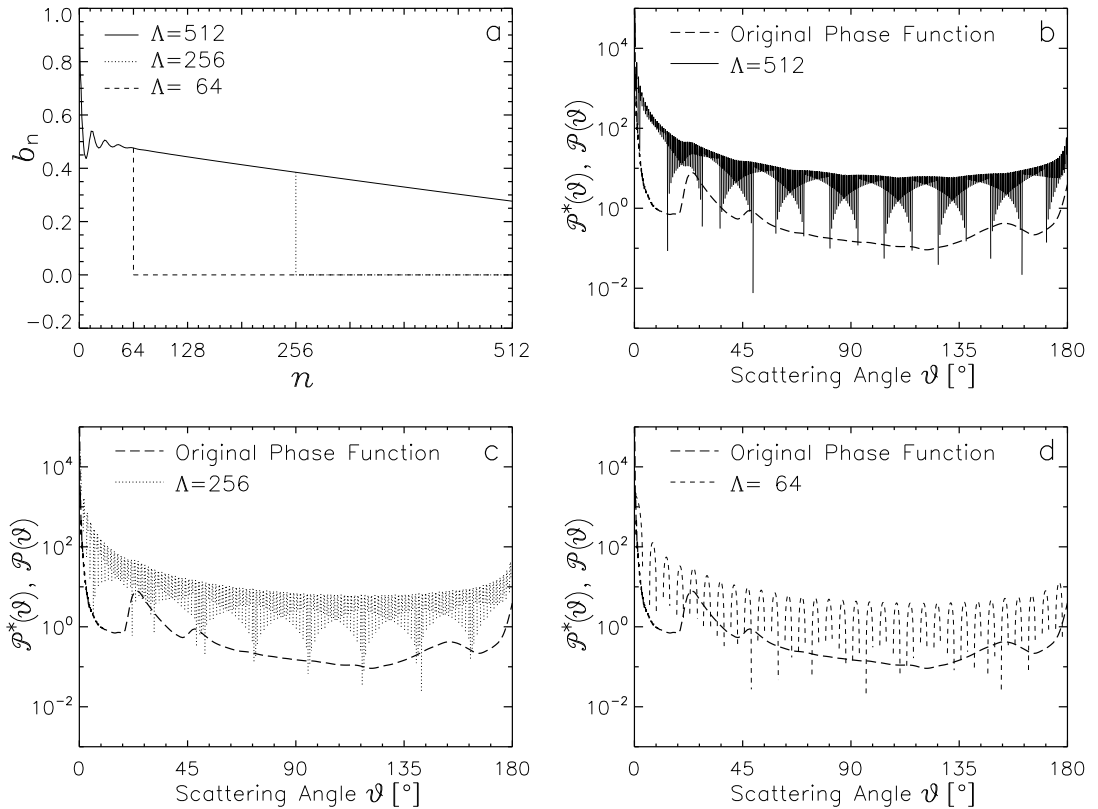


Figure 3.5: Legendre expansion of an exemplary scattering phase function (column shaped ice crystal, $D = 150 \mu\text{m}$, $\lambda = 500 \text{nm}$). The Legendre moments b_n are given in panel a. The original scattering phase function \mathcal{P} and the scattering phase functions \mathcal{P}^* recalculated from the Legendre moments are shown in panels b–d.

the Legendre moments given in Figure 3.5a are shown. Three different solutions are obtained for truncating the Legendre series at $\Lambda = 512/256/64$. The plot reveals that due to the truncation of the Legendre series the scattering phase functions are poorly reproduced. Not only the forward scattering peak is much broader, also fluctuations across all scattering angles are introduced.

To overcome these problems different methods have been developed as described below.

3.4.1 Truncation of Forward Scattering Peak

The primary method introduced to reduce the required number of Legendre moments Λ is the truncation of the forward scattering peak (Wiscombe, 1977). This method first proposed by Potter (1970) uses the fact, that the main energy scattered within the forward scattering peak is located in scattering angles close to $\vartheta = 0^\circ$. It is suggested that due to the negligible small scattering angles this fraction of radiation can be practically reallocated into the direct unscattered solar radiation. Therefore, the forward scattering in the original phase function \mathcal{P} is truncated resulting in the truncated scattering phase

function \mathcal{P}_{tr} by,

$$\mathcal{P}_{\text{tr}} = \mathcal{P} - h, \quad (3.25)$$

with h representing the truncated part of \mathcal{P} . This truncation reduces the fraction of scattered radiation and increases the fraction of direct radiation. To maintain energy conservation the scattering properties (single scattering albedo, extinction cross section) have to be scaled too.

If the fraction of energy f_{tr} within the truncated forward peak is represented by the integral over the truncation function h ,

$$f_{\text{tr}} = \frac{1}{2} \int_{-1}^{+1} h(\cos \vartheta) \, d \cos \vartheta = \frac{1}{2} \int_{-1}^{+1} [\mathcal{P}(\cos \vartheta) - \mathcal{P}_{\text{tr}}(\cos \vartheta)] \, d \cos \vartheta, \quad (3.26)$$

the scattering in the radiative transfer equation has to be reduced by scaling the scattering cross section with,

$$C'_{\text{sca}} = (1 - f_{\text{tr}}) \cdot C_{\text{sca}}. \quad (3.27)$$

With unchanged absorption cross section $C'_{\text{abs}} = C_{\text{abs}}$ the extinction cross section C_{ext} and the single scattering albedo $\tilde{\omega}$ are scaled accordingly by,

$$C'_{\text{ext}} = (1 - f_{\text{tr}} \tilde{\omega}) \cdot C_{\text{ext}}, \quad (3.28)$$

and,

$$\tilde{\omega}' = \frac{1 - f_{\text{tr}}}{1 - f_{\text{tr}} \tilde{\omega}} \cdot \tilde{\omega}. \quad (3.29)$$

For reasons of the normalization given in Eq. 3.19 \mathcal{P}_{tr} also has to be scaled with f_{tr} ,

$$\mathcal{P}'_{\text{tr}} = \frac{\mathcal{P}_{\text{tr}}}{1 - f_{\text{tr}}}. \quad (3.30)$$

The Legendre moments of the truncated scattering phase function can be calculated from the original moments by,

$$b'_n = \frac{b_n - c_n}{1 - f_{\text{tr}}}, \quad (3.31)$$

with c_n representing the Legendre moments of the truncation function h .

3.4.2 Delta-M Method

There had been a number of approaches to find an appropriate function h to truncate the forward scattering peak as discussed in Wiscombe (1977). The Delta-Eddington approximation proposed by Joseph *et al.* (1976) suggests to use the Dirac-Delta-function δ_{D} to represent h by,

$$h = 4f_{\text{tr}} \cdot \delta_{\text{D}}(\cos \vartheta - 1). \quad (3.32)$$

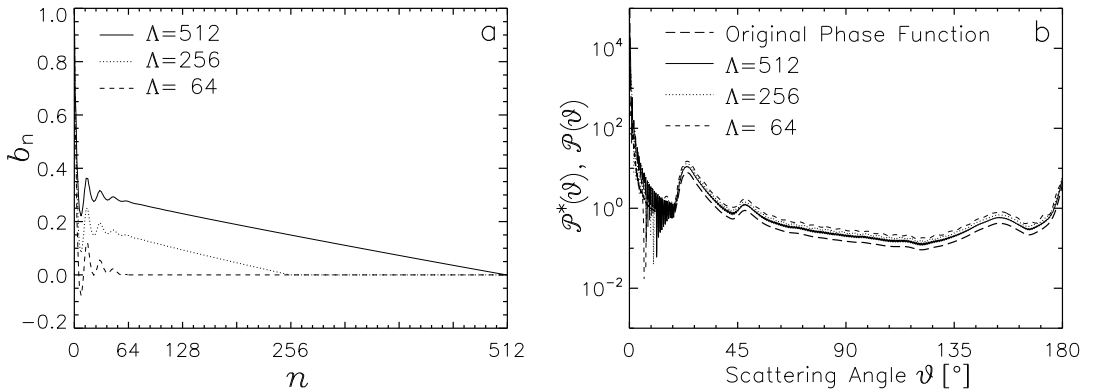


Figure 3.6: Delta-M scaled moments of the Legendre expansion shown in Figure 3.5. The scaled Legendre moments b_n are given in panel a. The original scattering phase function \mathcal{P} and the scattering phase functions \mathcal{P}^* recalculated from the scaled Legendre moments are shown in panel b.

Calculating the Legendre moments c_n by using Eq. 3.23 it is found that $c_n = f_{\text{tr}}$ and therefore,

$$b'_n = \frac{b_n - f_{\text{tr}}}{1 - f_{\text{tr}}}. \quad (3.33)$$

The open question is how to find an appropriate value of f_{tr} and at which Λ to truncate the Legendre series. Giving a solution for both issues the Delta-M method proposed by Wiscombe (1977) suggest to set the energy f_{tr} of the truncated Delta-function equal to the unscaled Legendre moment of the order Λ , $f_{\text{tr}} = b_\Lambda$. With this assumption a fast decrease of the scaled Legendre moments is derived, with $b'_\Lambda = 0$. All moments of higher order were truncated respectively set to zero.

The Delta-M scaled Legendre moments of the original Legendre expansion given in Figure 3.5a are shown in Figure 3.6a. The scattering phase functions \mathcal{P}^* recalculated from the scaled moments are displayed in Figure 3.6b. Compared to the recalculated unscaled \mathcal{P}^* (Figure 3.5b) a serious improvement of the representation of the original phase function is obvious. Only for the forward scattering angles up to $\vartheta = 20^\circ$ a fluctuating structure remains. The differences in the absolute level of the recalculated \mathcal{P}^* compared to the original \mathcal{P} results from the scaling (*cf.* Eq. 3.33).

3.4.3 Delta-Fit Method

The Legendre expansion in general (Eq. 3.21) comprises an infinite series. Thus information is inevitably skipped when truncating the expansion at order Λ . The Delta-fit method proposed by Hu *et al.* (2000) applies a least-squares fit of the scattering phase function to a limited number of Legendre polynomials Λ . The weights of the fit are then used as Legendre moments and applied to the Delta-M approximation.

The scaled and unscaled Legendre moments ($\Lambda = 256/128/64$) for the exemplary scattering phase function given in Figure 3.5b calculated with the Delta-fit are plotted in

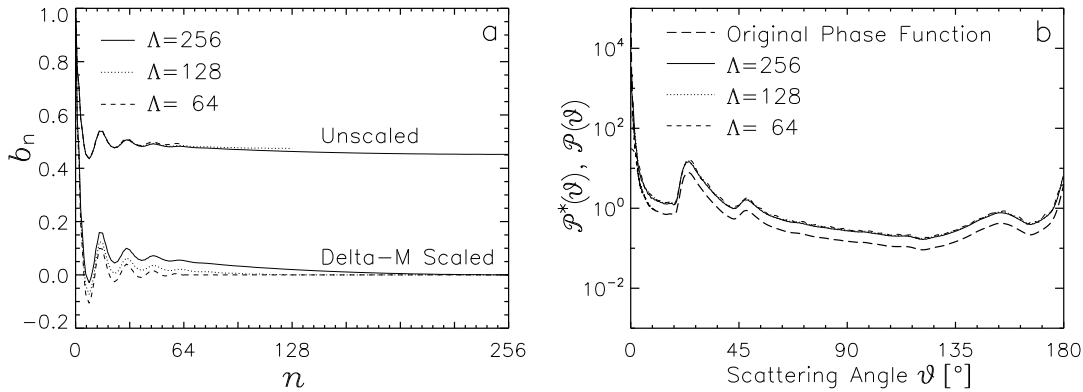


Figure 3.7: Unscaled and Delta-M scaled moments of the Legendre expansion derived from the Delta-fit method for the scattering phase function shown in Figure 3.5. The unscaled and scaled Legendre moments b_n are given in panel a. The original scattering phase function \mathcal{P} and the scattering phase functions \mathcal{P}^* recalculated from the scaled Legendre moments are shown in panel b.

Figure 3.7a. For $\Lambda = 64$ and $\Lambda = 128$ the unscaled moments show slightly higher values at high orders n than the moments obtained for $\Lambda = 256$. This enhancement of high order Legendre moments by the Delta-fit method results in an even better representation of \mathcal{P} at forward scattering angles lower than 20° compared to the results from the Delta-M method (*cf.* Figure 3.6). Already 64 Legendre moments are sufficient to obtain an accurate representation of the scattering phase function as shown in Figure 3.7b.

3.5 Cloud Volume Scattering Properties

The optical properties of a cloud volume b_{ext} , $\langle \tilde{\omega} \rangle$, $\langle \mathcal{P}(\cos \vartheta) \rangle$ are calculated by integration of the single scattering properties $C_{\text{ext}}(D)$, $\tilde{\omega}(D)$, $\mathcal{P}(\cos \vartheta, D)$ weighted by the number size distribution of the scattering cloud particles $\frac{dN}{dD}(D)$ related to the cloud volume (*e.g.*, Wendisch *et al.*, 2005). The spectral volumetric extinction coefficient b_{ext} in units of m^{-1} is calculated by,

$$b_{\text{ext}} = \int C_{\text{ext}}(\tilde{D}) \cdot \frac{dN}{dD}(\tilde{D}) d\tilde{D}. \quad (3.34)$$

Due to the linear relation $C_{\text{ext}}(D) = C_{\text{sca}}(D) + C_{\text{abs}}(D)$ between extinction, absorption and scattering cross section Eq. 3.34 can be used similar for the volumetric absorption b_{abs} and volumetric scattering coefficient b_{sca} (both in units of m^{-1}). With the definition of the single scattering albedo (Eq. 3.18) the volumetric single scattering albedo (dimensionless) results from,

$$\langle \tilde{\omega} \rangle = \frac{1}{b_{\text{ext}}} \int \tilde{\omega}(\tilde{D}) \cdot C_{\text{ext}}(\tilde{D}) \cdot \frac{dN}{dD}(\tilde{D}) d\tilde{D}. \quad (3.35)$$

In a similar manner the volumetric phase function $\langle \mathcal{P}(\cos \vartheta) \rangle$ (dimensionless) is calcu-

lated by,

$$\langle \mathcal{P}(\cos \vartheta) \rangle = \frac{1}{b_{\text{sca}}} \int \mathcal{P}(\cos \vartheta, \tilde{D}) \cdot C_{\text{sca}}(\tilde{D}) \cdot \frac{dN}{dD}(\tilde{D}) d\tilde{D}. \quad (3.36)$$

As discussed above the numerical solution of the radiative transfer equation requires to provide the Legendre moments b_n of $\langle \mathcal{P}(\cos \vartheta) \rangle$. This leads to intensive calculations due to the variation of cloud properties and the vast number of wavelengths considered in spectral radiative transfer simulations. A faster approach is to compute first the Legendre moments $b_n(D)$ of the individual ice crystal scattering phase functions $\mathcal{P}(\cos \vartheta, D)$ according to Eq. 3.23 and apply appropriate mixing formulas for the volumetric Legendre moments $\langle b_n \rangle$ afterwards. With the Legendre expansions Eq 3.21 and Eq. 3.36 it holds,

$$\langle \mathcal{P}(\cos \vartheta) \rangle = \frac{1}{b_{\text{sca}}} \int \sum_{n=0}^{\infty} \left[b_n(\tilde{D}) P_n(\cos \vartheta) \right] \cdot C_{\text{sca}}(\tilde{D}) \cdot \frac{dN}{dD}(\tilde{D}) d\tilde{D}. \quad (3.37)$$

As $C_{\text{sca}}(\tilde{D})$ and $\frac{dN}{dD}(\tilde{D}) d\tilde{D}$ are independent to the index n of the Legendre expansion and $P_n(\cos \vartheta)$ is independent to the particle dimension \tilde{D} Eq. 3.37 can be rearranged to,

$$\langle \mathcal{P}(\cos \vartheta) \rangle = \sum_{n=0}^{\infty} P_n(\cos \vartheta) \left[\frac{1}{b_{\text{sca}}} \int b_n(\tilde{D}) \cdot C_{\text{sca}}(\tilde{D}) \cdot \frac{dN}{dD}(\tilde{D}) d\tilde{D} \right]. \quad (3.38)$$

This gives an expression for the volumetric scattering phase function similar to the Legendre expansion of individual scattering phase function (*cf.* Eq. 3.21),

$$\langle \mathcal{P}(\cos \vartheta) \rangle = \sum_{n=0}^{\infty} \langle b_n \rangle \cdot P_n(\cos \vartheta), \quad (3.39)$$

with the volumetric Legendre moments $\langle b_n \rangle$ defined by,

$$\langle b_n \rangle = \frac{1}{b_{\text{sca}}} \int b_n(\tilde{D}) \cdot C_{\text{sca}}(\tilde{D}) \cdot \frac{dN}{dD}(\tilde{D}) d\tilde{D}. \quad (3.40)$$

3.6 Radiative Transfer Equation

The attenuation of direct solar radiation I_{dir} within an optical medium is described by the Beer-Lambert-Bouguer law (also called Beer's law),

$$\mu_0 \frac{dI_{\text{dir}}(\tau, \mu_0, \varphi_0)}{d\tau} = -I_{\text{dir}}, \quad (3.41)$$

with $\mu_0 = \cos \theta_0$ the cosine of the solar zenith angle θ_0 and the solar azimuth angle φ_0 defining the position of the Sun. As vertical coordinate the optical thickness $\tau(z)$ (dimensionless) is used. In general, $\tau(z)$ is defined by the integral of the volumetric extinction coefficient of an optical medium b_{ext} over the geometric height z ,

$$\tau(z) = \int_0^z b_{\text{ext}}(\tilde{z}) d\tilde{z}. \quad (3.42)$$

For the optical thickness of clouds z_{top} and z_{base} are used as integration limits:

$$\tau(z) = \int_{z_{\text{base}}}^{z_{\text{top}}} b_{\text{ext}}(\tilde{z}) d\tilde{z}. \quad (3.43)$$

Eq. 3.41 is solved by using S_0 the incident extraterrestrial irradiance at the top of the atmosphere (solar constant):

$$I_{\text{dir}}(\tau, \mu_0, \varphi_0) = S_0 \cdot \exp\left[-\frac{\tau}{\mu_0}\right]. \quad (3.44)$$

From this equation follows that the direct solar radiation reaching the Earth's surface is negligible in the case of ABM clouds. For high solar zenith angles ($\theta_0 > 70^\circ$) as presentative for the Arctic and optical thick clouds ($\tau > 2$) less than 0.5% of the direct solar radiation is transmitted through the cloud.

Therefore, in the following the radiative transfer equation (RTE) is discussed in a simplified form relevant for the solar radiative transfer in ABM clouds. Exclusively diffuse radiation characterized by the diffuse radiance I_{diff} is considered and thermal emission of radiation is neglected. With these assumptions the 1-dimensional (1D) RTE for a plane-parallel, horizontally homogeneous atmosphere can be written as:

$$\mu \frac{dI_{\text{diff}}(\tau, \mu, \varphi)}{d\tau} = I_{\text{diff}} - (J_{\text{dir}} + J_{\text{diff}}). \quad (3.45)$$

The direction of propagation of I_{diff} (viewing direction) is defined by $\mu = \cos \theta$ the cosine of the zenith angle θ and the azimuth angle φ . The radiation scattered into the viewing direction is described by the two source terms J_{dir} and J_{diff} in parenthesis of the right side of Eq. 3.45. J_{dir} , also called single scattering term, specifies how much radiation is scattered from the direct solar radiation into the viewing direction:

$$J_{\text{dir}} = \frac{\tilde{\omega}(\tau)}{4\pi \text{ sr}} \cdot S_0 \cdot \exp\left[-\frac{\tau}{\mu_0}\right] \cdot \mathcal{P}(\tau, [-\mu_0, \varphi_0] \longrightarrow [\mu, \varphi]) \quad (3.46)$$

The incident extraterrestrial irradiance at the top of the atmosphere S_0 is attenuated exponentially according to Beer's law passing along the optical thickness τ . The attenuated fraction of S_0 is scattered with a probability defined by the single scattering albedo $\tilde{\omega}$ and the scattering phase function \mathcal{P} .

The second source term J_{diff} in Eq. 3.45 is called the multiple scattering term and describes scattering processes by which diffuse radiation is scattered into the viewing direction:

$$J_{\text{diff}} = \frac{\tilde{\omega}(\tau)}{4\pi \text{ sr}} \int_0^{2\pi} \int_{-1}^1 I_{\text{diff}}(\tau, \mu_i, \varphi_i) \cdot \mathcal{P}(\tau, [\mu_i, \varphi_i] \longrightarrow [\mu, \varphi]) d\mu_i d\varphi_i \quad (3.47)$$

Similar to J_{dir} , the single scattering albedo $\tilde{\omega}$ and the scattering phase function \mathcal{P} characterize all scattering processes included in J_{diff} .

4 Measurements

The measurements presented within this work were conducted during the Arctic Study of Tropospheric Aerosol, Clouds and Radiation (ASTAR) 2007 campaign in the vicinity of Svalbard (78° N, 15° E) in March/April 2007. The 2007 campaign was the third of a series of experiments organized by the Alfred Wegener Institute for Polar and Marine Research (AWI) and the German Aerospace Center (DLR) including aircraft and ground based measurements in Arctic regions. The original aim of ASTAR was to investigate the interaction of aerosol and solar radiation with the background of Arctic haze events commonly appearing in Arctic spring time (Yamanouchi *et al.*, 2005). With the second and third campaign the investigations were expanded with regard to aerosol-cloud interactions (Stachlewska, 2006; Gayet *et al.*, 2007).

Two aircraft, the DLR Falcon equipped to characterize aerosol properties by *in situ* measurements and the AWI POLAR 2 configured to sample clouds by remote sensing and *in situ* instruments, were employed during ASTAR 2007. Within this work data from the POLAR 2 aircraft is reported. The airborne instrumentation included the Spectral Modular Airborne Radiation measurement system (SMART-Albedometer), *in situ* instruments such as the Polar Nephelometer, Cloud Particle Imager (CPI), and Particle Measuring System (PMS) Forward Scattering Spectrometer Probe (FSSP-100), and the Airborne Mobile Aerosol Lidar (AMALi).

A detailed description of the instrumentation with focus on the SMART-Albedometer is given in the following Section 4.1. The supplement instrumentation on board of POLAR 2 is described in Section 4.2. An overview of the cloud microphysical and radiative properties obtained with these instruments during ASTAR 2007 is given in Section 4.3.

4.1 SMART-Albedometer

The SMART-Albedometer has been developed at the Leibniz-Institute for Tropospheric Research (IfT) as a modular system to measure solar spectral radiation (irradiance, actinic radiation) from airborne platforms (*e.g.*, Wendisch *et al.*, 2001; Wendisch and Mayer, 2003; Wendisch *et al.*, 2004; Jäkel *et al.*, 2005; Bierwirth, 2008; Bierwirth *et al.*, 2009). The basic setup and the single components are illustrated in Figure 4.1. Four optical inlets (two upward facing, two downward facing) collect downwelling and upwelling radiation separately. The radiation is guided by optical fibers (two of them bifurcated) to six spectrometer systems developed by Zeiss. These use a grating to spectrally disperse the incoming radiation which is detected afterwards by a single-line Photo-diode array (PDA). The electric signal obtained by the PDA is recorded by personal computers (PC 1–3) and has to be related to radiometric quantities by a radiometric calibration.

Two different spectrometer systems with different gratings and PDAs are employed in the SMART-Albedometer. The *VIS* is a Multi Channel Spectrometer (MCS UV/NIR) and covers the wavelength range 200–1050 nm by a 1024 pixel PDA. This range includes the visible wavelength (VIS) between 380 nm and 700 nm. The spectral resolution (full width

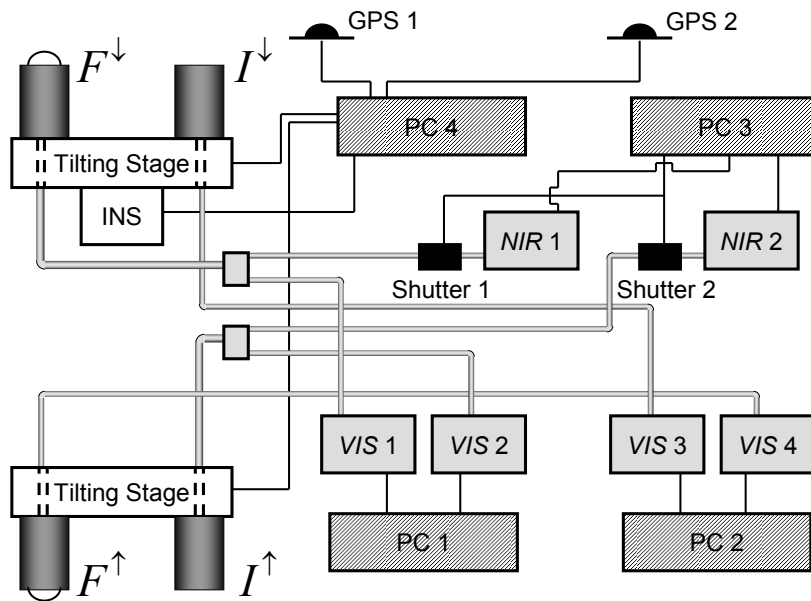


Figure 4.1: Basic setup and single components of the SMART-Albedometer (see text for details).

at half maximum, $FWHM$) of the VIS amounts to 2–3 nm. The second spectrometer system (NIR) applies a plane gratings (PGS, Plane Grating Spectrometer) and a 512 pixel PDA. It covers a portion of the NIR wavelength range 950–2100 nm with a $FWHM$ of 9–16 nm. The extraction of the radiation signal from the NIR data requires a realtime measurement of the dark signal (sum of dark current and thermally induced current) of the PDA (Bierwirth, 2008). Therefore, an optical shutter is plugged between the optical fiber and the NIR allowing for alternating measurements of radiation and dark signal.

A key feature of the SMART-Albedometer is the active stabilization of the optical inlets which compensates deviations of the aircraft attitude from the horizontal plane (developed in cooperation with *enviscope GmbH*). This is necessary because horizontal misalignments $\Delta\theta$ result in significant uncertainties of F_{λ}^{\downarrow} and F_{λ}^{\uparrow} Wendisch *et al.* (2001). For solar zenith angles larger than 70° a misalignment of $\Delta\theta = 1^{\circ}$ causes an error of 5% for the measurements of F_{λ}^{\downarrow} . The horizontal stabilization of the SMART-Albedometer is realized by two separate tilting stages on which the optical inlets are mounted. The tilting stages are adjusted by servo motors which are controlled by computer software (PC 4). They allow to correct for horizontal misalignments of up to $\pm 6^{\circ}$ with an accuracy of better than $\pm 0.2^{\circ}$. The system works properly for angular velocities up to 3° s^{-1} with a response time of the horizontal adjustment of 43 ms.

The actual attitude of the aircraft (roll and pitch angle) is obtained from an inertial navigation system (INS) designed by *iMAR GmbH*. It is supported by information of the global positioning system (GPS) supplied by a two antenna GPS receiver. The roll and pitch angle is measured with an accuracy of $< 0.1^{\circ}$ and a frequency of up to 200 Hz. These angles are utilized in real time by software (PC 4) to adjust the tilting stages.

4.1.1 Optical Inlet for Radiance Measurements

During ASTAR 2007 the SMART-Albedometer was employed to investigate the radiative cloud forcing and for the remote sensing of cloud properties. For remote sensing purposes radiance measurements of I_{λ}^{\uparrow} and I_{λ}^{\downarrow} were utilized. Therefore, a set of new optical inlets were constructed and characterized in this work. A photograph of the radiance optical inlet decomposed into its components is shown in Figure 4.2. A detailed technical drawing is given in Figure 4.3. The entrance optics of the radiance optical inlet is based on a Zeiss collimator lens (BK 7 glass) with a focal length of 31.6 mm. The design of the collimator mounting was developed by laboratory tests and ray tracing simulations. The setup was optimized by simulations to reduce the impact of stray light. In laboratory tests the opening angle of the optical inlet was determined.

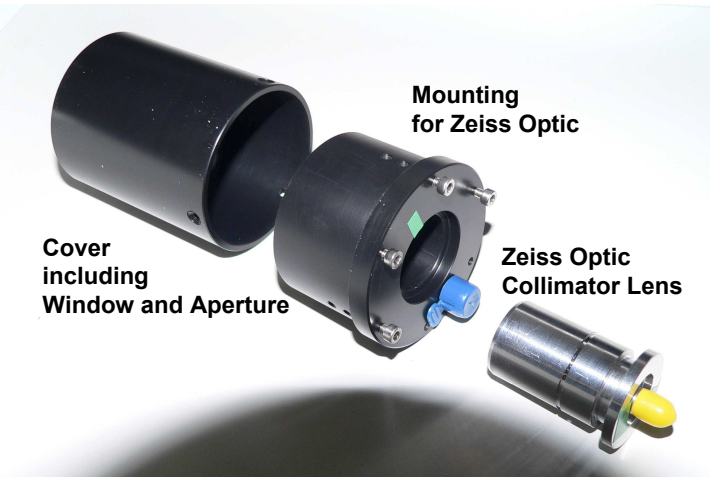


Figure 4.2: Photograph of the radiance optical inlet decomposed into its components.

Reduction of Stray Light

To simulate the stray light resulting from reflections at the side panels of the optical inlet the optical system design software ZEMAX[®] was used. The collimator lens and the cylindrical housing were implemented into the 3-dimensional (3D) non-sequential mode of ZEMAX[®]. It allows to freely define objects, radiation sources and detectors with which ray tracing can be simulated. Figure 4.4 shows a 3D view and a 2-dimensional (2D) cross section of the 3D model of the optical inlet. For the ray tracing simulations a horizontal radiation source was placed in front of the inlet emitting photons in random directions. A detector placed at the exit of the collimator lens counts the photons scattered into the optical fibre which is connected to the collimator lens. Photons reaching the detector on direct path are omitted per default from the radiation source.

The simulations have shown that an additional aperture placed directly in front of the collimator lens reduces stray light most efficiently. A snap shot of the ray tracing simulations is shown in Figure 4.4. The blue lines illustrate the rays traces at this single simulation. With the design shown here only a small fraction of the simulated photon paths is scattered into the collimator and the optical fiber.

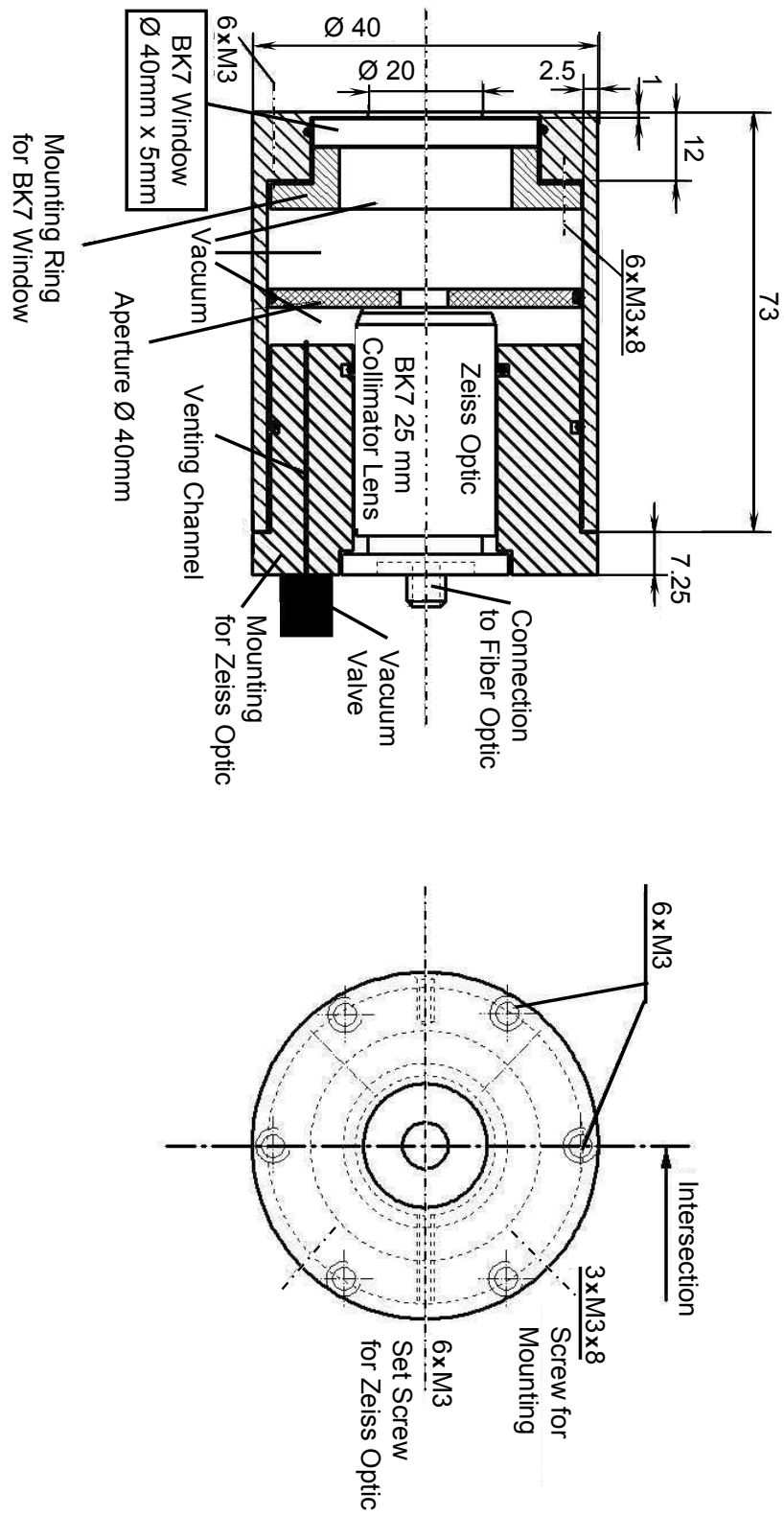


Figure 4.3: Drawing of the radiance optical inlet (provided by Berthold Friederich).

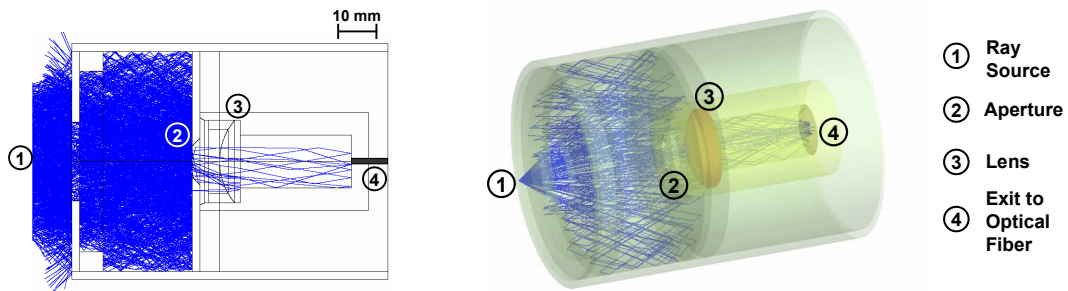


Figure 4.4: 2D cross section and 3D view of the ray tracing simulations for the radiance optical inlet performed with ZEMAX[®] to reduce stray light scattered from the housing into the optical fiber.

Opening Angle

The radiance is defined for an infinitesimal solid angle. Practically, the measurements have to collect radiation from a cone with defined opening angle. The corresponding geometry is illustrated in Figure 4.5. The opening angle Δ of the cone defines the boundaries for which radiation of incident angle δ reaches the exit of the optical inlet. For the collimator lens Δ is determined by the lens itself and the optical fiber connected to the collimator. Optical fibers with a large diameter D_F result in a large Δ and vice versa. For optical fibers with a diameter between $D_F = 0.6\text{--}1.3\text{ mm}$ opening angles in the range $\Delta = 0.8^\circ\text{--}2.1^\circ$ were measured. In the following detailed results for an optical inlet connected to an optical fiber of $D_F = 1.0\text{ mm}$ and with an opening angle of $\Delta = 1.5^\circ$ are presented.

In laboratory tests Δ of the inlet was characterized. Therefore, a narrow beam of radiation was generated with a 200 W lamp and two apertures focussing the radiation to a beam diameter $\sim 1\text{ mm}$. The collimator lens was mounted on a turn table and turned until the measured signal reaches zero.

The registered minimum and maximum angles $\delta_{\min}(\lambda, r)$ and $\delta_{\max}(\lambda, r)$ were recorded for different wavelengths λ and incident positions r of the beam with respect to the center of the lens (*cf.* Figure 4.5). It was found that both δ_{\min} and δ_{\max} increase with increasing wavelength and decrease with increasing r as shown in Figure 4.6. The measured dependence results from the lens geometry and the chromatic aberration of the lens.

From the measured $\delta_{\min}(\lambda, r)$ and $\delta_{\max}(\lambda, r)$ for each incident angle δ an appropriate min-

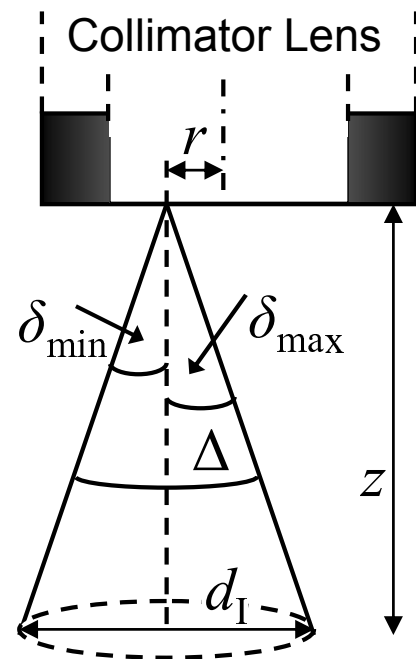


Figure 4.5: Definition of the opening angle Δ and the footprint d_I of the radiance measurements.

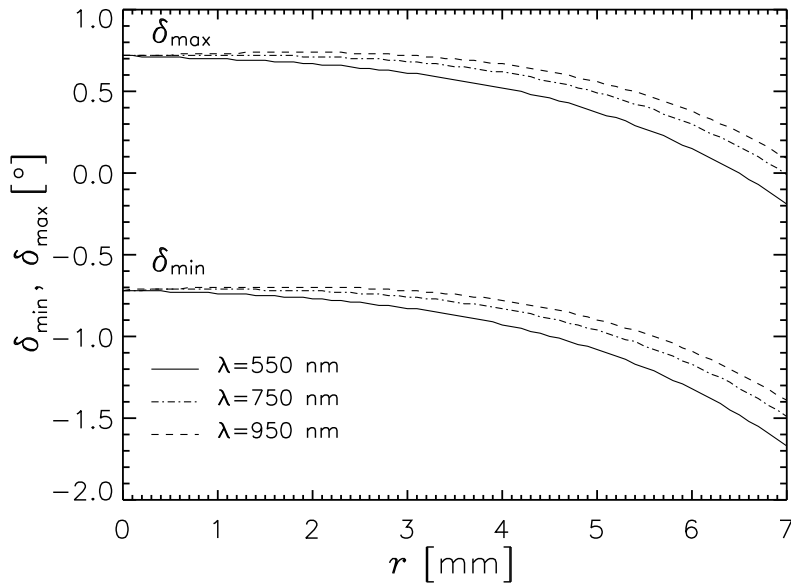


Figure 4.6: Minimum and maximum opening angle $\delta_{\min}(\lambda, r)$ and $\delta_{\max}(\lambda, r)$ of collimator lens at different positions with respect to the lens center r and wavelengths λ .

imum and maximum position $r_{\min}(\lambda, \delta)$ and $r_{\max}(\lambda, \delta)$ have been derived representing the part of the lens which collects radiation of this incident angle. With these characteristics the angular efficiency $E(\lambda, \delta)$ was calculated characterizing (for each δ) which fraction of the lens area transmits photons of this δ into the optical fiber,

$$E(\lambda, \delta) = \frac{1}{A_{\text{lens}}} \int_{r_{\min}(\lambda, \delta)}^{r_{\max}(\lambda, \delta)} 2\pi \cdot r \, dr. \quad (4.1)$$

$E(\lambda, \delta) = 1$ means that the entire lens area collects photons of this particular λ and δ . In Figure 4.7a $E(\lambda, \delta)$ is shown for the original collimator lens $d = 1.3$ cm and a wavelength of $\lambda = 550$ nm. Additional $E(\lambda, \delta)$ was calculated for configurations with additional apertures with diameter $d = 1.0$ cm and $d = 0.8$ cm in front of the collimator lens shadowing the edges of the lens. The plot shows that for all cases $E(\lambda, \delta)$ is reduced to 0.5 at incident angles of $\delta = -0.75^\circ$ and $\delta = 0.75^\circ$. This range is used to define the opening angle of the optical inlet $\Delta = 1.5^\circ$. Furthermore, it is obvious that if the entire lens area is exposed ($d = 1.3$ cm) the gradient of $E(\lambda, \delta)$ at angles of about $\delta = \pm 0.75^\circ$ is weakened.

A more sharp gradient is derived if apertures are placed in front of the lens. In principle this is equal to the apertures used in photography. An aperture reduces the intensity of collected radiation but improved the angular dependence of the optical inlet. The optimal solution between intensity gain and angular dependence was found for an aperture of $d = 0.8$ cm. For this aperture the wavelength dependence of $E(\lambda, \delta)$ is shown in Figure 4.7b. No significant wavelength dependence of Δ was found in this case. The slight differences in the gradient of $E(\lambda, \delta)$ are not crucial for the radiance measurements.

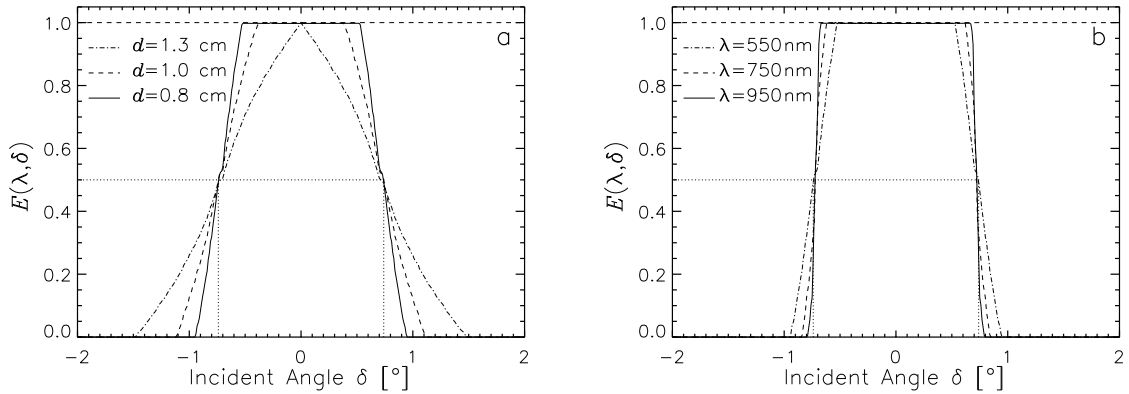


Figure 4.7: Angular efficiency $E(\lambda, \delta)$ of the radiance optical inlet for a) different aperture configuration at $\lambda = 550$ nm and b) different wavelengths for the configuration with an aperture of $d = 0.8$ cm.

With basic trigonometry the diameter of the footprint d_I representative for the radiance measurements at different distances z between surface and the optical inlet is calculated by,

$$d_I = 2z \cdot \arctan \frac{\Delta}{2}. \quad (4.2)$$

In Figure 7.6 the footprint corresponding to the ASTAR 2007 setup with an opening angle of $\Delta = 2.1^\circ$ is shown. For airborne measurements the footprint varies between 1 m at 30 m altitude and 110 m at 3,000 m altitude.

In an improved version of the optical inlets the outer aperture is covered by a BK 7 glass window providing vacuum conditions inside the tube. Thereby, the collimator lens is protected against condensation during changes of the external temperature conditions.

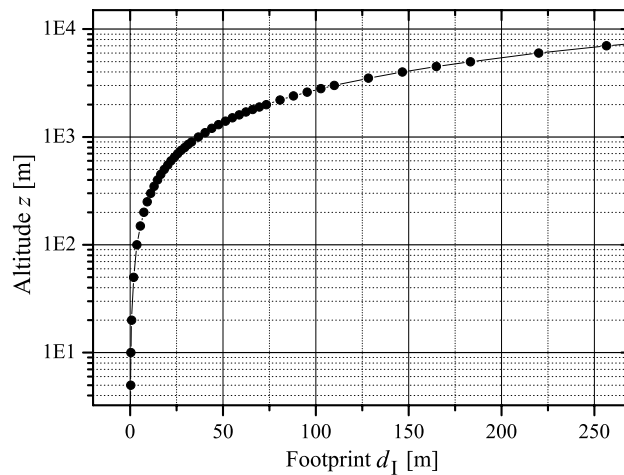


Figure 4.8: Altitude dependence of the footprint diameter d_I for the radiance optical inlet with opening angle $\Delta = 2.1^\circ$.

4.1.2 Radiometric Calibration of Radiance Measurements

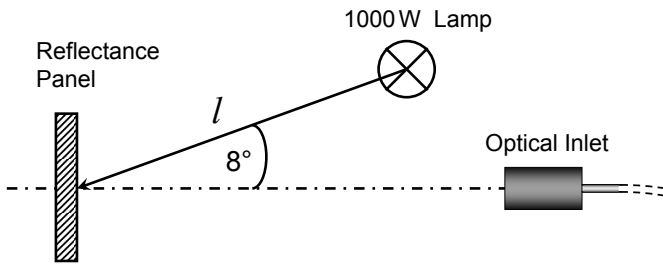


Figure 4.9: Radiometric calibration of radiance measurements using a reflectance panel.

To transfer the measured digital signals of the SMART-Albedometer into quantitative values of the spectral radiance a calibration against certified radiation sources is required. For this purpose, the imaging radiance optic requires the use of a source of diffuse radiation. Two approaches for calibrating the radiance measurements were compared. The first approach uses an irradiance standard (1000 W) emitting a defined irradiance $F_{\lambda,S}$ which is reflected by a certified reflectance panel. In Figure 4.9 the calibration setup is illustrated. The panel is made of Spectralon[®] material which reflects radiation highly Lambertian and produces an adequate diffuse radiation source. The panel is certified by an independent calibration traceable to National Institute of Standards and Technology (NIST) standards which provides the panel reflectance $R_P(\lambda)$. The reflectance is defined for an incident angle to the panel surface normal of 8° . The calibration factor $C_{\lambda,P}$ for the radiance measurements is calculated from the measured digital signal $S(\lambda)$ taking into account the distance l between irradiance standard and panel which deviates for practical reasons from the distance $l_0 = 50$ cm for which the irradiance standard is certified,

$$C_{\lambda,P} = \frac{F_{\lambda,S}}{\pi_{SR} \cdot R_P(\lambda)} \cdot \frac{l^2}{l_0^2} \cdot \frac{1}{S(\lambda)}. \quad (4.3)$$

The second approach uses a certified integrating sphere as illustrated in Figure 4.10. Within an integrating sphere the radiation of a source lamp is reflected by a Lambertian barium sulphate coating in a way that isotropic diffuse radiation reaches the exit aperture.

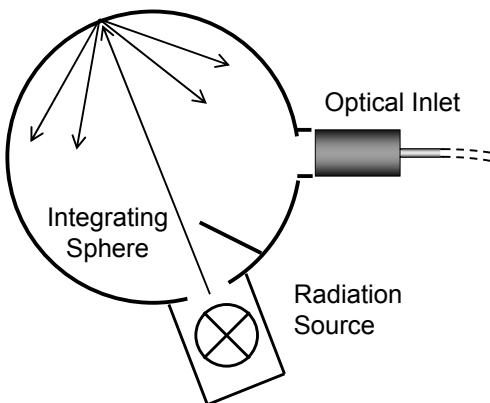


Figure 4.10: Radiometric calibration using an integrating sphere.

The spectral radiance $I_{\lambda,S}$ emitted through the exit aperture is certified by external calibration traceable to standards of the German Calibration Service (DKD). The calibration factor $C_{\lambda,S}$ for the radiance measurements is calculated from,

$$C_{\lambda,S} = \frac{I_{\lambda,S}}{S(\lambda)}. \quad (4.4)$$

The calibration factors $C_{\lambda,P}$ and $C_{\lambda,S}$ obtained for ASTAR 2007 are shown in Figure 4.11a. Both calibration factors have a strong spectral dependence which results a) from the spectrometer characteristics, b) the spectral output of the

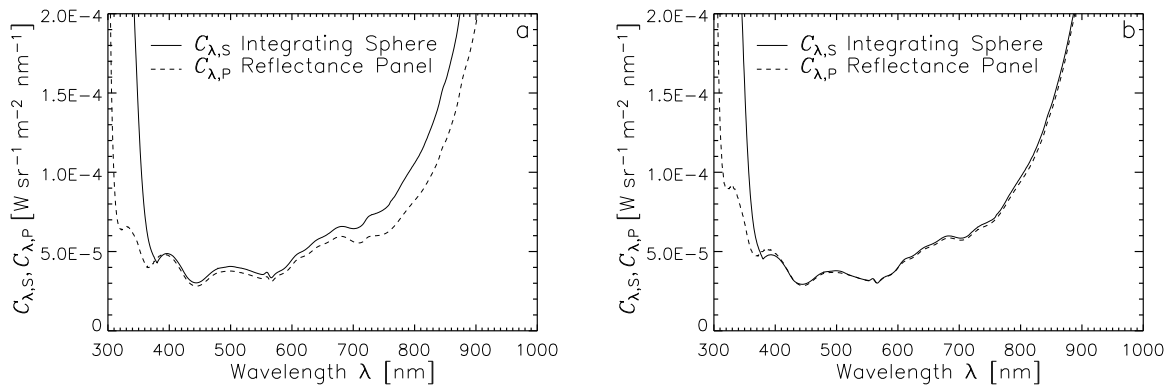


Figure 4.11: Absolute calibration factors for radiance measurements of a) ASTAR and b) MELTEX obtained from calibration against a reflection panel $C_{\lambda,P}$ and an integrating sphere $C_{\lambda,S}$.

radiation source and c) from absorption of radiation within the optical fiber and the BK 7 glass of the collimator lens and the covering window. BK 7 glass absorbs radiation with wavelengths $\lambda \leq 300$ nm which results in the high values of $C_{\lambda,P}$ at these wavelengths. The radiation source of the integrating sphere is limited to wavelengths larger than 350 nm. Therefore, $C_{\lambda,S}$ increases for shorter wavelengths significantly. For wavelengths larger than 650 nm a difference between $C_{\lambda,P}$ and $C_{\lambda,S}$ is observed.

Further investigation in the laboratory have shown that $C_{\lambda,P}$ is significantly affected by stray light in the NIR wavelength range $\lambda \geq 650$ nm due to scattering of radiation within the housing of the calibration setup. Therefore, the housing was coated afterwards with highly absorbing paint reducing the amount of stray light significantly as quantified by further calibrations. The calibration factors obtained for a subsequent experiment MELTEX 2008 (Impact of melt ponds on energy and momentum fluxes between atmosphere and ocean) are given in Figure 4.11b and show the improved agreement of $C_{\lambda,P}$ and $C_{\lambda,S}$. Both calibration factor agree within 5% for wavelengths larger than 400 nm. Nevertheless, the final calibration factors for ASTAR 2007 were merged from both calibration methods using $C_{\lambda,P}$ for $\lambda \leq 420$ nm and $C_{\lambda,S}$ for $\lambda > 420$ nm.

4.1.3 Integration on POLAR 2

For the airborne radiation measurements during ASTAR 2007 the upper and lower sensor unit of the SMART-Albedometer were installed on the AWI research aircraft POLAR 2. Respective certification had to be obtained. Two almost similar sensor bodies were developed by *enviscope GmbH* including a new heating system for Arctic conditions. A technical drawings of the modified upper sensor unit is shown in Figure 4.12. The two optical inlets (1) are mounted on the tilting stage (3) of the horizontal stabilization system which is driven by two perpendicular orientated servo motors (2). The servo motors are covered by an additional heating film and insulating material which protects for low temperatures. The INS (4) is mounted below the tilting stage to measure the attitude of the sensor unit

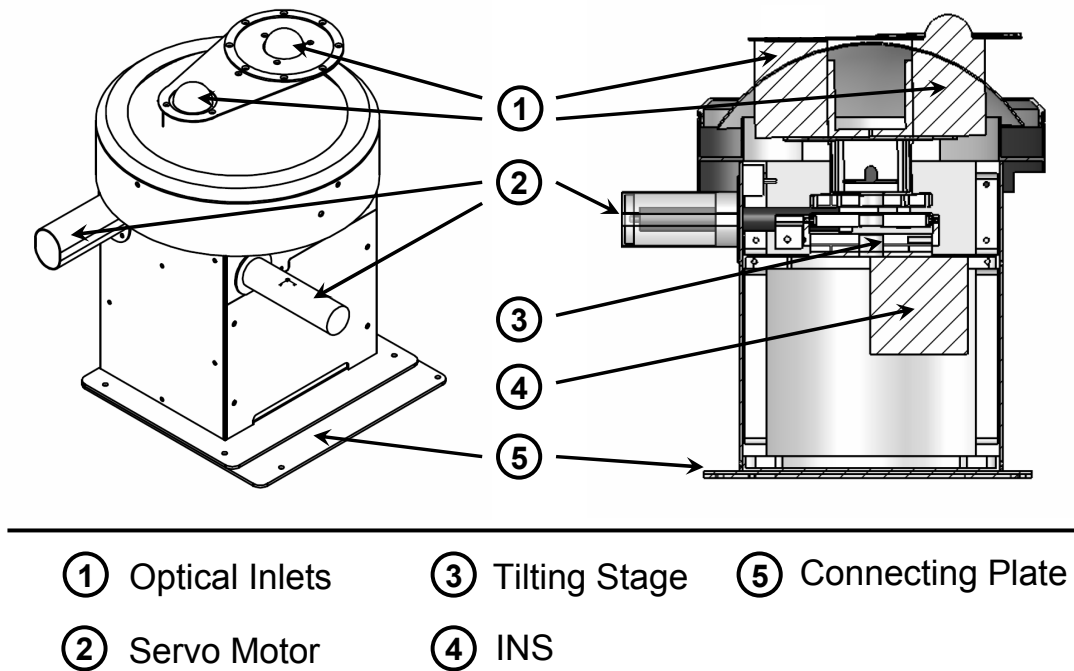


Figure 4.12: Technical drawing of the upper SMART-Albedometer sensor unit used on POLAR 2 (provided by *enviscope GmbH*)

as close as possible to the optical inlets.

The integration of the SMART-Albedometer on POLAR 2 was realized by AWI in cooperation with OPTIMARE Sensorsysteme AG and funded by IfT. The upper sensor body was mounted into a heating compartment in the front part of the POLAR 2 close to already existing broadband radiation sensors (Figure 4.13a). The tubes of the aircraft heating system help to heat the servo motors of the stabilization system. The lower sensor body was mounted on a retractable plate in the tail of POLAR 2 (Figure 4.13b). During takeoff and landing the plate enables to bring the lower sensor inside the aircraft. Therefore, the plate is retracted by a compression spring (3) and additionally fixed by an interlock (1). This is necessary because the front wheel of the POLAR 2 is in one line with the sensors unit which may cause damages of the optical inlets by stirred up gravel.

The certification of the retractable plate by the Federal Aviation Office (Luftfahrt Bundesamt) and the permission of the SMART-Albedometer integration on POLAR 2 was finalized in June 2006.

4.1.4 Configuration

The configuration of the SMART-Albedometer during ASTAR 2007 was chosen such that it provides measurements of downwelling and upwelling spectral irradiance (F_{λ}^{\downarrow} , F_{λ}^{\uparrow}) simultaneously with downwelling zenith and upwelling nadir spectral radiance (I_{λ}^{\downarrow} , I_{λ}^{\uparrow}). The upper and lower sensor unit mounted on POLAR 2 are shown in Figure 4.13c. The optical inlets for the radiance measurements are described above. For the irradiance measurements optical inlets constructed by the Bay Area Environmental Research

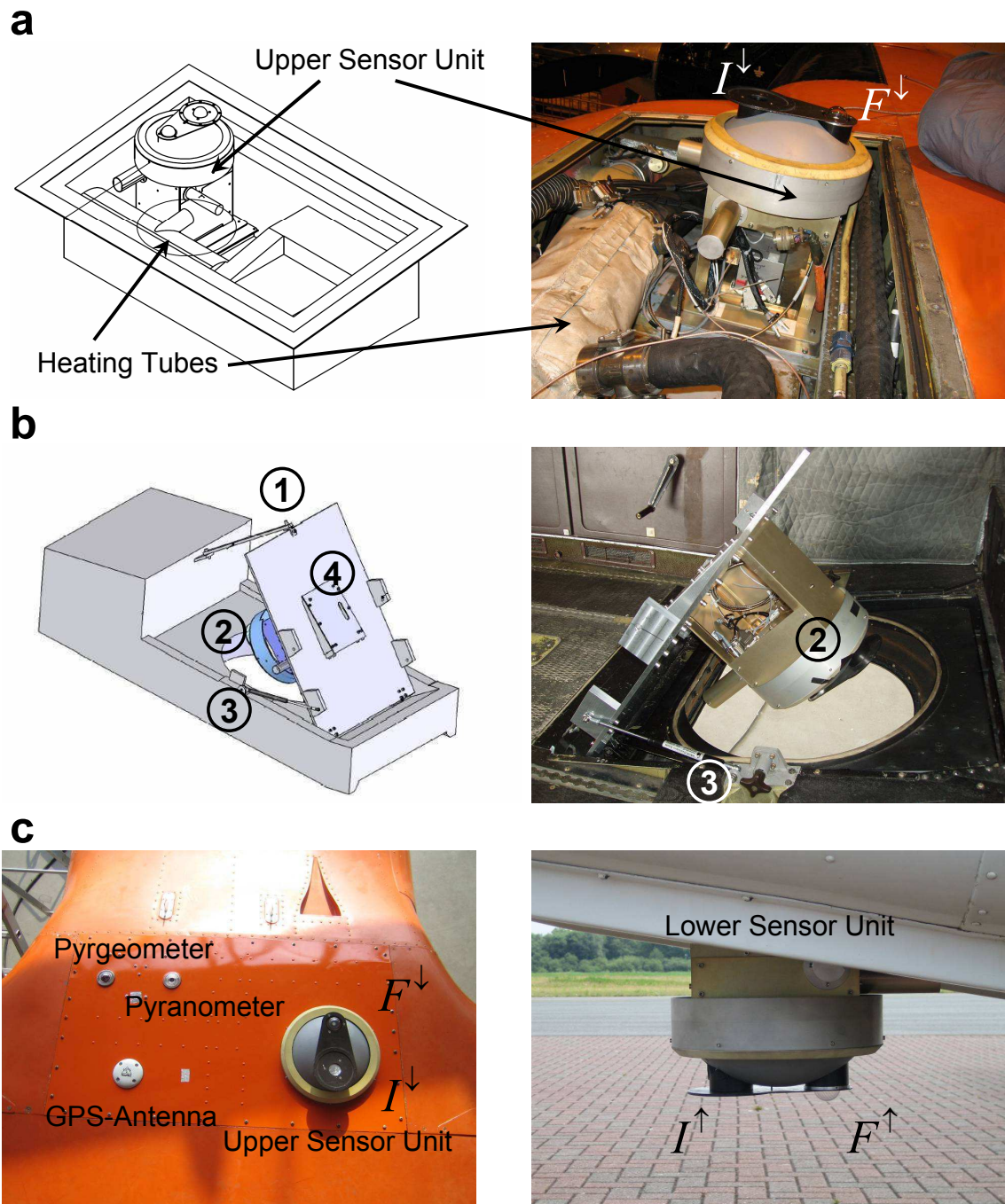


Figure 4.13: Integration of the SMART-Albedometer on the POLAR 2 Aircraft. Panel a shows the mounting of the upper SMART-Albedometer sensor (drawing provided by *enviscope GmbH*); panel b the retractable mounting of the lower SMART-Albedometer sensor (drawing provided by *OPTIMARE*). The numbers indicate (1) the interlock for takeoff and landing, (2) the SMART-Albedometer sensor, (3) the compression spring retracting the plate and (4) the cut-out for the optical fibers. In panel c the final mounting of both sensor units on POLAR 2 is shown.

Table 4.1: Configuration of the SMART-Albedometer during ASTAR 2007.

Spectrometer	System	Wavelength Range	$FWHM$	Irradiance	Radiance
<i>VIS</i>	/ MSC	350–950 nm	2–3 nm	F_{λ}^{\downarrow}	I_{λ}^{\uparrow}
<i>NIR</i>	/ PGS	950–2100 nm	9–16 nm	F_{λ}^{\downarrow}	I_{λ}^{\uparrow}
<i>VIS-II</i>	/ MSC	350–950 nm	2–3 nm	F_{λ}^{\uparrow}	I_{λ}^{\downarrow}

Institute, CA, USA were applied. The inlets were designed as integrating spheres made of Spectralon[®] reflectance material. Sealed with a quartz dome the Spectralon[®] integrating sphere provides an almost wavelength independent photon collection efficiency. A detailed characterization of the performance of these inlets is given in Crowther (1997); Bierwirth (2008). All quantities with corresponding wavelength range measured by the SMART-Albedometer during ASTAR 2007 are summarized in Table 4.1.

Four spectrometer systems (2 x *VIS*, 2 x *NIR*) were applied to measure F_{λ}^{\downarrow} and I_{λ}^{\uparrow} covering the wavelength ranges 350–950 nm (*VIS*) and 950–2100 nm (*NIR*) with a spectral resolution (full width at half maximum, $FWHM$) of 2–3 nm and 9–16 nm. F_{λ}^{\uparrow} and I_{λ}^{\downarrow} were measured with two spectrometer systems (*VIS-II*) in the visible part of the spectrum only (350–950 nm).

From these individual measurements the spectral reflectance $R(\lambda)$ and spectral albedo $\rho(\lambda)$ were derived applying Eqs. 3.11 and 3.12. $R(\lambda)$ was obtained for the wavelength range 350–2150 nm while measurements of $\rho(\lambda)$ are limited to the wavelength range 350–950 nm.

4.1.5 Measurement Uncertainties

A number of sources of error contribute to the uncertainty of the SMART-Albedometer measurements mainly resulting from the spectrometer sensitivity and the different calibrations. As the spectrometer sensitivity and calibration of the measured F_{λ}^{\downarrow} , F_{λ}^{\uparrow} and I_{λ}^{\uparrow} are different the uncertainties of the three measurements are treated separately. The individual errors contributing to each property are listed in Table 4.2 for four wavelengths; two representative for the *VIS* spectrometer and two for the *NIR* spectrometer. The two wavelengths of each spectrometer were chosen in a way that one is located in the range where the sensitivity of the spectrometers is high (650 nm and 1600 nm); the second is located close to the sensitivity minima (350 nm and 2100 nm). All individual sources of error are assumed to be independent. Hence, the overall errors for F_{λ}^{\downarrow} , F_{λ}^{\uparrow} and I_{λ}^{\uparrow} given in Table 4.2 are calculated applying the Gaussian error propagation.

The error of the digital signal obtained by the spectrometer was estimated from the signal to noise ratio (SNR) and the uncertainty in the wavelength calibration. For the *VIS* spectrometer a noise of about two digital counts was estimated independent of wavelength. The *NIR* spectrometers show a higher noise which ranges between 20 and 30 digital counts depending on the wavelength. To calculate the SNR one typical signal obtained during calibration in the laboratories with maximum digital counts of 15,000 for the *VIS* spectrometer and 5,000 for the *NIR* spectromteter was used. At wavelengths with maximum spectrometer sensitivity the resulting SNR indicates a measurement uncertainty of less

Table 4.2: Contribution of individual sources of error to the uncertainties of F_{λ}^{\downarrow} , F_{λ}^{\uparrow} and I_{λ}^{\uparrow} measured by the SMART-Albedometer. The errors are given for four wavelengths representative for the maximum (650 nm and 1600 nm) and minimum (350 nm and 2100 nm) sensitivity of the *VIS* and *NIR* spectrometer. For F_{λ}^{\uparrow} measurements have been conducted only with a *VIS* spectrometer.

Source of Error		$\lambda=350$ nm	$\lambda=650$ nm	$\lambda=1600$ nm	$\lambda=2100$ nm
F_{λ}^{\downarrow}	Spectrometer Signal	6.1 %	1.0 %	1.4 %	8.2 %
	Calibration Lamp	1.1 %	0.6 %	0.3 %	0.3 %
	Transfer Calibration	3.2 %	1.0 %	0.5 %	0.6 %
	Cosine Calibration	3.0 %	3.0 %	3.0 %	3.0 %
	Total	10 %	4 %	3 %	12 %
F_{λ}^{\uparrow}	Spectrometer Signal	1.4 %	1.0 %		
	Calibration Lamp	1.1 %	0.6 %		
	Transfer Calibration	3.5 %	1.1 %		
	Cosine Calibration	1.5 %	1.5 %		
	Total	4 %	2 %		
I_{λ}^{\uparrow}	Spectrometer Signal	5.6 %	1.0 %	2.2 %	20.9 %
	Calibration Lamp	1.1 %	*	*	*
	Reflectance Panel	0.8 %	*	*	*
	Integrating Sphere	*	6.0 %	9.0 %	10.0 %
	Transfer Calibration	11.1 %	1.5 %	1.0 %	1.2 %
	Total	14 %	6 %	10 %	33 %

than 1 % for most parts of the wavelength range. However, at wavelengths $\lambda \leq 380$ nm and $\lambda \geq 1800$ nm where the measured digital signal is weak the error increases up to 20 % at $\lambda \leq 310$ nm and up to 9 % at $\lambda \geq 2100$ nm. Furthermore, the wavelength pixel classification introduces an uncertainty to the measured digital signal. The wavelength pixel classification was determined from the emission lines of neon-mercury and argon-mercury lamps. The error of the wavelength calibration mainly results from the *FWHM* of the spectrometers which reduces the accuracy of the wavelength pixel classification and is assumed to be about 1 %. The overall error of the digital spectrometer signal given in Table 4.2 was calculated by combining the SNR and the uncertainty of the wavelength calibration by applying the Gaussian error combination.

The measurement of the dark current which has to be subtracted from the measured spectrometer signal is associated with an identical error as obtained for the spectrometer signal. Therefore, the error of the digital spectrometer signal given in Table 4.2 is accounted twice for the calculation of the overall measurement uncertainty.

In the laboratory a 1000 W lamp, an integrating sphere and a reflectance panel in combination with the 1000 W lamp have been used for the radiometric calibration. The errors of these radiation standards are certified by external calibration traceable to DKD. For

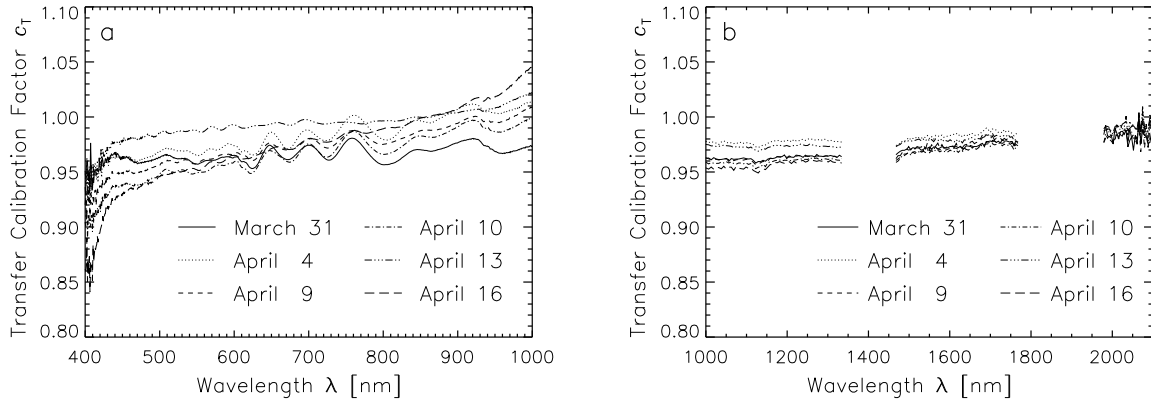


Figure 4.14: Transfer calibration factors c_T obtained for the *VIS* spectrometer (a) and *NIR* spectrometer (b) measuring F_λ^\downarrow .

the 1000 W lamp a wavelength dependent error between 1.1 % at 350 nm wavelength and 0.3 % at 2100 nm wavelength is given. The reflectance panel is certified with uncertainties of 0.8 % at 350 nm and the integrating sphere with uncertainties of 6–10 % between 650 nm and 2100 nm.

During transport and integration of the SMART-Albedometer on the aircraft the sensitivity of the system can change mostly due to the connection and alignment of the optical fibers. To account for these changes secondary calibrations with a small integrating sphere providing a constant source of radiation have been conducted during the laboratory calibration and during ASTAR 2007. The radiometric calibration was corrected by transfer calibration factors c_T defined as the ratio between the secondary calibrations obtained during ASTAR 2007 S_{field} and in the laboratory S_{lab} ,

$$c_T = \frac{S_{\text{lab}}}{S_{\text{field}}}. \quad (4.5)$$

For F_λ^\downarrow the transfer calibration factors for both *VIS* and *NIR* spectrometers are shown in Figure 4.14 for different days. At wavelengths where water vapor absorption varies the measurements c_T is not shown. For most wavelengths c_T is lower than unity which indicates a higher measurement sensitivity during ASTAR 2007 than obtained for the laboratory calibration. The temporal variability of c_T was found to be slightly higher for the *VIS* spectrometers than for the *NIR* wavelength range what reveals a high stability of the *NIR* spectrometers. The error estimated for the transfer calibration was calculated from the standard deviation of all six secondary calibrations obtained in Longyearbyen. The calculated values range at about 1 % for most parts of the wavelength range. Below 400 nm the uncertainties increase up to values of about 11 % especially for the measurements of I_λ^\uparrow .

Furthermore, the measurements of F_λ^\downarrow and F_λ^\uparrow have been corrected for deviations of the irradiance optical inlet from an ideal cosine characteristic as described by Wendisch *et al.* (2002) and in more detail by Wendisch (2002). The error introduced by this correction (cosine error) results mainly from the uncertainties of the laboratory measurements

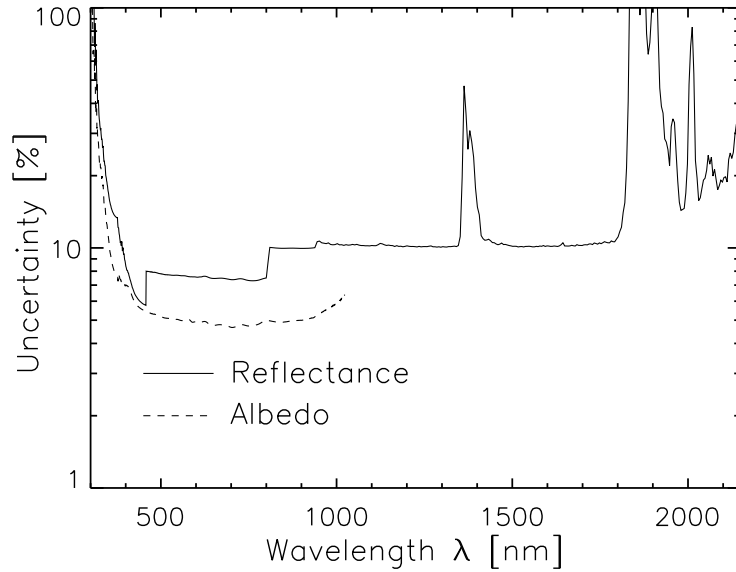


Figure 4.15: Spectral measurement uncertainty for the cloud top reflectance and cloud albedo obtained with the SMART-Albedometer.

performed to characterize the optical inlets. During this calibration the optical inlet is mounted on a turn table to simulate illuminations with different zenith angles. For zenith angles present during ASTAR 2007 (70–80°) a misalignment of the turn table of $\pm 0.2^\circ$ results in a measurement error of about 1.5%. Additionally, the calibration has shown that the cosine characteristic varies with the solar azimuth angle especially for low Sun. This variation and the resulting error amounts up to 2%. Furthermore, during the airborne measurements the misalignment of the optical inlets with respect to a horizontal plane increases the cosine error. The alignment accuracy of the SMART-Albedometer is about $\pm 0.2^\circ$. For solar zenith angle between 70° and 80° this misalignment causes a maximum error of 1.5% (Wendisch *et al.*, 2001). The total cosine error assumed in Table 4.2 amounts to 3% for F_λ^\downarrow and is independent on wavelength. For F_λ^\uparrow the azimuthal and zenith dependence is not relevant. Therefore, the cosine error reduces to 1.5%.

The overall errors for F_λ^\downarrow , F_λ^\uparrow and I_λ^\uparrow were calculated applying the Gaussian error combination and are given in Table 4.2. For the analysis of the SMART-Albedometer measurements cloud top reflectance R and cloud albedo ρ are used. Following Eqs. 3.11 and 3.12 R and ρ include the measurement uncertainty of F_λ^\downarrow , F_λ^\uparrow and I_λ^\uparrow . Therefore, the measurement uncertainty of R and ρ are calculated from the uncertainties of the individual components with Gaussian error combination. The resulting overall uncertainties are shown in Figure 4.15.

For R an uncertainty of about 10% was found for most parts of the wavelength range. Between 400 nm and 800 nm the uncertainty is slightly lower which is mostly due to the stepwise decrease of the uncertainty of the integrating sphere used for the calibration of I_λ^\uparrow . A higher uncertainty of R is found for small wavelengths $\lambda \leq 400$ nm where the spectrometer sensitivity and the intensity of solar radiation significantly decrease. For

the same reasons the uncertainty at wavelengths $\lambda \geq 1800$ nm and in particular in the water vapor absorption bands (1300–1500 nm, 1800–2050 nm) is enhanced with values reaching 100 %. Compared to R the measured ρ shows a lower uncertainty especially for wavelengths larger than 450 nm. Below this wavelength the spectrometer sensitivity decreases and the uncertainties of both R and ρ increase.

Figure 4.15 shows that the SMART-Albedometer measurements at wavelengths $\lambda \leq 500$ nm and within the water vapor absorption bands have to be analyzed with care. Measurements below $\lambda \leq 500$ nm where the spectrometer sensitivity is low are removed from most of the plots shown in the subsequent studies.

4.2 Supplementary Instrumentation

In situ measurements of cloud microphysical properties were obtained from a CPI, introduced by Lawson *et al.* (2001), and with a FSSP-100 (*cf.* Knollenberg, 1976; Wendisch *et al.*, 1996; Gayet *et al.*, 1996). Both instruments were operated by Laboratoire de Météorologie Physique (LaMP), Université Blaise Pascal, AUBIÈRE Cedex, France.

The FSSP detects radiation which is scattered by cloud particles illuminated with a laser beam ($\lambda = 632$ nm). The geometry of the laser beam (2.5 mm length and 0.1 mm diameter) and the true air speed of the POLAR 2 (approx. 80 m s^{-1}) define the sampling volume of the FSSP. It approximately amounts to $20 \text{ cm}^3 \text{ s}^{-1}$. The intensity of the scattered radiation is proportional to the size of the scattering particle. From this relation the cloud particle sizes are obtained. The FSSP measures the particle number size distribution $\frac{dN}{dD}$ in the size range of 3–27 μm with a bin size of 2 μm .

Larger cloud particles were sampled with the CPI which obtains high-resolution digital images of the cloud particles using a 1 million pixel digital Charge-Coupled Device (CCD) camera (2.3 μm). The CCD camera flashes up to 75 frames per second, potentially imaging more than 25 particles per frame. The CPI covers the particle sizes between 23 μm and 2300 μm with a resolution of 23 μm .

Besides the particle size distribution, from both instruments FSSP and CPI total particle number concentration N_{tot} , ice and liquid water content IWC , LWC , particle effective diameter D_{eff} and extinction coefficient b_{ext} were derived. The retrieval and measurement uncertainties of these data are described in detail by Gayet *et al.* (2007).

Unfortunately, the Nevzorov probe mounted on POLAR 2 and measuring bulk liquid and total water content LWC , TWC (in units of g m^{-3}) did not provide reliable measurements due to a broken hot wire. Therefore, LWC and IWC calculated from the particle size distribution measured by FSSP and CPI had to be used in the analysis. In order to present vertical integrated cloud properties the bulk liquid and ice water path LWP , IWP (in units of g m^{-2}) were calculated by:

$$LWP = \int_{z_{\text{base}}}^{z_{\text{top}}} LWC(z) dz, \quad (4.6a)$$

$$IWP = \int_{z_{\text{base}}}^{z_{\text{top}}} IWC(z) dz. \quad (4.6b)$$

From LWP and IWP the ice volume fraction f_{I} characterizing the state of mixing of the mixed-phase clouds is derived by:

$$f_{\text{I}} = \frac{IWP}{IWP + LWP}. \quad (4.7)$$

Optical properties of the cloud particles (volumetric scattering phase function, extinction coefficient and volumetric asymmetry parameter) were derived from the Polar Nephelometer by LaMP (Gayet *et al.*, 1997). It measures the scattering phase function of an ensemble of cloud particles (*i.e.*, water droplets or ice crystals or a mixture of these particles) from a few micrometers to about 800 μm diameter. Therefore, the radiation scattered by cloud particles illuminated by a collimated laser beam (804 nm) is detected at polar angles from about $\pm 3.5^\circ$ to $\pm 173^\circ$ by a circular array of 56 almost uniformly positioned photodiodes. The sampling volume of the Polar Nephelometer is defined by the size of the laser beam (10 mm length and 5 mm diameter) and the true air speed of the POLAR 2 (approx. 80 m s^{-1}). With an acquisition frequency of 10 Hz the sampling volume is 500 cm^3 which corresponds to a detection threshold of 0.5 particles per liter.

The optical properties of the cloud particles (extinction coefficient and volumetric asymmetry parameter) are derived from the direct measurement of the scattering phase function. The asymmetry parameter g is a measure for the anisotropy of the scattering phase function and therefore a powerful tool to discriminate ice crystals and liquid water particles (*cf.* Section 3.3). The asymmetry parameter is defined as the first moment ($n = 0$) of the Legendre expansion of a scattering phase function. From Eq. 3.23 follows,

$$g = b_0 = \frac{1}{2} \int_{-1}^{+1} \mathcal{P}(\cos \vartheta) \cdot \cos \vartheta d \cos \vartheta. \quad (4.8)$$

A value of $g = 1$ describes total forward scattering, $g = -1$ total backward scattering and $g = 0$ isotropic scattering. Depending on the particle size and shape cloud particles show values between 0.7 and 0.9. Due to the integration of the measurements over the sampling volume of the Polar Nephelometer the volumetric asymmetry parameter $\langle g \rangle$ is obtained. It is related to g following the definition of volumetric Legendre moments (Eq. 3.40).

The extinction coefficients measured by the Polar Nephelometer were utilized to define cloudy and cloud free areas in the analysis of the *in situ* measurements. All measurements with $b_{\text{ext}} > 0.05 \text{ km}^{-1}$ were assumed to be cloud free.

The cloud optical thickness τ was calculated from the measurements of b_{ext} using Eq. 3.43.

For the liquid water droplets and ice crystals partial optical thicknesses τ_W and τ_I were derived. These were used to define the ice optical fraction of the mixed-phase clouds by:

$$f_I^* = \frac{\tau_I}{\tau_I + \tau_W}. \quad (4.9)$$

Additional independent information on the cloud thermodynamic phase was provided by the depolarization measurements of AMALi which is a two-wavelengths (532 nm and 355 nm) backscatter lidar with depolarization measurements at 532 nm wavelength. AMALi was installed in nadir looking configuration. The vertical resolution amounts to 7.5 m. The minimum horizontal resolution was about 900 m. Further details of AMALi are described in Stachlewska *et al.* (2004).

For flight missions related to cloud measurements, the flight tracks of POLAR 2 were partly synchronized with satellites overpasses of the Cloud-Aerosol Lidar and Infrared Pathfinder Satellite Observation (CALIPSO) and CloudSat (Winker *et al.*, 2003; Stephens *et al.*, 2002). The Cloud-Aerosol Lidar with Orthogonal Polarization Winker *et al.* (CALIOP, see 2007) on board of CALIPSO provides backscatter coefficient and depolarization measurements of the investigated clouds from which the cloud thermodynamic phase was determined independently.

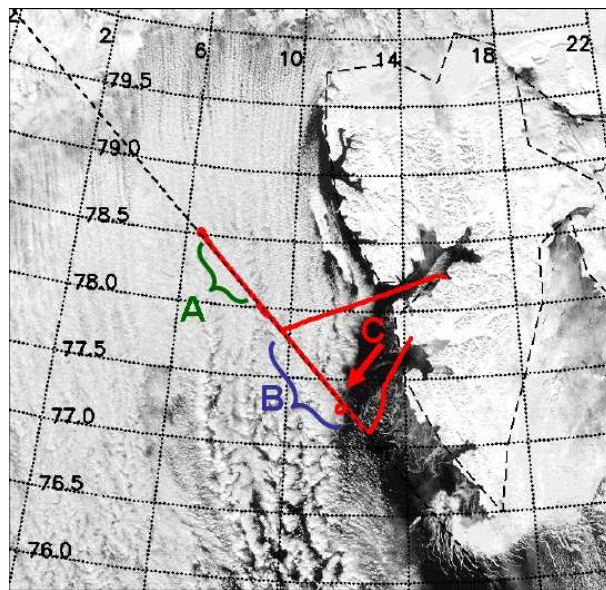


Figure 4.16: MODIS satellite image of April 7, 2007 overlaid with the flight track of POLAR 2 aircraft (flight # 5, red line) along the CALIPSO overpass (dashed black line). Numbers give the latitude and longitude respectively. Flight sections where measurements were analyzed are marked with labels A, B and C. At A a ABM cloud was sampled by both *in situ* instruments and SMART-Albedometer, at C a pure ice cloud has been observed with the SMART-Albedometer only (*cf.* Section 4.3.3). The flight section B is analyzed with regard to cloud thermodynamic phase in Section 6.5

4.3 Overview of ASTAR 2007

Thirteen measurement flights were conducted during ASTAR 2007 (Table 4.3). Five of the flights were devoted to surface reflectance and albedo measurements over snow covered glaciers, open sea and sea ice. Eight flights were performed to sample clouds with *in situ* and remote sensing instruments. For the investigations presented in this work surface reflectance and albedo were derived from measurements on flights # 1, 5, 8 and 11. The investigations on Arctic boundary-layer clouds are based on data obtained during flights with concurrent *in situ* measurements and satellite overpass (# 5 and # 9).

During these flights (April 7–9) a cold air outbreak with northerly winds initiated extended boundary-layer cloud fields over the open Greenland Sea as shown by the MODIS satellite image in Figure 4.16. The convection above the relatively warm open sea allowed the coexistence of ice and liquid water in these clouds. In addition to the predominating ABM clouds, pure ice and pure liquid water clouds have been observed during ASTAR 2007.

4.3.1 *In Situ* Measurements

In situ measurements have been obtained from a total of 16 vertical profiles. Except for two profiles taken at the edge of the cloud fields where pure ice clouds were dominating, the *in situ* measurements generally show the typical structure of the prevailing ABM clouds with a cloud top layer consisting of liquid water and precipitating ice crystals below.

Based on *in situ* data, the particle phase was determined from the combination of asymmetry parameter and particle number concentration measurements. The asymmetry parameter is significantly lower for non spherical ice crystals compared to spherical liquid water droplets (*e.g.*, Gerber *et al.*, 2000; Garrett *et al.*, 2001). As an approximation it was defined that the FSSP (size range 3–27 μm) measured liquid water droplets whereas

Table 4.3: Measurement flights conducted with the SMART-Albedometer during ASTAR 2007.

#	April	Conditions	Satellite	Area	Add. Instruments
1	01.	clear sky	X	north east Svalbard	AMALi
2	02. I	clouds	X	north east Greenland Sea	AMALi
3	02. II	clouds		east Greenland Sea	LaMP
4	03.	clouds		west coast of Svalbard	LaMP, AMALi
5	07. I	clouds	X	east Greenland Sea	LaMP, AMALi
6	07. II	clear sky		south of Svalbard	AMALi
7	08. I	clouds		east Greenland Sea	LaMP, AMALi
8	08. II	clear sky		Storfjord	AMALi
9	09.	clouds	X	north east Greenland Sea	LaMP, AMALi
10	10.	clear sky		Storfjord	AMALi
11	11.	clear sky		east Greenland Sea	AMALi
12	14.	clouds		south east Greenland Sea	LaMP, AMALi
13	16.	clouds		east Greenland Sea	LaMP, AMALi

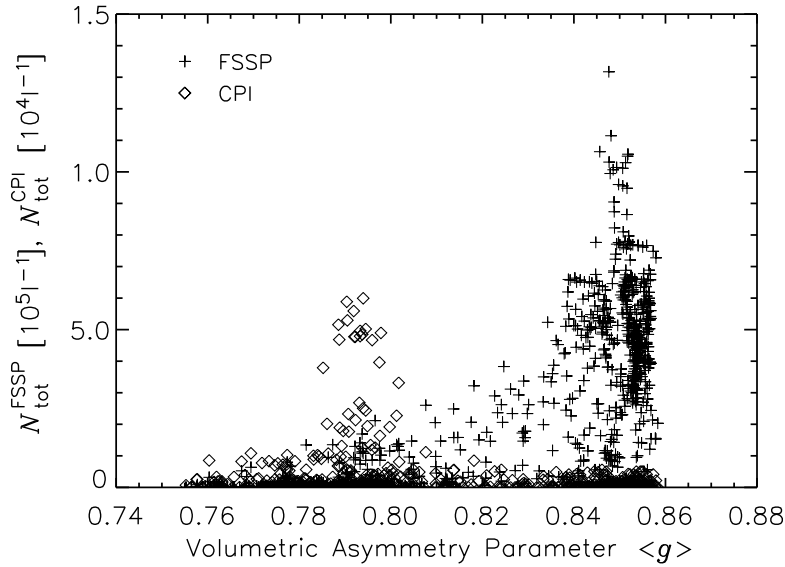


Figure 4.17: Total particle number concentrations measured by FSSP $N_{\text{tot}}^{\text{FSSP}}$ and CPI $N_{\text{tot}}^{\text{CPI}}$ in relation to the volumetric asymmetry parameter $\langle g \rangle$ measured simultaneously by the Polar Nephelometer.

the CPI (23–2300 μm) is used to determine the size distribution of large ice crystals. This assumption is based on the ice crystals sizes expected for mixed-phase conditions (*e.g.*, Korolev *et al.*, 2003; Shupe *et al.*, 2006). Due to the WBF process the ice crystals rapidly grow to sizes larger than the range covered by the FSSP.

Analysis of the simultaneous FSSP, CPI and Polar Nephelometer measurements of total particle number concentration $N_{\text{tot}}^{\text{FSSP}}$ and $N_{\text{tot}}^{\text{CPI}}$ and volumetric asymmetry parameter $\langle g \rangle$ as shown in Figure 4.17 support this assumption. The CPI measured particle number concentrations $N_{\text{tot}}^{\text{CPI}} > 1 \cdot 10^4 \text{ l}^{-1}$ where the asymmetry parameter indicates non-spherical ice crystals ($\langle g \rangle = 0.78\text{--}0.80$). The majority of the FSSP measurements with $N_{\text{tot}}^{\text{FSSP}} > 2 \cdot 10^5 \text{ l}^{-1}$ coincide with $\langle g \rangle = 0.84\text{--}0.86$ indicating liquid water droplets. In the range between $\langle g \rangle = 0.80\text{--}0.84$ only a few measurements of the FSSP show particle number concentration up to $4 \cdot 10^5 \text{ l}^{-1}$. In this intermediate range it has to be considered that following Eq. 3.40 a low concentration of large ice crystals (large scattering cross section) may contribute stronger to the volumetric asymmetry parameter than a high concentration of liquid water droplets (small scattering cross section).

A typical profile of measured particle number concentrations, LWC , IWC and asymmetry parameter obtained on flight # 5 between 78.0°N and 78.5°N (*cf.* Figure 4.16 label A) is given in Figure 4.18. The FSSP indicated particle concentrations and LWC up to $N_{\text{tot}}^{\text{FSSP}} = 50 \text{ cm}^{-3}$ and $LWC = 115 \text{ mg l}^{-1}$ between 1000–1700 m altitude. In the same layers the asymmetry parameter measured by the Polar Nephelometer, was about 0.85 which is a typical value for spherical liquid water droplets (*e.g.*, Gerber *et al.*, 2000; Garrett *et al.*, 2001). A thin layer dominated by ice crystals was found between 800 m and 1100 m indicated by lower asymmetry parameters. In this layer the CPI measured particle

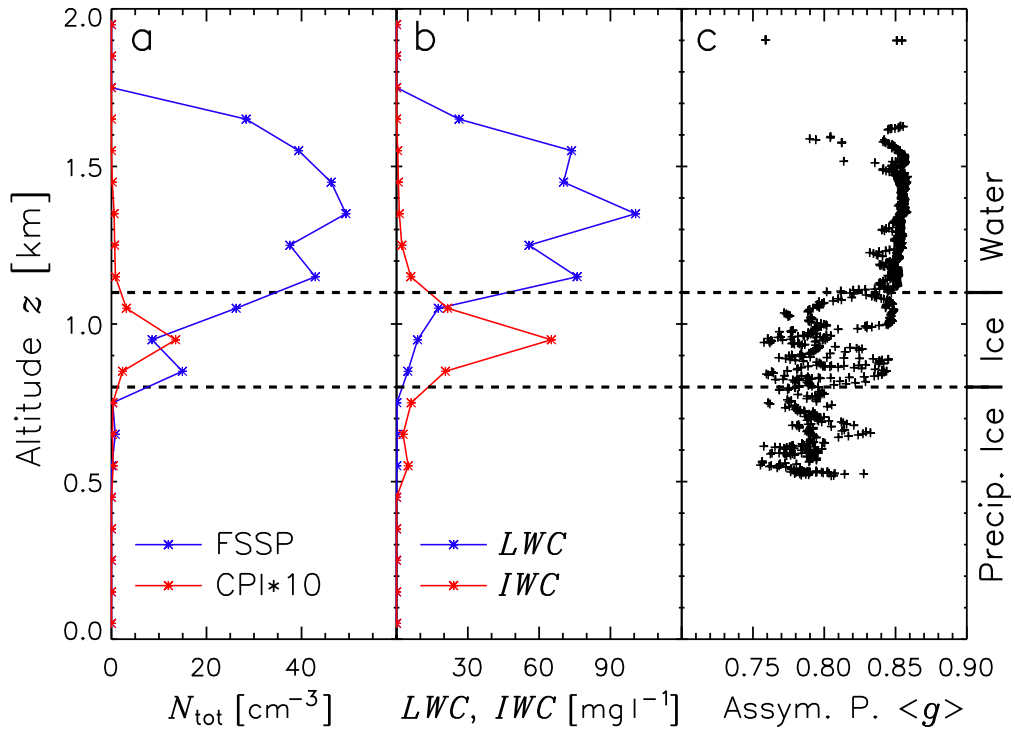


Figure 4.18: Profile of microphysical measurements obtained on flight #5. Total particle number concentration N_{tot} measured by FSSP and CPI are given in panel a; LWC and IWC in panel b. The volumetric asymmetry parameter $\langle g \rangle$ obtained from the Polar Nephelometer is shown in panel c.

number concentrations of up to $N_{\text{tot}}^{\text{CPI}} = 1.5 \text{ cm}^{-3}$ with maximum particle dimensions of up to $1000 \mu\text{m}$. Although the ice crystal number concentration is about a magnitude lower than the liquid water droplet concentration the ice crystals dominate the total water content with $IWC = 70 \text{ mg l}^{-1}$. Below this layer, precipitating large ice particles have been observed down to 500 m by visual observation on board the aircraft and from *in situ* measurements (low ice water content and asymmetry parameter).

The profile of asymmetry parameter (Figure 4.18b) shows a distinct transition between $\langle g \rangle \geq 0.83$ related to liquid water droplets and $\langle g \rangle \leq 0.80$ related to ice crystals. Only a few measurements show intermediate values. As Garrett *et al.* (2001) have shown the asymmetry parameter measured in Arctic stratus changes linearly from 0.86 to 0.76 depending on the fractional number of particles in the cloud that are ice rather than liquid. Therefore, the measurements presented in Figure 4.18b reveal that liquid water droplets are dominant in the upper cloud layer and ice crystals mostly occur near cloud base.

This vertical structure is typical for the Arctic stratus clouds observed during ASTAR 2007 and agrees with previous field campaigns (*e.g.*, Pinto, 1998; McFarquhar *et al.*, 2007). Cloud resolving numerical simulations of Arctic stratus confirm the typical layering with liquid water droplets at cloud top and precipitating ice crystals below (*e.g.*, Harrington *et al.*, 1999; Fridlind *et al.*, 2007).

The particle number size distribution $\frac{dN}{dD}$ vertically averaged for the profile given in Figure 4.18 is shown in Figure 4.19 for the FSSP and CPI measurements. The FSSP measurements reveal a two modal distribution of the liquid water droplets with two maxima for diameters of $5 \mu\text{m}$ and $17 \mu\text{m}$. The contribution of the small particles results mainly from measurements at cloud top (not shown here).

Investigations on FSSP measurements and similar *in situ* probes have shown that in the presence of large ice crystals shattering of the ice crystals at the tip of the instrument housing may occur and produce numerous smaller particles (Field *et al.*, 2003; Korolev and Isaac, 2005). The same effect has been observed by Glantz *et al.* (2003) for large liquid water droplets and may explain the presence of small particle in the measurements presented here. However, this small particle mode has not been observed for other profiles measured during ASTAR 2007. Therefore, it is not clear which process did produce these particles.

However, for radiative investigation the particle effective diameter D_{eff} is most important, characterizing the magnitude of absorption by the particle population. D_{eff} is defined by the ratio between particle volume $V(D)$ and geometric cross section $A(D)$ (*e.g.* Mitchell, 2002),

$$D_{\text{eff}} = \frac{3 \int \frac{dN}{dD}(\tilde{D}) \cdot V(\tilde{D}) d\tilde{D}}{2 \int \frac{dN}{dD}(\tilde{D}) \cdot A(\tilde{D}) d\tilde{D}} \quad (4.10)$$

For the particle size distribution presented here the contribution of the small particles to D_{eff} is negligible compared to the larger particles. For the liquid water particles measured by the FSSP a mean effective diameter $D_{\text{eff}} = (15 \pm 5) \mu\text{m}$ was derived.

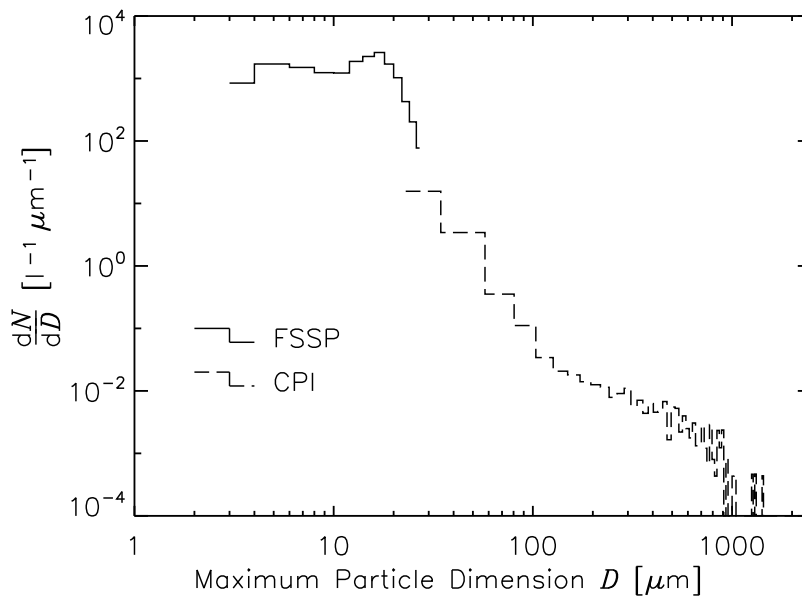


Figure 4.19: Mean particle number size distribution $\frac{dN}{dD}$ measured by FSSP and CPI within the cloud profiled on flight # 5 (c.f. Figure 4.18).

The CPI measurements representative for the ice crystal population show an almost exponential decrease of $\frac{dN}{dD}$ with increasing D . Ice crystals up to a maximum particle dimensions of about $1000 \mu\text{m}$ have been observed mainly at lower cloud parts corresponding to precipitating ice. The calculated mean effective diameter of the ice crystals amounts $(85 \pm 37) \mu\text{m}$ for the entire cloud. In the cloud layer dominated by ice crystals (800–1200 m) larger ice crystals with $D_{\text{eff}} = (103 \pm 36) \mu\text{m}$ have been observed.

4.3.2 Airborne Lidar Measurements

The laser of the AMALi lidar did not completely penetrate the optically thick clouds. However, AMALi did identify a liquid water layer at cloud top by the depolarization signal. Although multiple scattering in the liquid water layer generated high depolarization values, comparable to the depolarization signal of ice crystals, the detailed analysis of the lidar profiles averaged over 15 seconds reveals differences in the vertical pattern of the depolarization. The depolarization related to multiple scattering of liquid water particles increases slowly with cloud depth whereas nonspherical ice crystals result in an instantaneous increase of the depolarization (Hu *et al.*, 2007). From this analysis the precipitating ice below the clouds was identified in several cloud gaps.

4.3.3 Radiation Measurements

Beside the typical ABM clouds also pure ice and pure liquid water clouds have been observed during ASTAR 2007. Cloud top reflectances R for exemplary samples of the three cloud types are shown in Figure 4.20a. The mixed-phase and ice cloud have been observed on flight # 5 as indicated by the labels A and C in Figure 4.16. These measurements were taken at 1800 m altitude approximately 200 m above cloud top. The water cloud was sampled at 2700 m altitude on flight # 6 between 75.4°N , 11.5°E and 75.8°N , 11.8°E . All measurements shown here are averaged over the time period the clouds have been sampled (mixed-phase cloud 18 min, water cloud 8 min and ice cloud 2 min).

Especially the liquid water cloud shows differences of R in the wavelength range between 500 nm and 1300 nm as shown in Figure 4.20a. These differences result from different cloud optical thickness τ . For the clouds presented here τ was retrieved by applying standard retrieval techniques (Nakajima and King, 1990). The mixed-phase cloud assumed as liquid water cloud for the retrieval has a τ of 12, while for the ice and pure liquid water cloud $\tau = 15$ and $\tau = 4$ was found, respectively. The cloud optical thickness of the mixed-phase cloud estimated from the *in situ* measurements of extinction coefficients was about 8.

In the wavelength range 1450–1800 nm and 1900–2150 nm (highlighted gray in Figure 4.20) where R depends less of τ and water vapor absorption is weak the spectral pattern of the cloud top reflectance reveals significant differences. These are caused by the contrast in the imaginary part \tilde{n}_i of the refractive index (proportional to absorption) of ice and liquid water shown in Figure 4.20b. The pure ice cloud shows the lowest R values at 1500 nm and 2050 nm where \tilde{n}_i of ice has a maximum. Between 1500 nm and 1750 nm R strongly increases to values similar to the pure liquid water and mixed-phase cloud.

Here both liquid water and ice have a minima of \tilde{n}_i . In the same wavelength range the measurements above the pure liquid water and mixed-phase cloud show only a slight slope of R corresponding to the weak absorption of water (low \tilde{n}_i).

Simultaneous to the cloud top reflectance, the cloud albedo ρ was obtained for the pure ice and mixed-phase cloud introduced in Figure 4.20a. In Figure 4.21 for these cases the simultaneous measurements of R and ρ are compared. Generally, Figure 4.21 reveals that ρ is larger than R indicating a nonisotropic radiation field above the clouds (isotropy for $\rho = R$). Although, both clouds have been observed at similar solar zenith angle of $\theta_0 = 71^\circ$ and had a similar optical thickness (similar magnitude of R), the difference between R and ρ are smaller for the ice cloud than for the mixed-phase cloud. The reflected radiation above the ice cloud is more isotropic than above the mixed-phase cloud. These differences can be explained by differences in the scattering phase functions of liquid water particles and ice crystals. Assuming single scattering at the cloud top with $\theta_0 = 71^\circ$ the enhanced sideward scattering of ice crystals (*cf.* Figure 3.4) results in a more isotropic radiation field reflected by the ice cloud than by the mixed-phase cloud.

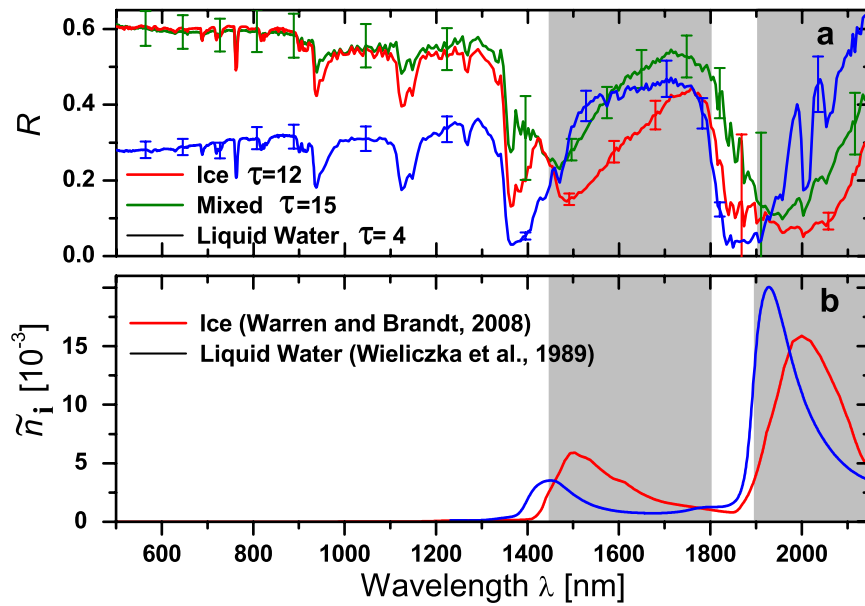


Figure 4.20: Examples of measured cloud top reflectance R (flight #5 and #6) over a pure ice cloud ($\tau = 12$), pure liquid water cloud ($\tau = 4$) and mixed-phase cloud ($\tau = 15$) are given in panel a. Error bars indicate the measurement uncertainty of the reflectance measurements. Panel b shows the imaginary part \tilde{n}_i of the refractive index for ice and liquid water.

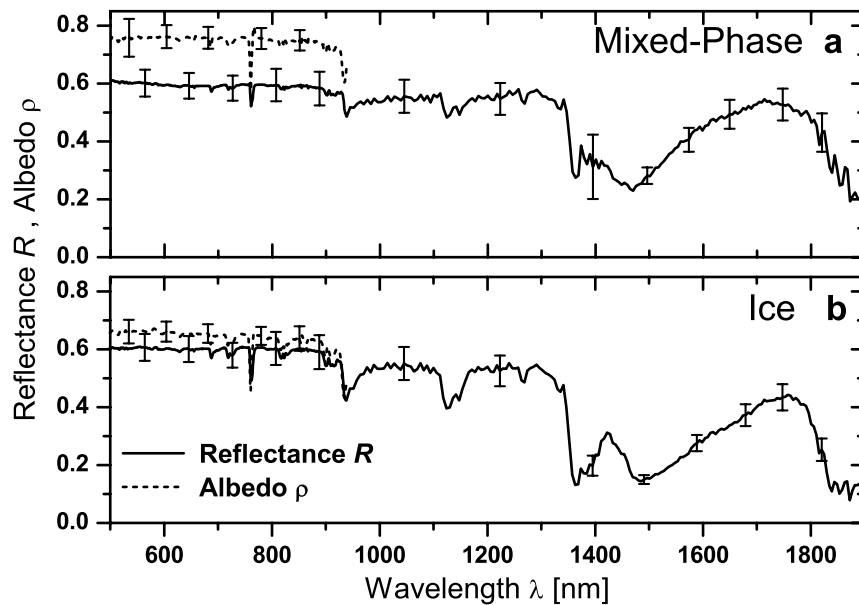


Figure 4.21: Cloud top reflectance R and cloud albedo ρ measured on flight #5 above a mixed-phase cloud (a) of ($\tau = 15$) and a pure ice cloud (b) of ($\tau = 12$) introduced in Figure 4.20.

5 Radiative Transfer in Arctic Boundary-Layer Mixed-Phase Clouds

To estimate the solar and IR radiative forcing of ABM clouds radiative transfer simulations have been performed. To represent the cloud in the radiative transfer model *in situ* measurements of microphysical cloud properties (flight # 5), were used. The simulations were analyzed with respect to the impact of the properties of the ice phase (ice fraction, ice crystal effective diameter, ice crystal shape). In the following sections the radiative transfer model applied for these studies is described and how the mixed-phase clouds were included into the model. From the results of the simulations the cloud radiative forcing was calculated and discussed in Section 5.5. In Section 5.6 the impact of the ice crystal shape on cloud radiative properties is investigated. Furthermore, simulations of the cloud top reflectance and albedo are analyzed in Section 5.7 with regard to their spectral variability.

5.1 Radiative Transfer Model

The spectral solar and IR radiative transfer simulations were performed with the *libRadtran* (library for Radiative transfer) code by Mayer and Kylling (2005). The *libRadtran* package provides a powerful tool to simulate the 1D radiative transfer through plan-parallel mixed-phase clouds by allowing a separate input for the ice and water mode of the cloud. Changes to one mode only can be applied without changing the input of the other. This reduces the required preparation of the model input drastically. For the numerical solution of the solar simulations the discrete ordinate radiative transfer solver DISORT version 2.0 by Stamnes *et al.* (1988) was applied. DISORT 2.0 contains the Delta-M method as described in Section 3.4.2 and additionally the intensity correction proposed by Nakajima and Tanaka (1988). Therefore, DISORT 2.0 is highly suitable for simulations of spectral radiances for which the scattering phase function of the cloud particles has to be represented in the simulation with high accuracy. The IR simulations were performed with a two-stream radiative solver described by Kylling *et al.* (1995).

5.1.1 Basic Model Input

The meteorological input (profiles of static air temperature, relative humidity and static air pressure) was composed of a radio sounding at Ny Ålesund/Svalbard (April 7, 2007,

Table 5.1: Surface albedo measured during ASTAR 2007

Albedo Typ	Flight #	Geogr. Pos.	θ_0	Flight Altitude
snow covered glacier	1	19.6° E, 79.9° N	75.1°	1650 m
fresh sea ice	8	18.4° E, 77.1° N	79.2°	2700 m
open water (clear sky)	11	12.7° E, 77.2° N	73.0°	30 m
open water (overcast)	5	10.8° E, 77.6° N	73.0°	200 m

11:00 UTC). Above 33 km altitude a subarctic winter profile (Anderson *et al.*, 1986) was used. The aerosol microphysical properties were taken from Shettle (1989). The spring-summer maritime aerosol profile was chosen for the boundary-layer; background aerosol conditions were applied for the altitudes above. The aerosol optical thickness was scaled by the Ångström formula with an Ångström exponent of $\alpha_A = 1.51$ and an aerosol optical thickness at $1 \mu\text{m}$ wavelength of $\beta_A = 0.03$. Both coefficients have been obtained from sun photometer measurements at Ny Ålesund on April 7, 2007 using a SP1A sun photometer (Herber *et al.*, 2002). If not stated otherwise, the simulations were conducted for a solar zenith angle of $\theta_0 = 71^\circ$ similar to the conditions during the radiation measurements of the investigated clouds presented in Section 4.3.3.

5.1.2 Surface Albedo

As lower boundary condition the radiative transfer simulations require an appropriate surface albedo. During ASTAR 2007 albedo and reflectance measurements have been obtained with the SMART-Albedometer above different surfaces representative for the Arctic. The data include a snow-covered glacier field, fresh sea ice and open sea water under clear sky and overcast conditions. The geographic position, flight altitude and solar zenith angle θ_0 for which the data was measured is summarized in Table 5.1. The albedo measured at flight altitude was extrapolated to the surface albedo using an iterative extrapolation algorithm presented by Wendisch *et al.* (2004). The simulations have shown that for the clean Arctic air with low aerosol concentrations, the low flight altitudes and the high albedo values above snow or ice the corrections by the extrapolation can be neglected. The results of the first iteration step ranged at albedo values within the uncertainty of the measured albedo.

The spectral albedo ρ and nadir reflectance R of the four different surface types are given in Figure 5.1. Measurements within absorption bands of atmospheric gases (H_2O , CO_2 , O_2)

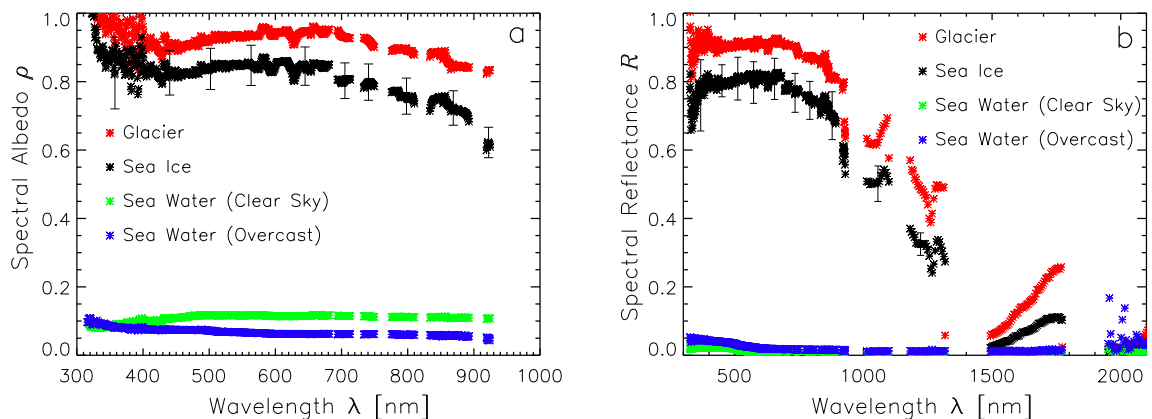


Figure 5.1: Surface albedo ρ (a) and reflectance R (b) measured during ASTAR 2007 above representative surfaces (c.f. Table 5.1). Wavelengths including absorption bands of atmospheric gases (H_2O , CO_2 , O_2) were excluded from the graph. Exemplarily, for the sea ice albedo and reflectance error bars indicate the measurement uncertainties.

were excluded from the plot. At these wavelengths only a weak radiation signal in the range of the signal to noise ratio is measured. This causes a high uncertainty of ρ and R (*cf.* Section 4.1.5).

Above the snow-covered glacier and sea ice the albedo reaches the highest values close to unity, whereas the water surfaces reflect less incoming radiation. This reveals the high contrast of surface albedo in Arctic regions where open water and sea ice are located side by side.

In the surface reflectance measurements which cover a wider wavelength range the absorption bands of ice with maxima at 1250 nm, 1500 nm and 2000 nm are prominent. For wavelengths larger than 900 nm the ice and liquid water absorption increases and therefore the reflectance values decrease. Around 1750 nm a local minimum of the ice absorption results in a slightly higher reflectance. Contrarily, the reflectance above sea water is close to zero for almost all wavelengths, except for wavelengths lower than 500 nm which indicated the blue color of water.

According to the observed cloud (flight # 5) for the radiative transfer simulations shown in this work the surface albedo of open water and overcast condition was applied. In the IR radiative transfer simulations the surface temperature was set to 0° C.

5.1.3 Cloud Properties

The model input for the cloud optical properties includes the volume extinction coefficient $b_{\text{ext}}^{I/W}$, volumetric single-scattering albedo $\langle \tilde{\omega} \rangle^{I/W}$, the volumetric scattering phase function $\langle \mathcal{P}(\vartheta) \rangle^{I/W}$ (solar simulations) and the volumetric asymmetry parameter $\langle g \rangle^{I/W}$ (IR simulations) calculated separately for the ice mode (suffix I) and liquid water mode (suffix W) as described in Section 3.5. The *libRadtran* package internally combines the optical properties of the ice and liquid water mode applying the standard mixing formulas (*e.g.*, Sun and Shine, 1994):

$$b_{\text{ext}} = b_{\text{ext}}^I + b_{\text{ext}}^W, \quad (5.1a)$$

$$\langle \tilde{\omega} \rangle = \frac{\langle \tilde{\omega} \rangle^I \cdot b_{\text{ext}}^I + \langle \tilde{\omega} \rangle^W \cdot b_{\text{ext}}^W}{b_{\text{ext}}} \quad (5.1b)$$

$$\langle \mathcal{P}(\vartheta) \rangle = \frac{\langle \tilde{\omega} \rangle^I \cdot b_{\text{ext}}^I \cdot \langle \mathcal{P}(\vartheta) \rangle^I + \langle \tilde{\omega} \rangle^W \cdot b_{\text{ext}}^W \cdot \langle \mathcal{P}(\vartheta) \rangle^W}{b_{\text{ext}} \cdot \langle \tilde{\omega} \rangle}, \quad (5.1c)$$

$$\langle g \rangle = \frac{\langle \tilde{\omega} \rangle^I \cdot b_{\text{ext}}^I \cdot \langle g \rangle^I + \langle \tilde{\omega} \rangle^W \cdot b_{\text{ext}}^W \cdot \langle g \rangle^W}{b_{\text{ext}} \cdot \langle \tilde{\omega} \rangle}. \quad (5.1d)$$

In order to represent the anisotropic scattering phase function of cloud particles in the solar radiative transfer simulations the Delta-M method was applied as described in Section 3.4.2. The exact phase function was expanded into 1024 Legendre coefficients for both ice crystals and liquid water droplets. Additional simulations have shown that the Delta-fit method introduced in Section 3.4.3 can lead to inaccurate results. With the

reduced number of Legendre coefficients obtained by the Delta-fit method problems occur if the strong forward scattering peak of the scattering phase function is redistributed into the direct solar radiation. This is an appropriate assumption considering single scattering only. However, for multiple scattering processes this assumption can lead to an incorrect angular distribution of the scattered radiation above cloud top and therefore alters the simulated cloud top reflectance. As the clouds investigated within this work are optically thick, multiple scattering processes have to be considered. Therefore, the application of the Delta-fit method was omitted in this work.

5.2 Optical Properties of Individual Ice Crystals

The investigations take into account ice crystals of five different shapes (sphere, aggregate, column, plate, bullet rosette) illustrated in Figure 5.2. Results are shown for the two extreme cases (columns, aggregates) and for spherical crystals as reference. The different optical properties of the individual ice crystals (extinction cross section b_{ext} , single-scattering albedo $\tilde{\omega}$, asymmetry parameter g and scattering phase function \mathcal{P}) were supplied by Yang and Liou (1996a) and Yang *et al.* (2005) in the form of a digital library (hereafter referred as PY-database). Yang and Liou (1996a) used a combination of methods including an Improved Geometric Optics Method (IGOM) to obtain the properties of the nonspherical ice crystals for solar wavelengths. The data are available for 40 maximum particle dimensions between $5\ \mu\text{m}$ and $1500\ \mu\text{m}$ and 165 wavelengths in the range 300–2300 nm.

Yang *et al.* (2005) used similar methods to calculate the ice crystal properties in the IR wavelength range between $3\ \mu\text{m}$ and $100\ \mu\text{m}$. The look-up tables are calculated for 49 wavelengths including 45 ice crystal sizes between 2 and $10,000\ \mu\text{m}$. Single-scattering properties of spherical ice crystals and water droplets for the same wavelengths (solar and IR) and particle diameters have been obtained by Mie-theory (Bohren and Huffman, 1998).

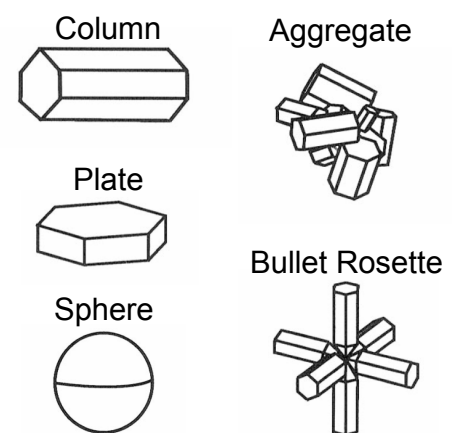


Figure 5.2: Ice crystal shapes included in the PY-database.

5.3 Cloud Microphysical Properties

The simulations presented here are based on a stratiform cloud layer observed during the ASTAR campaign on flight # 5 (*cf.* Section 4.3). The cloud was situated between 800 m and 1600 m altitude above the sea surface. The *in situ* measurements showed the simultaneous occurrence of ice and liquid water particles with an ice water path of $IWP = 17\ \text{g m}^{-2}$ and a liquid water path of $LWP = 35\ \text{g m}^{-2}$. The ice volume fraction f_I amounts 0.33. Effective particle diameter of $D_{\text{eff}}^I = 103\ \mu\text{m}$ for the ice crystals

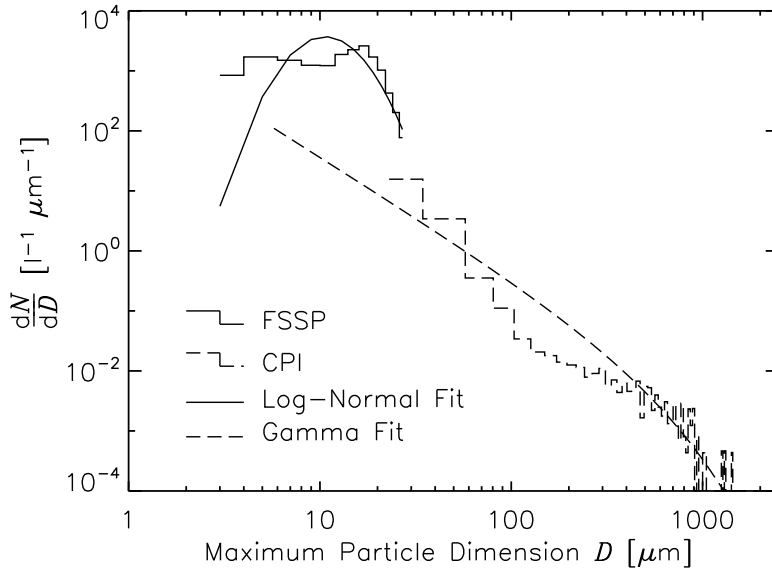


Figure 5.3: Liquid water mode NSD fitted as log-normal distribution to the FSSP measurements presented in Section 4.3.1. The ice mode NSD was fitted as gamma-distribution to the appropriate CPI measurements.

and $D_{\text{eff}}^{\text{W}} = 15 \mu\text{m}$ for the liquid water particles were measured. The cloud optical thickness estimated from the *in situ* measurements was $\tau = 8$ with partial optical thicknesses of the ice and water mode of $\tau_{\text{I}} = 0.5$ and $\tau_{\text{W}} = 7.5$. This corresponds to an ice optical fraction f_{I}^* of 0.06.

For simplification the model cloud was assumed as plan parallel, homogeneously mixed cloud consisting of one layer. The neglect of vertical variations allows to study the effects of the ice crystals on radiative transfer without interaction of effects resulting from the cloud vertical structure. This issue will be addressed in detail in Section 7.

For the construction of the mixed-phase cloud two separate modes of cloud particle number size distributions (NSDs) for liquid water droplets and ice crystals were assumed (called water and ice mode in the subsequent text). A separate treatment of the liquid water droplets and ice crystals enables an easy variation of ice crystal shape, ice crystal and liquid water particle effective diameter in the radiative transfer simulations. Additionally it allows to vary the ice volume fraction f_{I} or ice optical fraction f_{I}^* of the mixed-phase cloud.

5.3.1 Liquid Water Mode

The NSD of the liquid water particles obtained from FSSP measurements was fitted to a log-normal distribution (*e.g.*, Miles *et al.*, 2000). The representation by a theoretical function has the advantage to allow systematic changes of the particle properties ($D_{\text{eff}}^{\text{W}}$, total particle number concentration $N_{\text{tot}}^{\text{W}}$). The log-normal distribution is defined by the three parameters total number concentration $N_{\text{tot}}^{\text{W}}$, median diameter D_{M}^{W} and logarithmic

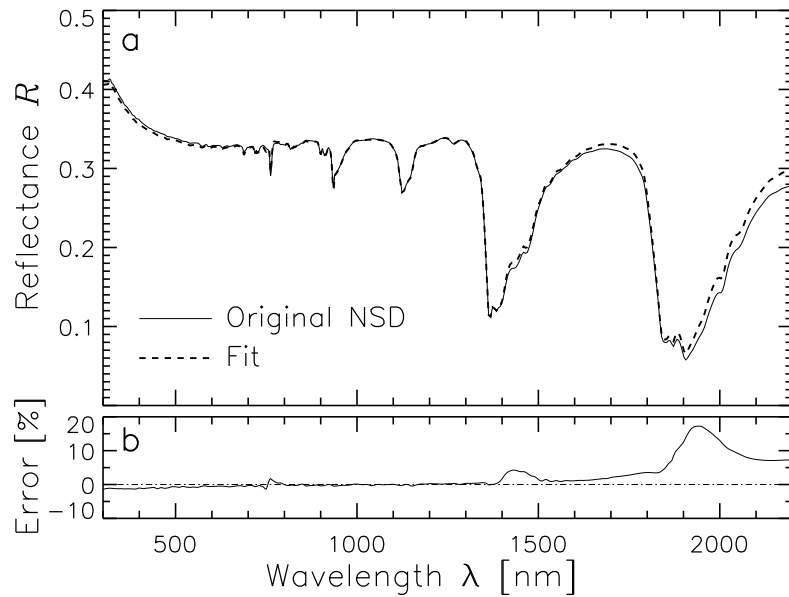


Figure 5.4: Cloud top reflectance R simulated by using the measured NSD and the NSD fitted to theoretical functions (a). In panel b the relative difference between both simulations is given.

width σ (with D the maximum particle dimension),

$$\left(\frac{dN}{dD}\right)^W = \frac{N_{\text{tot}}^W}{\sqrt{2\pi} \cdot \sigma \cdot D} \cdot \exp\left[-\frac{(\ln D - \ln D_M^W)^2}{2\sigma^2}\right]. \quad (5.2)$$

For spherical particles the median diameter D_M^W is directly linked to the effective diameter D_{eff}^W by,

$$D_{\text{eff}}^W = D_M^W \cdot \exp\left[\frac{5}{2}\sigma^2\right]. \quad (5.3)$$

For the measured NSD $D_{\text{eff}}^W = 15 \mu\text{m}$, $N_{\text{tot}}^W = 3.3 \cdot 10^3 \text{ cm}^{-3}$ and $\sigma = 0.35$ were found. These values agree with data collected by previous measurements summarized by Korolev and Mazin (1993) and Miles *et al.* (2000). From the measurements by Korolev and Mazin (1993) including marine mixed-phase clouds at higher latitudes $D_{\text{eff}}^W = 16.4 \mu\text{m}$ and $\sigma = 0.19$ were obtained. Miles *et al.* (2000) calculated mean values of $D_{\text{eff}}^W = 19.2 \pm 4.7 \mu\text{m}$ and $\sigma = 0.38 \pm 0.13$ representative for marine low-level stratiform clouds.

The log-normal distribution obtained from the fit to the FSSP measurements is given in Figure 5.3. The fitted NSD was calculated for particle range 3–28 μm covered by the FSSP measurements. Differences to the measured NSD result mainly from the bimodal character of the measured NSD. However, the shape of the NSD has a minor impact on the radiative transfer which is mainly characterized by the effective diameter of the NSD and the corresponding cloud optical thickness determined by N_{tot}^W .

A comparison between simulations using the measured NSDs and the NSDs fitted to theoretical functions is given in Figure 5.4. The differences of the simulated cloud top reflectances R range below 2% for wavelengths smaller than 1400 nm and below 4% in the

range 1500–1850 nm. Larger differences up to 20 % occur where the liquid water and ice absorption bands coincide with water vapor absorption bands (1400–1500 nm and 1850–2200 nm). These are not crucial for the investigations on the energy budget presented here. Less than 3 % of the broadband solar F^\downarrow is covered by this wavelength range which does not significantly contribute to the solar energy budget.

5.3.2 Ice Mode

According to the water mode, the NSD of the ice crystals measured by the CPI was fitted to a theoretical gamma-distribution (Chylek *et al.*, 1992; Heymsfield *et al.*, 2002) It is specified by the three constants $\hat{\alpha}$, $\hat{\beta}$ and $\hat{\gamma}$,

$$\left(\frac{dN}{dD}\right)^I = \hat{\gamma} \cdot D^{\hat{\alpha}} \cdot \exp\left[-\hat{\beta} \cdot D\right]. \quad (5.4)$$

Thereby, $\hat{\alpha}$ characterizes the shape of the gamma-distribution. All three parameters can be related to the total particle number concentration N_{tot}^I and the ice crystal effective diameter D_{eff}^I ,

$$N_{\text{tot}}^I = \hat{\gamma} \cdot \frac{\Gamma(\hat{\alpha} + 1)}{\hat{\beta}^{\hat{\alpha}+1}}, \quad (5.5)$$

$$D_{\text{eff}}^I = \frac{\hat{\alpha} + 3}{\hat{\beta}}. \quad (5.6)$$

It has to be pointed out, that the relation for D_{eff}^I holds only for the assumption of spherical ice crystals. For nonspherical ice crystals D_{eff}^I was calculated using the definition given in Eq. 4.10.

The corresponding gamma-distribution obtained from the fit to the CPI measurements is shown in Figure 5.3. To cover the size range of the CPI the NSD was calculated for ice crystal diameters between 5–2300 μm . The best fit assuming column shaped ice crystals was derived for $\hat{\alpha} = -2.0$, $D_{\text{eff}}^I = 103 \mu\text{m}$ and $N_{\text{tot}}^I = 1.5 \cdot 10^3 \text{l}^{-1}$. This agrees well with the range of ice crystal effective diameter reported by Korolev *et al.* (2003); Shupe *et al.* (2008b). From *in situ* measurements in Arctic mixed-phase clouds Korolev *et al.* (2003) found ice crystals in the range of $D_{\text{eff}}^I = 86\text{--}151 \mu\text{m}$. The ice crystal effective diameter retrieved by Shupe *et al.* (2008b) from ground based radar observations during the M-PACE experiment ranges between 64 μm and 120 μm with a mean value of 92 μm .

5.4 Mixing of Ice and Liquid Water Mode

To analyze the solar radiative forcing of mixed-phase clouds the state of mixing and the ice crystal shape are changed in the simulations. Different approaches on how the variation of the state of mixing and particle shape can be realized exist (*e.g.*, Ehrlich *et al.*, 2008b; Wendisch *et al.*, 2007). The state of mixing of a mixed-phase cloud can be defined either by the ice volume fraction $f_I = IWP/(IWP + LWP)$ or the ice optical

fraction $f_I^* = \tau_I / (\tau_I + \tau_W)$. Both approaches follow different objectives and have different consequences as explained below.

*Variation of f_I and f_I^**

The ice volume fraction f_I can be changed by scaling the concentration of the water and ice modes such that $TWP = LWP + IWP$ is kept constant. This approach has its origins in the calculation of cloud optical properties from *in situ* measurements of cloud microphysical properties. Bulk probes measure TWP with higher accuracy than its components LWP and IWP (Korolev *et al.*, 1998; Korolev and Strapp, 2002). Therefore, with regard to mixed-phase clouds the uncertainty of the calculated cloud optical properties results from the estimated f_I . Furthermore, for investigations on the cloud thermodynamics this approach is more suitable. If a cloud has a certain amount of nucleated water (TWP) this can be transformed by heterogeneous ice nucleation processes into ice crystals and change the cloud optical properties. While IWP , LWP and f_I changes, TWP remains constant.

A different approach is to keep the cloud optical thickness unchanged. Therefore, the ice optical fraction f_I^* had been varied by fitting the ice and liquid water modes of the NSD to appropriate values of τ_I and τ_W with the restriction $\tau = \tau_I + \tau_W = \text{const}$. This assumption is related to radiative transfer theory where the vertical coordinate is the clouds optical thickness. Therefore, it is more suitable to compare different clouds of the same optical thickness. All resulting effects on the cloud forcing can be concluded directly from the scattering and absorption properties of the ice and liquid water particles. This approach also suits remote sensing applications where the measured signal originates from one cloud of fixed optical thickness which otherwise may contain different amounts of ice.

The main reason for the complexity of mixing the ice and liquid water mode by f_I or f_I^* results from the different particle sizes with ice crystals being usually larger than liquid water droplets. Thus for a pure ice and pure liquid water cloud of a particular TWP less ice crystals than liquid water droplets are required to obtain the same TWP . Consequently, the lower particle concentration of the pure ice cloud results in a lower cloud optical thickness $\tau \sim TWP / D_{\text{eff}}$ (Slingo, 1990) compared to the pure water cloud. With regard to mixed-phase clouds this implies that for a fixed TWP τ decreases with increasing f_I while τ_I increases at the same time.

The dependence of τ and τ_I on the ice volume fraction f_I is plotted in Figure 5.5a for $TWP = 100 \text{ g m}^{-2}$ being fixed. The relations are displayed for different $D_{\text{eff}}^I = 30/90/150 \mu\text{m}$. The effective diameter of the liquid water droplets was fixed to $D_{\text{eff}}^W = 15 \mu\text{m}$. The plot shows that the reduction of τ is linear and larger for ice crystals of large diameter. For $D_{\text{eff}}^I = 150 \mu\text{m}$ the total optical thickness drops from 21.5 for a pure liquid water cloud to 2 for a pure ice cloud of same TWP . That means, due to heterogeneous ice nucleation the cloud optical thickness decreases if no liquid water condensates and no precipitation occurs.

With regard to the second approach f_I^* , equal τ *e.g.* measured by remote sensing methods

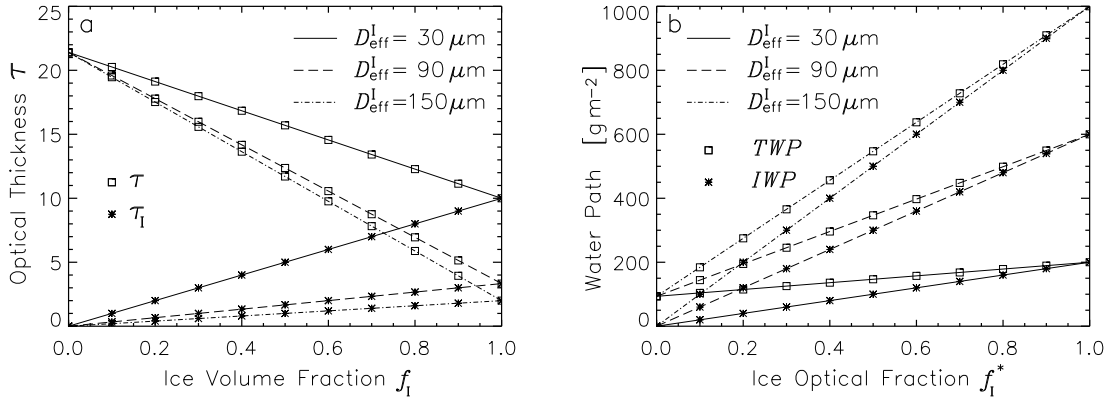


Figure 5.5: a) Impact of ice volume fraction f_I on τ and τ_I if cloud total water path is fixed $TWC = \text{const.}$ The relation is plotted for different $D_{\text{eff}}^I = 30/90/150 \mu\text{m}$. The effective diameter of the liquid water droplets was fixed to $D_{\text{eff}}^W = 15 \mu\text{m}$. In b) the appropriate dependance between ice optical fraction f_I^* and IWC respectively TWC is given for fixed τ .

can result from clouds with different TWP . The increase of TWP with increasing f_I^* is shown in Figure 5.5b for a cloud of fixed τ . The plot reveals that a pure ice cloud requires a much higher water path than a pure liquid water cloud to maintain the total cloud optical thickness. Similar to Figure 5.5b the strongest increase of TWP is obtained for the largest ice crystals $D_{\text{eff}}^I = 150 \mu\text{m}$. Here TWP increases from 90 g m^{-2} to 1000 g m^{-2} with increasing f_I^* .

The plots in Figure 5.5a and b imply that f_I and f_I^* are coupled in a nonlinear way. If TWP is kept constant an increasing f_I will always cause a simultaneous reduction of τ_W and τ . Consequently f_I^* increases but with different factor compared to f_I . The determining factor for the relation between f_I and f_I^* is the ratio between ice crystal and liquid water droplet particle size $D_{\text{eff}}^I, D_{\text{eff}}^W$.

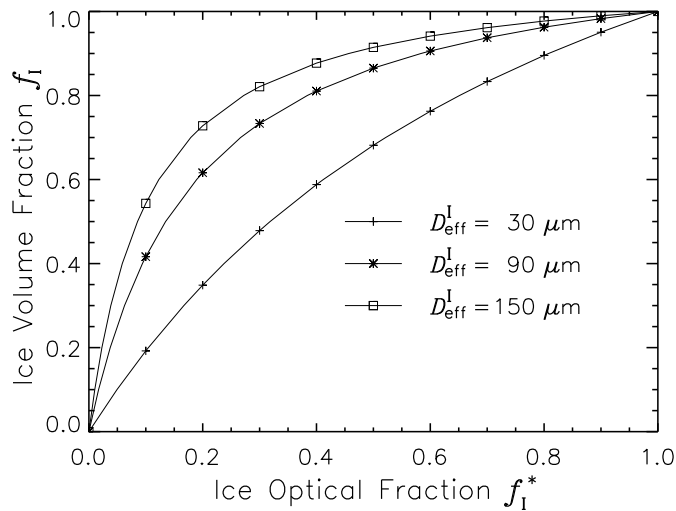


Figure 5.6: Relation between f_I and f_I^* for different $D_{\text{eff}}^I = 30/90/150 \mu\text{m}$. The effective diameter of the liquid water droplets was fixed to $D_{\text{eff}}^W = 15 \mu\text{m}$.

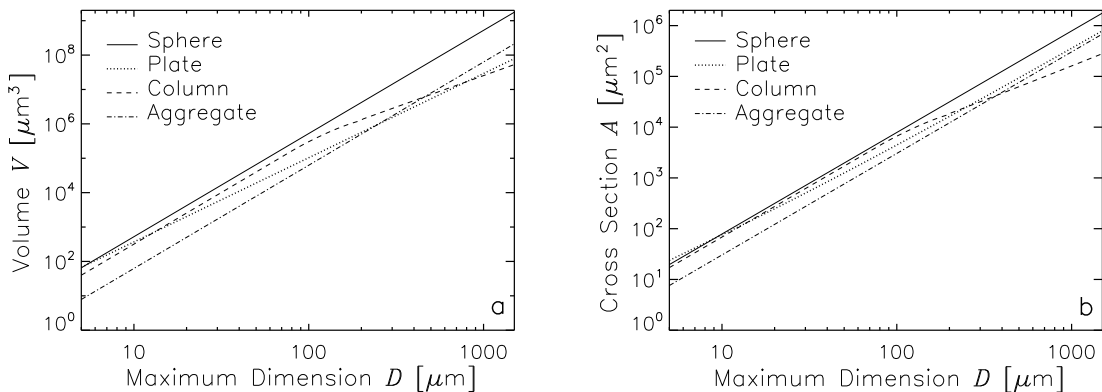


Figure 5.7: Particle volume V (a) and cross section A (b) in dependence of maximum particle dimension for different ice crystal shapes (Data is taken from PY-database).

In Figure 5.6 the relation between f_I and f_I^* is plotted for fixed $D_{\text{eff}}^W = 15 \mu\text{m}$ and varying $D_{\text{eff}}^I = 30/90/150 \mu\text{m}$. The plots show that the closer D_{eff}^I to D_{eff}^W the more linear is the relation between f_I and f_I^* . Otherwise, f_I changes more rapidly for small f_I^* . This reveals that already a low ice optical fraction *e.g.* $f_I^* = 0.2$ can account for a reasonable volumetric ice fraction of $f_I = 0.5$. This is underlined by the *in situ* measurements presented in Section 4.3.1. Here an ice fraction of $f_I^* = 0.06$ and $f_I = 0.33$ with $D_{\text{eff}}^W = 15 \mu\text{m}$ and $D_{\text{eff}}^I = 85 \mu\text{m}$ was obtained.

Variation of Ice Crystal Shape

In the same way the variation of ice crystal shape is influenced by the different cross section and volume of different ice crystal habits. While spheres have the maximum volume and maximum geometric cross section for a given particle maximum dimension $V_S(D) = \pi/6 \cdot D^3$, $A_S(D) = \pi/4 \cdot D^2$, nonspherical ice crystals have always a smaller volume $V(D) \leq V_S(D)$ and a smaller geometric cross section $A(D) \leq A_S(D)$. In this consideration the particle diameter of nonspherical ice crystals is determined by the maximum dimension of the ice crystals as registered by the CPI measurements.

The relation between D and V , A for exemplary crystal shapes taken from the PY-database is shown in Figure 5.7. It has to be pointed out, that these depend on the assumptions made in the PY-database on the aspect ratio of the crystals. Nevertheless, the plots reveal that for small particle dimension $D \leq 400 \mu\text{m}$ column shaped ice crystals and plates have volumes closer to V_S than aggregates. While for large particles aggregates have the highest particle volume of all nonspherical crystal shapes. The same is obtained for the particle cross section with plates and columns having a cross section close to A_S for small particle diameters. Aggregates have much lower cross sections than A_S , but exhibit the largest A of all nonspherical ice crystals for large particle diameters.

Similar to the two approaches f_I and f_I^* used to vary the state of mixing in mixed-phase clouds two different approaches keeping τ or TWP fixed were applied to change the ice crystal shape. For $\tau = \text{const}$ replacing spherical ice crystals with nonspherical ice

crystals will increase TWP . If TWP is kept constant replacing spherical ice crystals with nonspherical ice crystals will decrease τ .

A third approach based on *in situ* measurements of ice crystal NSD is applied (Ehrlich *et al.*, 2008b). Usually the NSD or N_{tot} is measured without quantitative information about the ice crystal shape of individual particles. Therefore, calculating cloud optical properties from the measurements requires an assumption on the particle shape (*e.g.*, Wyser, 1999; Zhang *et al.*, 1999; Wendisch *et al.*, 2005). In this third approach the NSD and N_{tot} is fixed while the ice crystal shape is varied. Consequently both τ_1 and IWP changes with ice crystal shape. Replacing spherical ice crystals with nonspherical ice crystals will decrease τ_1 and f_1^* due to the reduction of particle cross section and simultaneously decrease IWP , f_1 due to the reduction of particle volume.

In this work all simulations will be performed with the approaches to retain τ or TWP unchanged. Simulations using fixed particle number concentrations (NSD) are published by Ehrlich *et al.* (2008b) who investigated the effect of different ice crystal shape on the radiative properties of mixed-phase clouds. It was found that the cloud layer reflectance changes less than 0.04 if the ice crystal shape was varied by this approach. Therefore, the approach keeping the NSD fixed is omitted in the following investigations.

5.5 Cloud Radiative Forcing

The cloud radiative forcing at an altitude z is defined as the difference between the net irradiance obtained when a cloud is present and the net irradiance simulated for clear sky conditions.

$$\mathcal{F}_{\Delta}(z) = [F^{\downarrow}(z) - F^{\uparrow}(z)]_{\text{cloud}} - [F^{\downarrow}(z) - F^{\uparrow}(z)]_{\text{clear}} \quad (5.7)$$

Positive values correspond to a radiation gain (mostly resulting in a warming), negative values to an energy loss (cooling) of the atmosphere/Earth below the altitude z . To analyze the results the total radiative forcing $\mathcal{F}_{\Delta}(z)$ is divided into the radiative forcing of the solar $\mathcal{F}_{\Delta}^{\text{sol}}(z)$ and the IR wavelength range $\mathcal{F}_{\Delta}^{\text{IR}}(z)$. The cloud solar and infrared radiative forcing was calculated for the mixed-phase clouds introduced above using the approach f_1 and f_1^* . For varying f_1 the total water path was fixed to $TWP = 100 \text{ g m}^{-2}$, while for varying f_1^* the cloud optical thickness was set to $\tau = 20$.

5.5.1 Solar Radiative Forcing

The solar radiative forcing $\mathcal{F}_{\Delta}^{\text{sol}}$ at the surface ($z = 0$) below the cloud layer and at the top of the atmosphere ($z = \text{TOA}$) is shown in Figure 5.8a in dependence of f_1 for clouds of various $D_{\text{eff}}^{\text{I}}$. Generally, due to the reflection of radiation by the cloud layer the solar radiation reaching the surface is reduced and the amount of radiation escaping at the TOA increases. Therefore, $\mathcal{F}_{\Delta}^{\text{sol}}$ is negative at the surface and the TOA which corresponds to a cooling of the surface/atmosphere (solar cooling). The values of $\mathcal{F}_{\Delta}^{\text{sol}}$ range between -240 W m^{-2} and -110 W m^{-2} at the surface and between -220 W m^{-2} and

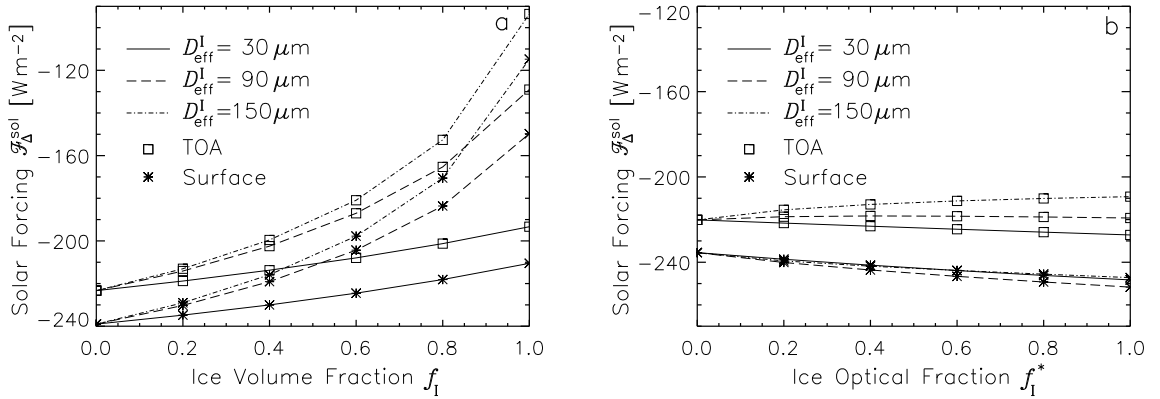


Figure 5.8: Solar radiative forcing $\mathcal{F}_{\Delta}^{\text{sol}}$ of mixed-phase clouds calculated for the top of the atmosphere (TOA) and the surface. The state of mixing was varied using a) f_{I} with $TWP = 100 \text{ g m}^{-2}$ and b) f_{I}^* with $\tau = 20$. The results are given for three different ice crystal effective diameter $D_{\text{eff}}^{\text{I}} = 30/90/150 \mu\text{m}$.

-90 W m^{-2} at the TOA. For the pure liquid water cloud the maximal solar cooling was obtained with -240 W m^{-2} at the surface and -220 W m^{-2} at the TOA. For all three ice crystal effective diameters the solar cooling of the cloud decreases (increase of $\mathcal{F}_{\Delta}^{\text{sol}}$) with increasing ice volume fraction f_{I} . This is mainly caused by the varying cloud optical thickness τ which decreases with increasing f_{I} as discussed in Section 5.4. The lower the cloud optical thickness the less solar radiation is reflected by the cloud layer and the lower is the solar cooling due to the cloud. These results imply that the phase transition of liquid water droplets to ice crystals reduces the solar cooling by the cloud if the TWP is kept constant.

In the same way the growth of ice crystals to larger diameters reduces the solar cooling by the cloud essentially. As shown in Figure 5.5 the ice crystal effective diameter influences the dependence of τ on f_{I} . Consequently, also the solar radiative forcing of the cloud is affected by $D_{\text{eff}}^{\text{I}}$ as revealed by the three curves representing different ice crystals sizes in Figure 5.8a. The decrease of the solar cooling (increase of $\mathcal{F}_{\Delta}^{\text{sol}}$) with increasing f_{I} is more significant if large ice crystals are present. The solar radiative forcing of the pure ice clouds range between -210 W m^{-2} and -115 W m^{-2} for the different $D_{\text{eff}}^{\text{I}}$ used in the simulations.

If the cloud optical thickness is kept constant the variation of the cloud solar radiative forcing with ice optical fraction f_{I}^* is reduced. At the surface the solar cooling by the clouds slightly increases with increasing f_{I}^* from -235 W m^{-2} to -250 W m^{-2} . As the cloud optical thickness is unchanged the differences result from either the single scattering albedo or the scattering phase function of the cloud particles. For the solar zenith angle used in the simulations ($\theta_0 = 71^\circ$) the sideward scattering of the scattering phase function ($\vartheta = 109^\circ$) characterizes the reflection of solar radiation for all single scattering processes. As shown in Figure 3.4 ice crystals lead to higher sideward scattering than liquid water droplets. Therefore, an increasing f_{I}^* results in a higher reflection of direct solar radiation at the cloud top and consequently in an increased solar cooling by the cloud.

At the TOA $\mathcal{F}_{\Delta}^{\text{sol}}$ ranges between -230 W m^2 and -210 W m^2 and shows a different behavior for the three $D_{\text{eff}}^{\text{I}}$ used in the simulations. For small ice crystals $D_{\text{eff}}^{\text{I}} = 30 \mu\text{m}$ the solar cooling increases about 10 W m^2 with increasing f_{I}^* while the simulations using large ice crystals $D_{\text{eff}}^{\text{I}} = 150 \mu\text{m}$ show an decrease of the solar cooling by the cloud of 10 W m^2 . This pattern is caused by the absorption of solar radiation within the cloud layer which is equivalent to the difference between the solar radiative forcing at the TOA and the solar radiative forcing at the surface (hereafter labeled with S).

The total irradiance absorbed within the atmosphere obtained for the simulations with cloud $F_{\text{A,cloud}}$ and the total absorbed irradiance for clear sky conditions $F_{\text{A,clear}}$ are calculated using Eq. 3.15 by,

$$F_{\text{A,cloud}} = [F^{\downarrow}(\text{TOA}) - F^{\uparrow}(\text{TOA})]_{\text{cloud}} - [F^{\downarrow}(\text{S}) - F^{\uparrow}(\text{S})]_{\text{cloud}}, \quad (5.8a)$$

$$F_{\text{A,clear}} = [F^{\downarrow}(\text{TOA}) - F^{\uparrow}(\text{TOA})]_{\text{clear}} - [F^{\downarrow}(\text{S}) - F^{\uparrow}(\text{S})]_{\text{clear}}. \quad (5.8b)$$

The difference between simulations with and without cloud gives the amount of radiation $F_{\text{A,CL}}$ absorbed in the cloud layer (hereafter labeled with CL),

$$F_{\text{A,CL}} = F_{\text{A,cloud}} - F_{\text{A,clear}}. \quad (5.9)$$

Inserting Eqs. 5.8a and 5.8b and using the definition of the radiative forcing given in Eq. 5.7, $F_{\text{A,CL}}$ can be calculated by the difference of the solar radiative forcing at the TOA and the surface,

$$F_{\text{A,CL}} = \mathcal{F}_{\Delta}(\text{TOA}) - \mathcal{F}_{\Delta}(\text{S}). \quad (5.10)$$

Accordingly the absorbed solar irradiance $F_{\text{A,CL}}$ can be read from Figure 5.8b as the difference of the corresponding plots of $\mathcal{F}_{\Delta}(\text{TOA})$ and $\mathcal{F}_{\Delta}(\text{S})$. Figure 5.8b shows that the absorption depends on the particle effective diameter and ranges between 15 W m^2 and 40 W m^2 . As discussed in Section 3.3 larger particles have a lower single scattering albedo and absorb more solar radiation.

The minimum values of $F_{\text{A,CL}}$ are obtained for the pure liquid water cloud; the maximum values for the pure ice cloud with maximum ice crystal effective diameter $D_{\text{eff}}^{\text{I}} = 150 \mu\text{m}$. For a small difference of the particle size between liquid water droplet and ice crystal effective diameter, the simulations using $D_{\text{eff}}^{\text{I}} = 30 \mu\text{m}$ obtain a cloud absorption almost constant with ice optical fraction f_{I}^* . Therefore, the pattern of the radiative forcing at the TOA $\mathcal{F}_{\Delta}(\text{TOA})$ shows a slight decrease equal to the increase of solar cooling at the surface caused by the enhanced sideward scattering of the ice crystals. If the ice particles are larger and consequently the cloud absorption is higher, the sideward scattering effect is compensated ($D_{\text{eff}}^{\text{I}} = 90 \mu\text{m}$) or exceeded ($D_{\text{eff}}^{\text{I}} = 150 \mu\text{m}$).

For the simulations with fixed TWP the cloud absorption is almost constant at about 15 W m^2 . The effect of different $D_{\text{eff}}^{\text{I}}$ on the cloud optical thickness balances the increase of absorption with increasing $D_{\text{eff}}^{\text{I}}$.

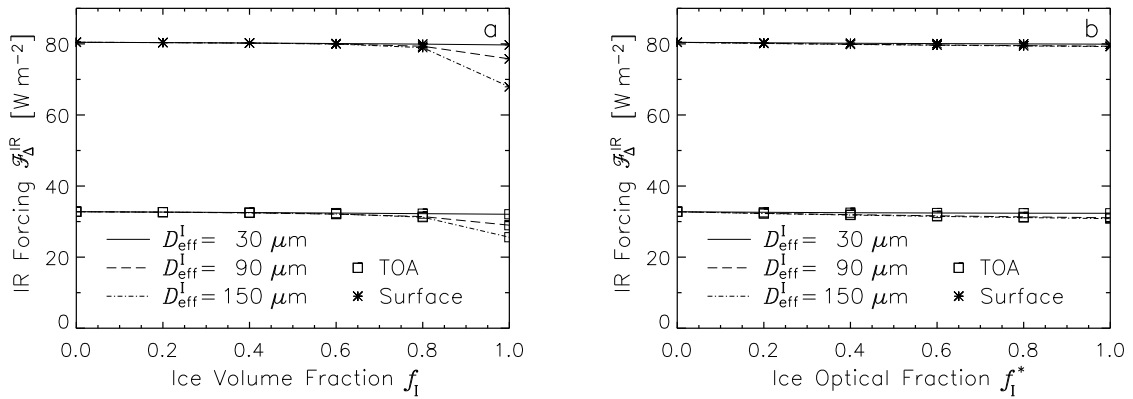


Figure 5.9: IR radiative forcing $\mathcal{F}_{\Delta}^{\text{IR}}$ of mixed-phase clouds calculated for the top of the atmosphere (TOA) and the surface. The state of mixing was varied using a) f_{I} with $TWP = 100 \text{ g m}^{-2}$ and b) f_{I}^* with $\tau = 20$. The results are given for three different ice crystal effective diameter $D_{\text{eff}}^{\text{I}} = 30/90/150 \text{ }\mu\text{m}$.

5.5.2 IR and Total Radiative Forcing

The radiative transfer simulations in the IR wavelength range have shown that the IR forcing of the clouds is almost independent of the cloud properties (τ , $D_{\text{eff}}^{\text{I}}$, f_{I} , f_{I}^*) as illustrated in Figure 5.9. The clouds absorb and emit the IR radiation as a back body. Therefore, the IR forcing of the clouds is mainly characterized by the cloud temperature which was -17°C at the cloud bottom and -20°C at the cloud top in the simulations. As the temperature in the cloud layer is generally higher than the average temperature of the atmosphere above, the clouds lead to a warming of the surface (IR warming). The whole atmosphere is also warmed by the clouds due to the lower emission of IR radiation into the space which is reduced by the lower temperature of the cloud layer compared to the surface temperature of -15°C .

In the radiative transfer simulations an IR warming of 81 W m^{-2} was obtained at the surface. For the TOA the IR warming is reduced to 33 W m^{-2} due to the slightly lower temperature at cloud top compared to cloud bottom and due to gaseous absorption in the atmosphere above the cloud top where temperatures decrease with altitude.

The only deviation from these characteristics is obtained for the pure ice clouds constructed with constant TWP and with large ice crystals ($D_{\text{eff}}^{\text{I}} = 90\text{--}150 \text{ }\mu\text{m}$). For clouds with $f_{\text{I}} = 1.0$ the optical thickness decreases below 5 for which the IR radiation is not absorbed completely by the clouds. In these cases the IR warming is reduced by 10 W m^{-2} at the surface and 5 W m^{-2} at the TOA.

Generally, the warming effect of the cloud IR forcing is lower than the cooling effect of the cloud solar forcing. Therefore, the total radiative forcing off all clouds investigated here is negative corresponding to a cooling of the Earth's atmosphere. As the IR forcing of the clouds is almost unaffected by the cloud optical properties, the pattern of the total cloud radiative forcing results mainly from the solar radiative forcing with a constant offset given by the IR forcing. Minimum values of the total radiative forcing at the surface are

obtained for the pure liquid water clouds with -160 W m^{-2} and maximum values for pure ice clouds ($f_{\text{I}} = 1.0$, $D_{\text{eff}}^{\text{I}} = 150 \mu\text{m}$) with -45 W m^{-2} .

The strong cooling effect calculated for the ABM clouds presented here differs from investigations presented in literature (*e.g.*, Schweiger and Key, 1994; Curry *et al.*, 1996; Minnett, 1999; Intrieri *et al.*, 2002; Dong and Mace, 2003; Shupe and Intrieri, 2004). For the Arctic ocean area Schweiger and Key (1994) derived a monthly averaged energy budget. For April they found a cloud solar radiative forcing of $\mathcal{F}_{\Delta}^{\text{sol}} = -34 \text{ W m}^{-2}$ and IR forcing of $\mathcal{F}_{\Delta}^{\text{IR}} = 59 \text{ W m}^{-2}$ at the surface. The total forcing amounts to $\mathcal{F}_{\Delta} = 25 \text{ W m}^{-2}$ corresponding to warming of the surface. Similar values for stratus clouds were calculated by Dong and Mace (2003) from ground based measurements near Barrow, Alaska ($\mathcal{F}_{\Delta}^{\text{sol}} = -28 \text{ W m}^{-2}$, $\mathcal{F}_{\Delta}^{\text{IR}} = 40 \text{ W m}^{-2}$, $\mathcal{F}_{\Delta} = 12 \text{ W m}^{-2}$). These results significantly differ from the surface cooling (up to -160 W m^{-2}) dominated by a strong solar radiative forcing (up to -250 W m^{-2}) obtained for the clouds presented in this work.

Both studies showed that the cloud solar radiative forcing strongly depends on the surface albedo and the solar zenith angle. In this regard the situation investigated in this work is an extreme case with a low surface albedo and a high position of the Sun. The measurements presented by Dong and Mace (2003) have been obtained above a snow covered surface ($\rho = 0.9$), while Schweiger and Key (1994) integrated their data for the Arctic ocean partly covered with sea ice. A high surface albedo strongly increases the reflected radiation in cloud free conditions compared to the dark ocean. Thus the cloud solar radiative cooling calculated in these studies is reduced compared to clouds above open sea presented here.

Furthermore, the monthly average reduces the cloud solar radiative forcing as it includes periods with darkness. In these cases the warming effect of the clouds by IR radiative forcing dominates the total cloud energy budget.

5.6 Impact of Ice Crystals Shape on Cloud Optical Properties

The impact of the ice crystal shape on the broadband cloud layer optical properties (reflectance, transmittance and absorptance) of ABM clouds was quantified. The broadband solar radiative transfer simulations were based on one-year cloud measurements with radar and microwave radiometer performed by Shupe *et al.* (2005, 2006) These data revealed microphysical properties of ABM clouds similar to the measurements obtained during ASTAR 2007 presented in Section 4.3.1. The detailed description of the study is published by Ehrlich *et al.* (2008b). In the following the major results contributing to the investigation of this work will be presented.

The radiative transfer simulations have been performed for mixed-phase clouds of different ice volume fractions f_{I} keeping the total water path fixed at $TWP = 103 \text{ g m}^{-2}$. The ice crystal shape is varied between columns, plates, bullet rosettes and aggregates keeping the ice water path IWP , f_{I} and the mean particle diameter D_{m}^{I} unchanged. Therefore, the variation of the ice crystal shape results only in a variation of $N_{\text{tot}}^{\text{I}}$ keeping the shape of the NSD unchanged. The corresponding D_{eff} of the NSD vary with ice crystal shape

Table 5.2: Mean and effective particle diameter D_m^I , D_{eff}^I of the ice crystal NSD assuming different ice crystal shapes. For the liquid water droplet NSD D_m^W , D_{eff}^W is given.

D_m^W	D_{eff}^W	D_m^I		
		Sphere	Column	Aggregate
13.3	14.3	27.0	81.0	81.0
		93.0	279.0	192.0
				58.0
				262.0

and are given in Table 5.2.

As a reference, simulations assuming spherical ice crystals are used. The calculated cloud layer reflectance \mathcal{R} , transmittance \mathcal{T} and absorptance \mathcal{A} assuming a solar zenith angle of 60° are plotted in Figure 5.10 as a function of f_I .

Only the results for columns, aggregates and spheres are shown because the cloud optical properties obtained for aggregates show the largest and for columns the smallest deviation to spherical ice crystals. The results for plates and bullet rosettes range between these two extreme cases.

In Figure 5.10a and 5.10c the results are shown for simulations assuming large ice crystals with a mean diameter of $D_m^I = 93 \mu\text{m}$ and liquid water droplets of $D_m^W = 13.3 \mu\text{m}$. For the simulations shown in Figure 5.10b and 5.10d the ice crystal mean diameter was reduced to $D_m^I = 27 \mu\text{m}$. In general, \mathcal{R} decreases and \mathcal{T} increases with increasing ice volume fraction f_I while \mathcal{A} remains almost unchanged at 0.06. This is consistent with

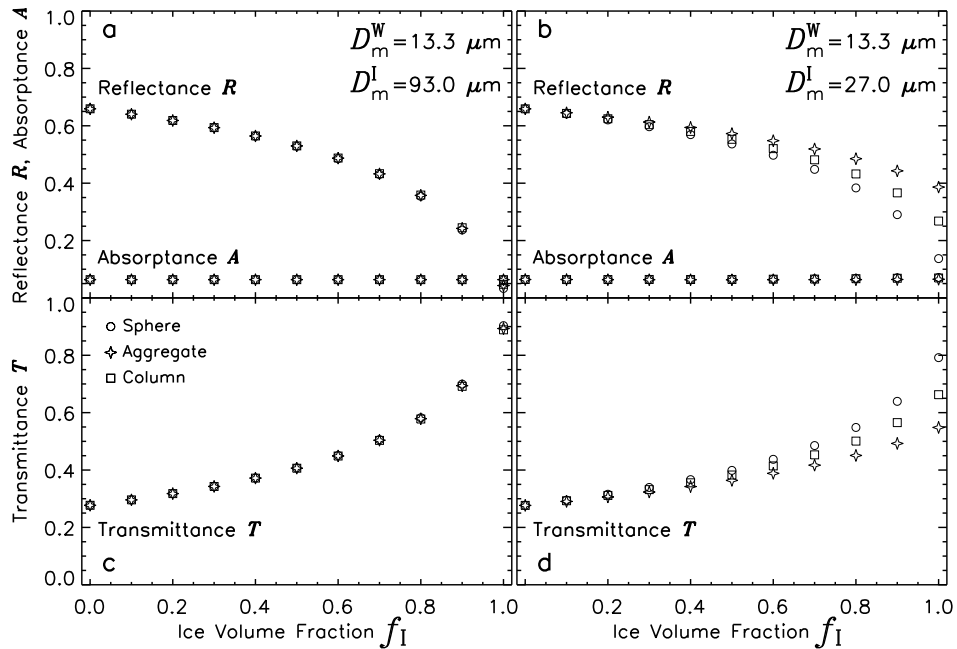


Figure 5.10: Comparison of the calculated broadband cloud layer reflectance, transmittance and absorptance for mixed-phase clouds of (a) $D_m^W = 13.3 \mu\text{m}/D_m^I = 93 \mu\text{m}$; (b) $D_m^W = 13.3 \mu\text{m}/D_m^I = 27 \mu\text{m}$. The results are given for the ice crystal shapes sphere, column and aggregate.

the decrease of the solar cooling of mixed-phase clouds with increasing f_I as discussed in Section 5.5.

There is no significant impact of the ice crystal shape on the cloud optical properties for the mixed-phase cloud with large ice crystals $D_m^I = 93 \mu\text{m}$ (Figure 5.10a and 5.10c). In this case the water mode determines the cloud radiative properties due to the high difference in the ice and water particle number concentration which is caused by the large difference in the particle diameters of ice crystals and liquid water droplets. Also for the pure ice cloud ($f_I = 1.0$) the low ice optical thickness yields no significant shape effect. However, for the case assuming smaller ice crystals $D_m^I = 27 \mu\text{m}$ the ice crystals become more relevant for the cloud radiative properties (Figure 5.5b and 5.5d). Here \mathcal{R} and \mathcal{T} calculated for the different ice crystal shapes start to diverge for ice volume fractions $f_I \geq 0.5$. For $f_I = 0.9$ the cloud reflectance ranges from 0.29 to 0.44 and transmittance from 0.55 to 0.79. The cloud absorptance does not exhibit some dependence on the assumed ice crystal shape over the entire range of f_I .

As shown by the comparison of the two simulated cases ($D_m^I = 27 \mu\text{m}$ and $D_m^I = 93 \mu\text{m}$) the mean particle dimension of the ice crystals defines the magnitude of the impact of ice crystal shapes on the cloud optical properties. The ratio between the mean ice crystal and liquid water droplet diameter mainly controls the fractional ice optical thickness and therefore the radiative impact of the ice crystal shape.

The different magnitudes of the simulated effects for columns and aggregates are caused by the consideration of the particle volumes when IWP is kept constant as discussed in Section 5.4. An increase of f_I is related to an decrease of τ . As the particle volume of columns is closer to the particle volume of spheres with the same maximum diameter than the particle volume of aggregates, the cloud optical properties assuming columns are closer to the results obtained with spherical ice crystals than the simulations using aggregates.

5.7 Spectral Cloud Top Reflectance

Considering a mixed-phase cloud with fixed cloud optical thickness the simulations presented in Section 5.5 have shown, that the variation of the cloud solar radiative forcing is not larger than 15 W m^{-2} if the ice optical fraction f_I^* is changed. That means the broadband solar irradiance has only a slight sensitivity with regard to f_I^* . However, for the remote sensing of cloud properties the spectral information of the reflected solar radiation is used utilizing the spectral cloud top reflectance R . In Figure 5.11 R for nadir viewing geometry and the cloud albedo ρ is plotted for different ice optical fractions f_I^* . The data is obtained from simulations identical to the solar radiative forcing calculations ($\tau = 20$, $D_{\text{eff}}^W = 15 \mu\text{m}$, $D_{\text{eff}}^I = 90 \mu\text{m}$).

For different f_I^* the spectral reflectance shows a variability of up to 40% which is higher than the variability of the cloud solar radiative forcing (7%, *cf.* Figure 5.8). Two different mechanisms cause the wavelength dependent variation of R . In the wavelength range between 300 nm and 1300 nm R increases with increasing f_I^* . In this wavelength range

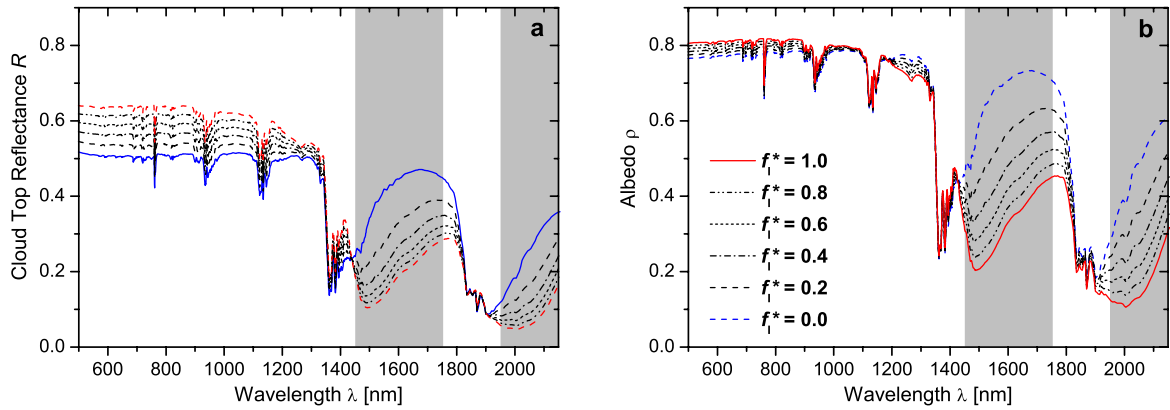


Figure 5.11: Cloud top reflectance R (a) and albedo ρ (b) simulated for clouds of various f_I^* ($\tau = 20$, $D_{\text{eff}}^W = 15 \mu\text{m}$, $D_{\text{eff}}^I = 90 \mu\text{m}$). The wavelength ranges with enhanced liquid water and ice absorption are highlighted gray.

scattering processes characterized by the scattering phase function define the radiative transfer while the absorption of solar radiation by cloud particles is weak. As shown by Figure 3.4 the scattering phase function has higher values for ice crystals than for liquid water droplets at the scattering angles being of interest here ($\vartheta = 109^\circ$). Consequently the solar radiation reflected at cloud top into nadir direction is enhanced if f_I^* increases. With regard to remote sensing applications which utilize R at VIS wavelengths to retrieve the cloud optical thickness this infers that a cloud of similar optical thickness can cause different values of R depending on their thermodynamic phase. This implies serious uncertainties for the remote sensing of cloud properties from R as described by Lee *et al.* (2006). They found that dependent on the assumed cloud thermodynamic phase the same cloud can be interpreted as pure ice cloud with $\tau = 10$ or liquid water cloud with $\tau = 16$. To avoid this ambiguity, a phase discrimination has to be conducted before common cloud retrieval algorithms are applied.

The cloud albedo ρ is less affected by the different scattering phase functions of the cloud particles. F^\uparrow used to calculate ρ integrates the radiation reflected by the cloud top over the lower hemisphere. Therefore, the information on the scattering phase function is lost. Figure 5.11b shows that ρ does not vary with increasing f_I^* for wavelengths up to 1400 nm.

Information on the cloud thermodynamic phase is given in the wavelength range of R and ρ where ice and liquid water absorption is enhanced. These wavelengths ranging between 1450–1800 nm and 1900–2150 nm are highlighted gray in Figure 5.11. The plot shows that in this wavelength range, contrary to the shorter wavelengths, R and ρ decrease with increasing ice optical fraction f_I^* . This is caused by the enhanced absorption of the ice crystals ($D_{\text{eff}}^I = 90 \mu\text{m}$) which are larger than the liquid water droplets ($D_{\text{eff}}^W = 15 \mu\text{m}$) used in these simulations and consequently have a lower single scattering albedo (higher absorption) as discussed in Section 3.3. For higher f_I^* the absorption maximum of the ice crystals is clearly identified at $\lambda = 1500 \text{ nm}$ and $\lambda = 2000 \text{ nm}$ where R and ρ have local minima.

6 Remote Sensing of Cloud Thermodynamic Phase

The spectral cloud top reflectance varies for clouds with different ice fraction. The characteristics of the reflectance spectra were utilized in three different approaches to retrieve the cloud thermodynamic phase (pure liquid, mixed-phase and pure ice cloud) from the SMART-Albedometer measurements. A known two-wavelengths approach (Section 6.1) and a principle component analysis (Section 6.2) was applied. A third approach used the combined albedo and reflectance measurements to obtain information on the cloud phase (Section 6.3). Parts of these investigations have been published in Ehrlich *et al.* (2008a). To evaluate the sensitivity of the cloud phase retrieval radiative transfer simulations have been performed for pre-defined pure ice and pure liquid water boundary-layer clouds of various optical thickness τ and effective diameter D_{eff} listed in Table 6.1. The simulations are based on the cloud presented in Section 5.3 using the same general input for the radiative transfer model as described in Section 5.1. For liquid water clouds the effective diameter was varied corresponding to the range reported by Miles *et al.* (2000) for marine stratocumulus clouds. The ice clouds are modeled for the range of effective diameter observed during ASTAR 2007. Corresponding the flight altitude of the POLAR 2 during the remote sensing of the investigated clouds the spectral cloud top reflectance and albedo are simulated for 1800 m altitude.

6.1 Spectral Slope Ice Index I_S

The spectral slope of the cloud top reflectance between 1640 nm and 1700 nm wavelength was used to identify the cloud phase with the Airborne Visible and Infrared Imaging Spectrometer (AVIRIS) by Knap *et al.* (2002). The dimensionless ice index, defined as

$$I_S^{\text{Knap}} = \frac{R_{1700} - R_{1640}}{R_{1640}} \cdot 100, \quad (6.1)$$

vanishes for pure liquid water clouds and reaches values of up to 30 for pure ice clouds. For SCIAMACHY Acarreta *et al.* (2004) have increased the wavelength range used to determine the spectral slope to 1550–1670 nm. The spectral slope is calculated by linear regression excluding the absorption bands of CO₂ (1560–1580 nm and 1595–1610 nm). Ice indices calculated this way range between 10 for liquid water clouds and 50 for ice clouds. The wavelength range used by Acarreta *et al.* (2004) was limited to 1670 nm due to technical characteristics of SCIAMACHY with a change of the spectral resolution at 1670 nm. For our measurements with the SMART-Albedometer the definition of ice index

Table 6.1: Cloud optical thickness τ and effective particle diameter $D_{\text{eff}}^{\text{W}}$, $D_{\text{eff}}^{\text{I}}$ used in the radiative transfer simulations.

τ	$D_{\text{eff}}^{\text{W}}$ [μm]	$D_{\text{eff}}^{\text{I}}$ [μm]
2/ 4/ 6/ 8/10	8/10/14/20/26	30/60/90/120/150
12/14/16/18/20		

Table 6.2: Ice indices I_S , I_P and I_A calculated for the observed clouds presented in Section 4.3.3.

	Liquid Water	Mixed-Phase	Ice
I_S	8.8	29.8	57.0
I_P	0.1	2.3	5.0
I_A	*	1.16	1.36

I_S is extended to the wavelength range between $\lambda_a = 1550$ nm and $\lambda_b = 1700$ nm,

$$I_S = \frac{100}{R_{1640}} \cdot \left[\frac{dR}{d\lambda} \right]_{[\lambda_a, \lambda_b]} \quad (6.2)$$

This is the maximum wavelength range where water vapor absorption does not contribute significantly to the measured signal. To reduce the impact of noise from the individual wavelength channels the slope of R was calculated by linear regression.

The ice indices I_S calculated from the three cloud cases presented in Section 4.3.3 are given in Table 6.2. The values range from 8.8 for the liquid water cloud to 57 for the ice cloud with the mixed-phase cloud in between. These significant differences in I_S confirm that the three observed clouds (pure ice, pure liquid water and mixed-phase) can be distinguished with this method. I_S calculated from the simulated ice and liquid water clouds is shown in Figure 6.1. Typical values for liquid water clouds range between $I_S = 5$ and $I_S = 15$. Ice clouds show a higher variability of I_S with values of up to 80.

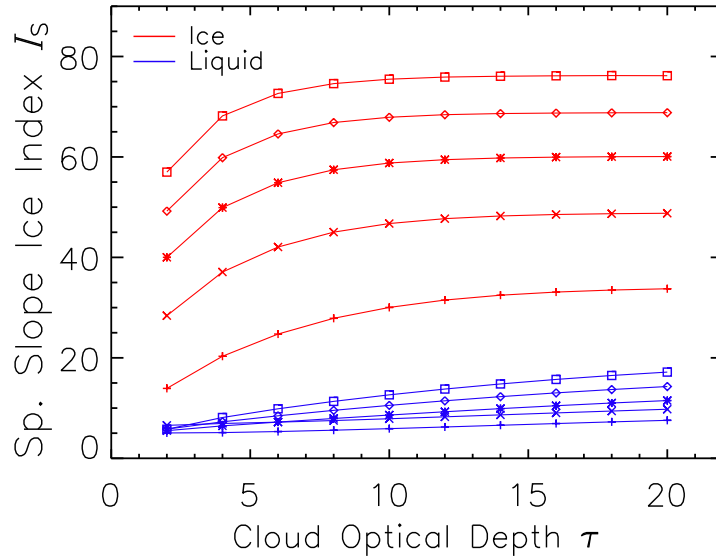


Figure 6.1: Spectral slope ice index I_S calculated from simulations of pure ice clouds (red) and pure liquid water clouds (blue). The different D_{eff} are marked by different symbols, plus ($D_{\text{eff}} = 30/8 \mu\text{m}$), cross ($D_{\text{eff}} = 60/12 \mu\text{m}$), star ($D_{\text{eff}} = 90/16 \mu\text{m}$), diamond ($D_{\text{eff}} = 120/20 \mu\text{m}$), square ($D_{\text{eff}} = 150/26 \mu\text{m}$).

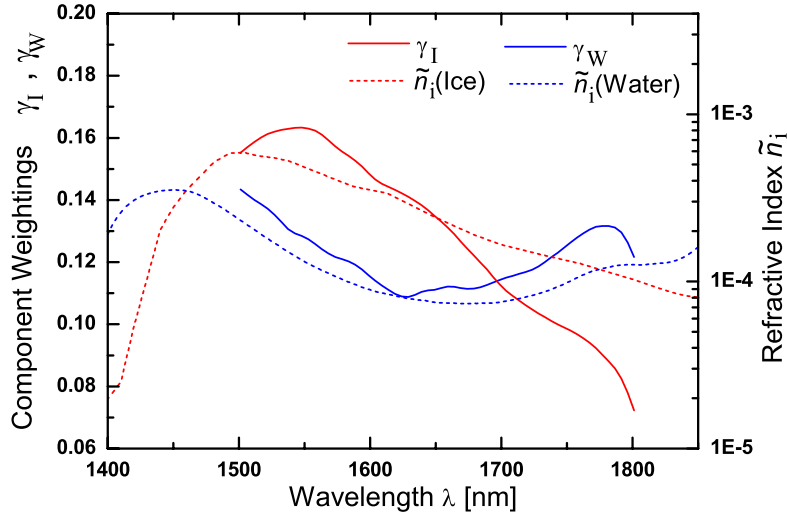


Figure 6.2: Component weightings γ_I and γ_W for the calculation of the principle components PC_I and PC_W (solid lines). Dashed lines represent the imaginary part \tilde{n}_i of refractive index for ice and liquid water published by Warren and Brandt (2008) and Wieliczka *et al.* (1989).

6.2 Principle Component Analysis (PCA) Ice Index I_P

Principle component analysis (PCA) provides a powerful tool to understand the variations in a multivariate data set (Pearson, 1901). The transformation of the original data into a set of principle components compresses the information given by the multivariate data to a few principle components. Analyzing spectral atmospheric radiation measurements the principle components are correlated with physical processes like molecular scattering, trace gas absorption or aerosol interaction (Rabbette and Pilewskie, 2001). In this work PCA was utilized to extract the ice and liquid water absorption signature in measurements and simulations of the spectral cloud top reflectance.

PCA was applied separately to the pure ice and pure liquid water boundary-layer clouds introduced above. For each phase a set of 50 different clouds was taken into account for the PCA (*cf.* Table 6.1). The simulated cloud top reflectance was normalized by the reflectance at 860 nm wavelength R_{860} to eliminate the impact of cloud optical thickness. To focus on the ice and liquid water absorption signature only, the wavelength range between $\lambda_1 = 1500$ nm and $\lambda_2 = 1800$ nm was considered for the calculations.

The PCA was performed with an Interactive Data Language (IDL) procedure *pca.pro* developed by Freedman and Landsman (1993). It performs PCA according to the method described by Murtagh and Heck (1987) and provides the component weightings $\gamma_i(\lambda)$ of the principle components PC_i . Finally, PC_i are calculated by applying $\gamma_i(\lambda)$ to the spectral cloud top reflectance,

$$PC_i = \sum_{\lambda=\lambda_1}^{\lambda_2} \gamma_i(\lambda) \cdot \frac{R(\lambda)}{R_{860}} \quad i = 1 \dots N, \quad (6.3)$$

with i defining the order of the principle component and N the number of wavelength channels used in the analysis.

Due to the normalization by R_{860} the remaining variance of the data will mainly result from changes in the absorption of the particles which are due to the variation of their effective diameter. Consequently the calculations show that the first principle component derived from the pure liquid water cloud simulations is related to liquid water absorption (hereafter called PC_W). The contribution of R at individual wavelengths to PC_W is given by the component weightings γ_W shown in Figure 6.2. The minimum weight occurs in the wavelengths between 1600 nm and 1700 nm where liquid water absorption is weak as indicated by the imaginary part \tilde{n}_i of the refractive index (dashed line).

In the same way the first principle component from the pure ice cloud simulations (hereafter called PC_I) is correlated with ice absorption and has the maximum component weighting γ_I at wavelengths around 1550 nm. In order to utilize PC_W and PC_I for cloud phase identification, a so called PCA ice index I_P is defined as,

$$I_P = \left(\frac{PC_I}{PC_W} - 0.94 \right) \cdot 100. \quad (6.4)$$

The offset of 0.94 has been determined arbitrarily in order to obtain values close to zero for liquid water clouds. For the observed liquid water cloud presented in Section 4.3.3, $I_P = 0.1$ was calculated.

Values for all three observed clouds are given in Table 6.2. The results of the analysis of the simulated liquid water clouds shown in Figure 6.3 reveal typical values of $I_P = 0-1$. For ice clouds I_P ranges from values of 1 up to 8 clearly capable of being distinguished from liquid water clouds. Therefore, I_P is a useful criterium to distinguish ice and liquid water clouds.

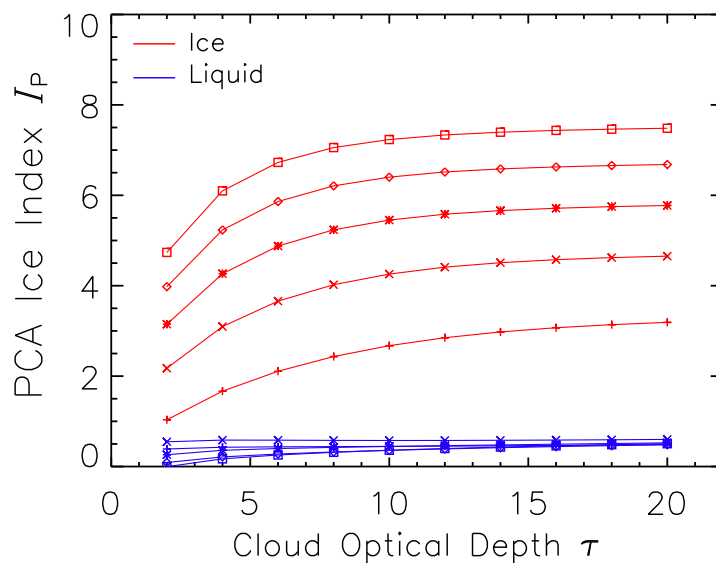


Figure 6.3: Same as Figure 6.1 for the PCA ice index I_P .

6.3 Anisotropy Ice Index I_A

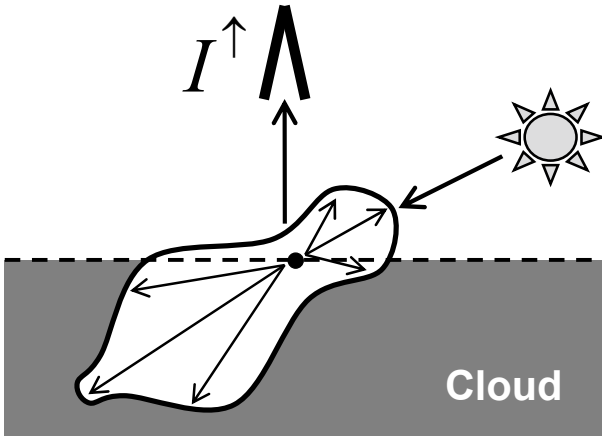


Figure 6.4: Illustration of single scattering processes at cloud top. The white area indicates the scattering phase function of liquid water droplets.

In general clouds act as non-lambertian reflectors as illustrated in Figure 6.4. The radiance field reflected from cloud top is essentially affected by the anisotropic scattering phase function of the cloud particles. Representative scattering phase functions for spherical liquid water particles and ice crystals of column, plate and aggregate shape are illustrated in Figure 6.5.

This information was used by Chepfer *et al.* (2002) to retrieve the ice crystal shape from dual satellite measurements at a wavelength of 650 nm. From the differences in the radiation scattered close to the backscatter angle of 180° and those scattered into viewing angles between 60° and 150° particle phase and shape can be distinguished.

A similar retrieval of particle phase and shape was applied by McFarlane *et al.* (2005) to measurements of the Multiangle Imaging Spectroradiometer (MISR) using the nine different viewing angles of the instrument. By minimizing the differences between measured and simulated reflectances they were able to calculate an ice index. It was shown that the highest differences between droplets and crystals occur at scattering angles between 70° and 130° . Both studies emphasize that the retrieved properties are representative only for particles near cloud top.

The configuration of the SMART-Albedometer operating under conditions of low Sun allows for a similar retrieval of the cloud phase using simultaneous albedo and nadir re-

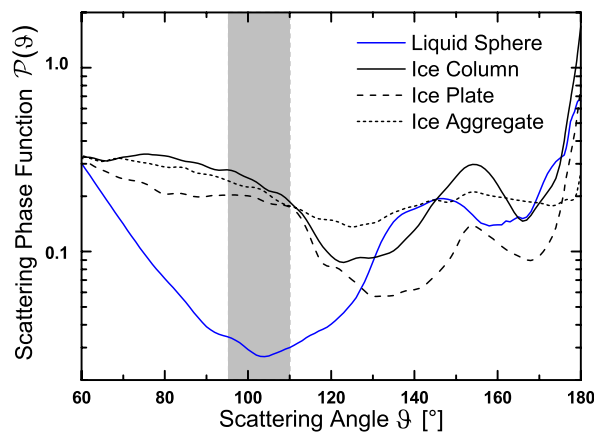


Figure 6.5: Scattering phase function of different individual cloud particles at 640 nm wavelength. The diameter of the liquid water sphere is $16 \mu\text{m}$. All ice crystals have a maximum dimension of $55 \mu\text{m}$.

flectance measurements. With the high solar zenith angles (70° to 85°) during ASTAR 2007, the nadir reflectance measurements correspond to sideward scattering by the cloud particles with scattering angles of 95° to 110° assuming single scattering as being predominant. As indicated by the grey area in Figure 6.5 these scattering angles provide substantially enhanced scattering by nonspherical particles compared to spherical particles.

This increases the upwelling radiance and cloud top reflectance which is confirmed by simulations for $\theta_0 = 71^\circ$ presented in Figure 5.11. The pure ice cloud shows higher R at wavelengths up to 1300 nm than the simulations for the pure liquid water cloud. On the other hand, the upwelling irradiance and consequently the albedo ρ (*cf.* Eq. 3.12) includes information from all scattering angles and is less dependent on the scattering phase function. This was illustrated in Figure 4.21 by comparison of R and ρ measured above the mixed-phase and pure ice clouds observed during flight # 5. Both clouds have been observed for $\theta_0 = 71^\circ$ and had a comparable optical thickness of 12. The measurements show, that the difference between R and ρ is smaller for the ice cloud than for the mixed-phase cloud, where liquid water was found at cloud top.

Based on these findings, the ratio of cloud top reflectance and albedo β_I at 645 nm wavelength is suggested as an indicator of the anisotropy of the radiation field reflected at cloud top,

$$\beta_I = \frac{R_{645}}{\rho_{645}}. \quad (6.5)$$

For the geometry presented here with $\theta_0 = 71^\circ$, β_I is always lower than 1 whereby nonspherical particles give a higher β_I than spherical particles. $\beta_I = 1$ would mean that the radiation is reflected isotropically, *i.e.*, $\rho = R$.

With increasing cloud optical thickness both ρ and R increase with a stronger increase for R . Increased multiple scattering diminishes the information of the scattering phase function and leads to more isotropically reflected radiation. That is why also β_I increases with cloud optical thickness. This relation is plotted in Figure 6.6 using R_{645} as a measure of cloud optical thickness on the abscissa. The data result from the simulations of pure liquid water clouds and pure ice clouds presented above. Both liquid water and ice clouds show a distinct relation between β_I and R_{645} , with the isotropy of the reflected radiation being significantly higher above ice clouds than above liquid water clouds of the same R_{645} . These differences are utilized to identify the cloud phase.

Therefore, β_I has been parameterized for the simulated liquid water clouds as function of R_{645} by the polynomial fit shown as a blue solid line in Figure 6.6. This parametrization is valid for the assumed geometry (θ_0 , nadir view, flight altitude) and the entire variety of liquid water clouds (τ , D_{eff}) provided by the simulation. This leads to the definition of the anisotropy ice index I_A as the deviation of the measured β_I^{meas} from the β_I^{water} parameterized for liquid water clouds. I_A is calculated as the ratio

$$I_A = \frac{\beta_I^{\text{meas}}}{\beta_I^{\text{water}}}. \quad (6.6)$$

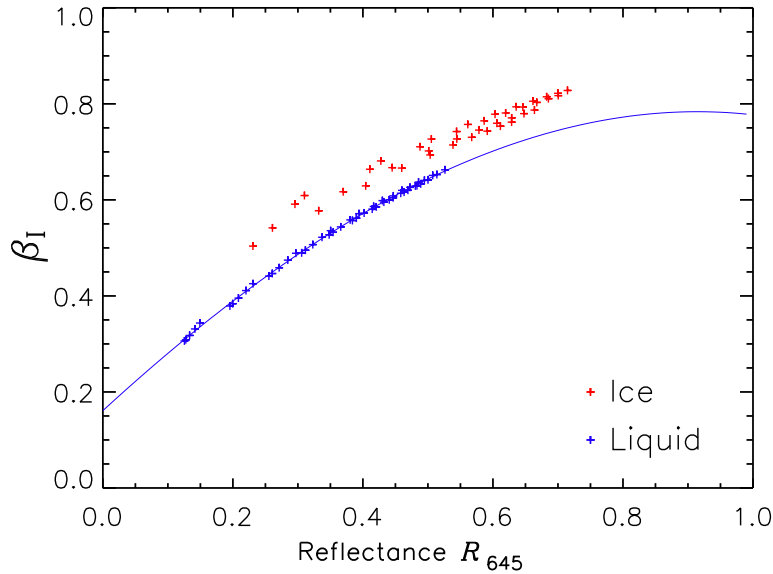


Figure 6.6: Simulated β_I for pure liquid water clouds and pure ice clouds (column-shaped crystals) of different optical thickness ($\tau = 2$ –20) and effective diameter (8 – $26 \mu\text{m}$ for liquid water and 10 – $100 \mu\text{m}$ for ice clouds). The polynomial fit for the liquid water cloud is overlaid as a solid line ($\beta_I^{\text{water}} = 0.15 + 1.32 \cdot R - 0.67 \cdot R^2 + 0.01 \cdot R^3$).

Therefore, β_I^{water} is obtained from the polynomial fit using the measured value of R_{645}^{meas} . Using R_{645}^{meas} incorporates indirectly the cloud optical thickness and reduces their impact on I_A . From the definition of I_A it follows that $I_A = 1$ for pure liquid water clouds and $I_A > 1$ for pure ice clouds.

The results for the observed pure ice cloud and mixed-phase cloud presented in Section 4.3.3 are given in Table 6.2. Both values differ significantly from unity. For the pure liquid water cloud it was not possible to calculate I_A . This cloud had a small horizontal extension. The measured albedo was substantially affected by the dark water surface visible apart the cloud.

Typical values for water clouds obtained from the simulated clouds are shown in Figure 6.7 and range between $I_A = 0.98$ and $I_A = 1.03$. Ice clouds give higher values of $I_A > 1.06$ separated distinctly from the results for liquid water clouds.

6.4 Sensitivity Studies

The cloud top reflectance is affected not only by the cloud thermodynamic phase but also by other cloud optical properties (cloud optical thickness and cloud particle effective diameter). In order to reduce their impact on the cloud phase retrieval different normalizations of R are applied before calculating the ice indices. Nevertheless, it is impossible to overcome these influences completely.

Acarreta *et al.* (2004) have shown for their ice index (which is similar to the spectral slope ice index I_S) that the values for ice clouds may vary by a factor of up to 3 between clouds of small effective diameter/low cloud optical thickness and clouds of large effective

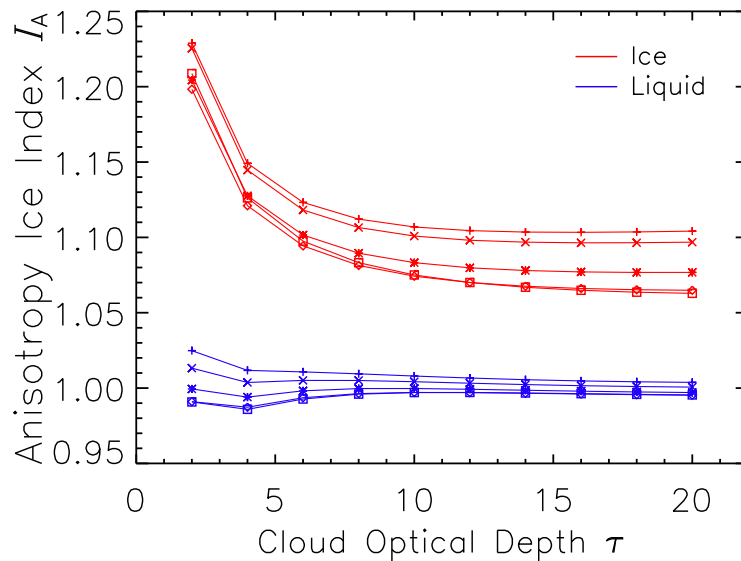


Figure 6.7: Same as Figure 6.1 for the anisotropy ice index I_A .

diameter/high cloud optical thickness. Changes in the solar zenith angle have been found to be less important for the simulated ice indices. Especially for optically thin clouds the surface properties have an impact on the ice indices. The surface albedo is crucial for the VIS wavelength used to calculate the anisotropy ice index I_A . Absorption by liquid water, snow or sea ice may affect the spectral slope ice index I_S and the PCA ice index I_P . In order to reduce the complexity this study concentrates on the conditions during ASTAR 2007 with an open sea surface.

In the following the impact of cloud optical thickness and particle effective diameter on the ambiguity to discriminate pure ice and pure liquid water clouds by the ice indices is discussed (Subsection 6.4.1). Subsection 6.4.2 presents investigations of the sensitivity of the ice indices on the vertical structure of ABM clouds.

6.4.1 Cloud Optical Properties

The ice indices I_S , I_P and I_A calculated from the simulations of pure ice and liquid water clouds of different τ and D_{eff} are shown in Figure 6.1, 6.3 and 6.7. The plots reveal that the ice indices are almost insensitive to D_{eff} and τ for pure liquid water clouds. The values vary only slightly with D_{eff} and τ . The spectral slope ice index I_S and the PCA ice index I_P show almost no variation with τ . On the other hand, the ice indices of the pure ice clouds spread over a wide range. Most significant is the decrease of I_S and I_P with decreasing D_{eff} . Especially for optically thin ice clouds I_S can reach values of pure liquid water clouds with high optical thickness. A slight improvement is given by I_P . Here none of the ice clouds give values as low as the simulated liquid water clouds. The discrimination of pure ice and pure liquid water clouds is almost unambiguous.

With regard to an identification of mixed-phase clouds *a priori* knowledge of D_{eff} and τ is

needed. The ice indices obtained for a mixed-phase cloud range between a minimum value given by a liquid water cloud and a maximum given by an ice cloud with D_{eff} and τ equal to the values of the mixed-phase cloud (not shown here). If D_{eff} , τ and accordingly the maximum values of I_S and I_P are not known, the ice indices obtained for the mixed-phase cloud may indicate a pure ice cloud with smaller D_{eff} or smaller τ .

Most robust with regard to the cloud optical properties of ice crystals is the anisotropy ice index I_A . Figure 6.7 shows that values for ice and liquid water clouds differ for all simulations. Therefore, I_A is most suitable (in theory) for discriminating ice and liquid water clouds in the setting of the present sensitivity study. It has to be pointed out that theoretically I_A is exactly 1 for the liquid water clouds as the data shown here are simulations equal to the simulations used to parameterize β_1^{water} . The deviation from 1 results from slight differences between data points of β_1^{water} and its parametrization (*cf.* Figure 6.6).

6.4.2 Vertical Distribution

Generally, the definition of a mixed-phase cloud is that ice and liquid water particles coexist in a certain cloud volume. For radiative transfer simulations there are different options to realize this mixture, either as a homogeneous mixed single-layer cloud or as a multi-layer cloud with distinct pure ice and liquid water layers. From the *in situ* measurements presented in Section 4.3.1 it follows that ABM clouds typically consist of two layers with liquid water droplets at cloud top and precipitating ice below. This sensitivity study focus on the ability to identify such mixed-phase clouds and how the layering affects the cloud phase retrieval.

Radiative transfer simulations have been performed based on the microphysical measurements (flight # 5), presented in Section 4.3.1. The cloud optical properties were fixed at $\tau = 15$, $D_{\text{eff}}^{\text{W}} = 15 \mu\text{m}$ for liquid water particles and $D_{\text{eff}}^{\text{I}} = 85 \mu\text{m}$ for ice particles. The cloud was divided into 10 sublayers with a homogeneous liquid water mode of $\tau_{\text{W}} = 1.5$ for each layer. One ice layer ($\tau_{\text{I}} = 1.5$) was added and shifted from cloud top to cloud bottom. For each simulation the ice indices I_S , I_P and I_A were calculated. The results are given in Table 6.3.

Table 6.3: I_S , I_P , and I_A of mixed-phase clouds ($\tau_{\text{W}} = 13.5$, $\tau_{\text{I}} = 1.5$) for different positions of the ice layer (not all 10 simulations are shown here). The position is given by the optical thickness $\tau_{\text{W}}^{\text{top}}$ of the liquid water layer located above the single ice layer.

$\tau_{\text{W}}^{\text{top}}$	I_S	I_P	I_A
0.0	41.0	3.3	1.08
1.5	32.2	2.4	1.01
3.0	25.7	1.8	1.00
6.0	18.4	1.2	1.00
9.0	14.6	0.8	1.00
13.5	11.8	0.5	1.00

The results show that all three indices are most sensitive to the upper cloud layer showing the highest values if the ice layer is located at cloud top ($\tau_{\text{W}}^{\text{top}} = 0$). Here $\tau_{\text{W}}^{\text{top}}$ gives the total optical thickness of the liquid water layers located above the single ice layer. The maximum values of $I_{\text{S}} = 41$, $I_{\text{P}} = 3.3$ and $I_{\text{A}} = 1.08$ range above typical values for pure liquid water clouds and below the maximum values of an ice cloud with equal $D_{\text{eff}}^{\text{I}} = 85 \mu\text{m}$ and $\tau = 15$ as used in the simulations of the mixed-phase cloud (*cf.* Figure 6.1, 6.3 and 6.7).

The spectral slope ice index I_{S} and the PCA ice index I_{P} decrease slowly with increasing $\tau_{\text{W}}^{\text{top}}$ to values of $I_{\text{S}} = 12$, $I_{\text{P}} = 0.5$ which reaches the range simulated for pure water clouds. Nevertheless, for $\tau_{\text{W}}^{\text{top}} < 10$ and considering the effective diameter of the water particles ($D_{\text{eff}}^{\text{W}} = 15 \mu\text{m}$) the ice indices I_{S} and I_{P} are higher than for pure liquid water clouds. This suggests that these approaches are able to distinguish typical ABM clouds with a liquid cloud top layer from pure liquid water clouds. It has to be pointed out that the sensitivity of I_{S} and I_{P} to mixed-phase clouds will be reduced if a smaller $D_{\text{eff}}^{\text{I}}$ of the ice crystals is assumed. Smaller ice crystals have less absorption which results in reduced differences of I_{S} and I_{P} between pure ice and liquid water clouds (*cf.* Figure 6.1 and Figure 6.3).

The anisotropy ice index I_{A} deviates from the values of pure liquid water clouds only if the ice layer is at cloud top. This suggests that I_{A} is suitable only for a discrimination of pure ice and pure liquid water clouds. Typical ABM clouds with liquid cloud top will be identified as pure liquid water clouds. This is consistent with the findings of Chepfer *et al.* (2002) who found that the particle shape retrieved from two scattering angles at 650 nm wavelength was insensitive to multilayered clouds when τ of the cloud top layer is larger than 2.

6.5 Case Study on Flight # 5

On flight # 5 (April 7, 2007) concurrent radiation and microphysical measurements have been conducted along the path of the Cloud-Aerosol Lidar and Infrared Pathfinder Satellite (CALIPSO) over the Greenland Sea as marked in Figure 4.16 (Section 4.3) with B. A stratus cloud field with cloud top up to 1500 m extended from 77.3° N to northwards at the time of the CALIPSO overpass (10:18 UTC). The profile of the total attenuated backscatter signal measured by CALIPSO is shown in Figure 6.8a. The lidar could not completely penetrate the optically thick clouds with exception of the cloud edge ($< 77.4^\circ \text{N}$). For the investigated cloud the depolarization measurements (not shown here) are not suitable for a cloud phase analysis. Multiple scattering in the optically thick clouds increased the depolarization regardless of particle shape. Nevertheless, the lidar profiles reveal that in the southern part of the cloud deck (*cf.* Figure 4.16 and left-side of Figure 6.8a) ice particles are precipitating down to the surface. These precipitation particles, which are also observed from CloudSat (reflectivity), can be detected by the Lidar because they are not capped by a liquid water layer in this area.

This part of the cloud was sampled with *in situ* microphysical instruments about 1 hour

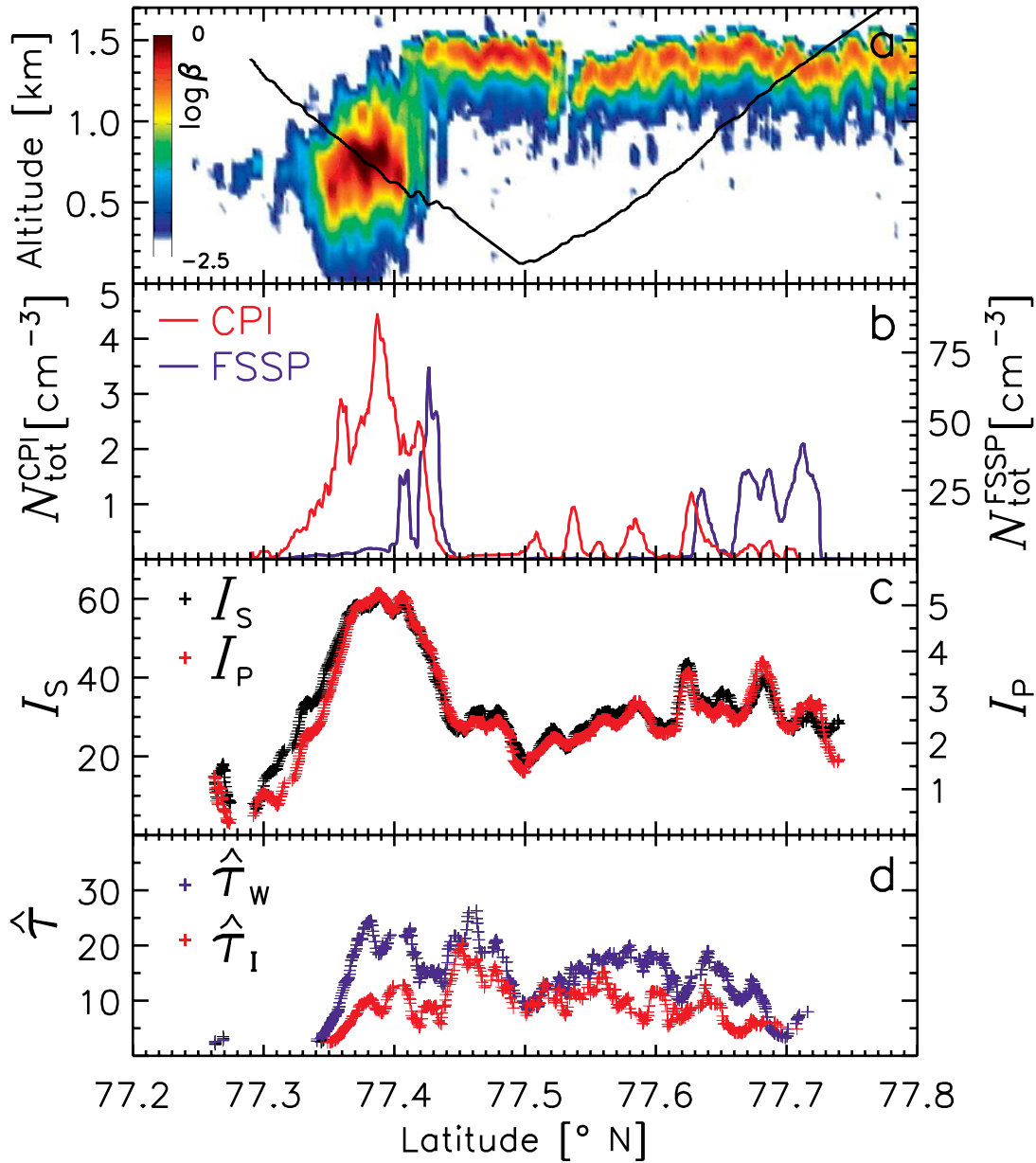


Figure 6.8: Profile of total attenuated backscatter coefficient β [$\text{sr}^{-1} \text{km}^{-1}$] measured by CALIPSO in the cloud observed on flight #5 (a). The flight track of the *in situ* measurements is overlaid as a black line. Ice and liquid water particle number concentrations N_{tot} measured by CPI and FSSP along the flight track and the ice indices I_S and I_P for the same positions are given in panel b and c. In panel d the cloud optical thickness $\hat{\tau}_W$ and $\hat{\tau}_I$ retrieved by assuming pure liquid water and pure ice clouds is shown.

before the CALIPSO overpass. The advection of the cloud field with the northerly winds is considered in Figure 6.8b with 11.5 km/h. The measurements corrected for advection showed that the cloud edge in the southern part consisted of ice particles only ($< 77.4^\circ \text{N}$). The particle number concentration measured by the CPI increases up to $N_{\text{tot}} = 3 \text{ cm}^{-3}$. First liquid water particles have been observed with the FSSP 3 km further north. After the descent below the cloud base (77.5°N to 77.6°N) the partly high ice crystal number concentrations with simultaneous absence of liquid water particles is related again to precipitating ice below the cloud. Higher cloud layers are probably of mixed-phase as measured during the ascent through the cloud (77.6°N to 77.7°N).

Shortly after the CALIPSO overpass the cloud was investigated again by radiation measurements flying above the cloud top. From the measured cloud top reflectance the cloud phase was remotely identified using the ice indices defined above. Figure 6.8c shows the measured spectral slope ice index I_S and PCA ice index I_P along the flight track of flight # 5. Both ice indices show high values around 77.4°N which correlates with the high ice particle concentration measured by the *in situ* instrumentation one hour earlier. The maximum values of $I_S = 60$ and $I_P = 5$ indicate a pure ice cloud when compared to the simulations shown in Figure 6.1. With measured values of $D_{\text{eff}} = 85 \mu\text{m}$ and $\tau = 15$, the simulations for $D_{\text{eff}} = 90 \mu\text{m}$ and $\tau = 15$ show values of I_S and I_P similar to the ice indices calculated from the measurements.

Lower values ($I_S = 20\text{--}40$ and $I_P = 2\text{--}4$) corresponding to mixed-phase clouds assuming unchanged D_{eff} and τ were measured later when the FSSP registered significant liquid water particle concentrations. With respect to the sensitivity studies of Section 6.4, I_S and I_P measured above the mixed-phase clouds are higher than expected and close to values of pure ice clouds with small effective diameter. This reveals that either the fraction of ice crystals is much higher than measured by the *in situ* measurements or the vertical distribution of the ice differs from the assumption of a liquid cloud top layer with high ice concentrations below. This issue will be discussed in Section 7 in more detail.

Additionally, the cloud optical thickness τ was derived from R by applying a common cloud retrieval algorithm as suggested by Nakajima and King (1990). τ was retrieved for two different assumptions on the cloud thermodynamic phase. The results assuming pure liquid water clouds $\hat{\tau}_W$ are given in Figure 6.8d by blue symbols; red symbols indicate the cloud optical thickness $\hat{\tau}_I$ derived from the assumption of pure ice clouds. The plot shows that $\hat{\tau}_I$ is in general lower than $\hat{\tau}_W$ what is a direct consequence of the enhanced sideward scattering of nonspherical ice crystals as discussed in Section 5.7. In comparison with the ice indices, the largest differences between $\hat{\tau}_W$ and $\hat{\tau}_I$ occur above the observed pure ice cloud where the retrieval of $\hat{\tau}_W$ overestimated the optical thickness with $\hat{\tau}_W \approx 20$ compared to $\hat{\tau}_I \approx 10$. Above the mixed-phase clouds which can be assumed as liquid water clouds in this regard as the cloud top is dominated by liquid water droplets the retrieval of $\hat{\tau}_I$ underestimates the cloud optical thickness significantly. These differences indicate that an assumption of the cloud thermodynamic phase is necessary to retrieve reliable cloud optical properties.

The analysis of the reflectance-albedo ratio β_I also reveals the presence of ice at the cloud

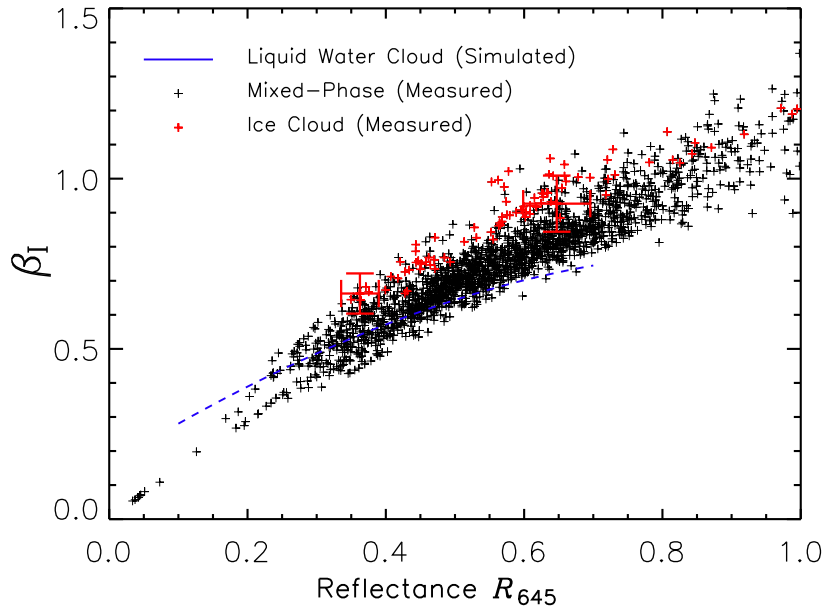


Figure 6.9: Measured β_I as function of R_{645} . Black crosses show measurements over mixed-phase clouds, red crosses over the ice cloud observed on the cloud edge. Simulations for pure liquid water clouds are shown as a blue line.

edge. Figure 6.9 shows all measurements taken on flight # 5, above clouds ($\theta_0 = 71^\circ$). Generally the measured values of β_I deviate from the theoretical curve of pure liquid water clouds (1D simulations) which is not expected for mixed-phase clouds with a thick liquid layer at cloud top (*cf.* Section 6.4.2). The high values of β_I indicate the presence of ice crystals at the top of the mixed-phase clouds.

It has to be pointed out here that due to the combination of three separate measurements (F_λ^\downarrow , F_λ^\uparrow and I_λ^\uparrow) the uncertainties of the data points are relatively large as marked at two measurements samples in Figure 6.9. Furthermore, the 1D simulations used to define the anisotropy ice index I_A do not account for possible 3D radiative effects. Nevertheless, the measurements above the cloud edge (labeled by red crosses) tend to range in higher values of β_I . This shows that at the cloud edge nonspherical ice crystals were present at cloud top.

6.6 Case Study on Flight # 9

On flight # 9 (April 9, 2007) similar the measurements on flight # 5 boundary-layer clouds have been observed. Due to the weakened supply of cold air reaching from the sea ice located in the North, the cloud field was more heterogenous than the mixed-phase clouds investigated on flight # 5. In Figure 6.10 an MODIS satellite image of the cloud field is given. The flight track of the POLAR 2 aircraft is overlaid as red line. Similar to the measurements on flight # 5 the flight pattern of the POLAR 2 was combined with an overpass of CALIPSO (dashed line).

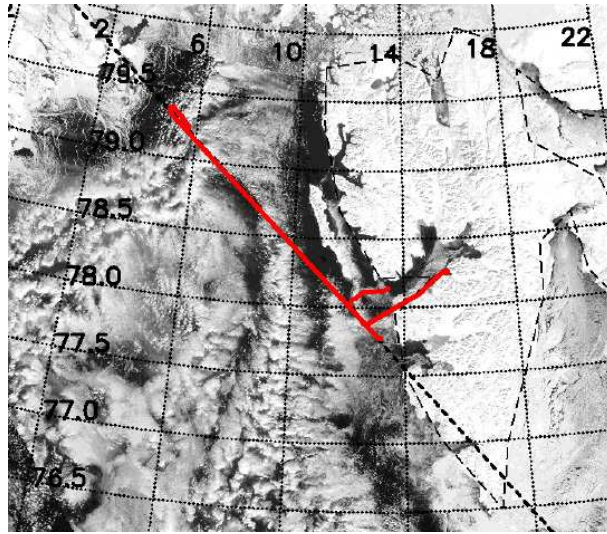


Figure 6.10: MODIS satellite image of April 9, 2007 overlaid with the flight track of POLAR 2 (flight # 9, red line) along the CALIPSO overpass (dashed black line). Numbers give the latitude and longitude respectively.

In situ measurements with the FSSP, CPI and Polar Nephelometer were conducted short before and during the CALIPSO overpass. About one hour before the satellite overpass the clouds were remotely sensed on the same track with the SMART-Aledometer and AMALi. The results of the *in situ* and remote sensing measurements between 77.9° N and 79.2° N are shown in Figure 6.11 in plots similar to Figure 6.8. In addition the depolarization measurements of AMALi are given in panel e. For each depolarization profile AMALi measurements were averaged over 15 seconds. For the comparison of all measurements the advection of the cloud field with respect to the CALIPSO overpass is considered. The *in situ* and remote sensing measurements were corrected for a northerly advection component of 7 km/h.

The backscattering profile measured by CALIPSO shows distinct cloud patches with different cloud top altitudes and cloud vertical thicknesses. The cloud top altitude tends to increase towards North what is confirmed by the AMALi measurements. Between 78.7° N and 78.9° N a larger cloud gap has been observed. The cloud top is indicated by slightly enhanced depolarization values in the AMALi signal. Multiple scattering by the liquid water droplets at the cloud top layer leads to depolarization of the polarized radiation emitted by the AMALi laser. This layer with slightly enhance depolarization shows approximately the cloud top. The identification of cloud gaps is confirmed by the retrieval of $\hat{\tau}_W$ and $\hat{\tau}_I$. Both values decrease in areas where cloud gaps are indicated by AMALi.

High depolarization ratios have been observed by AMALi between 78.5° N and 78.6° N and at about 79.0° N. The high depolarization indicate the presence of ice crystals. By scattering processes of the polarized radiation emitted by AMALi at the plane surfaces of the ice crystals the direction of polarization is changed following the Fresnel equations. This leads to a depolarization of the radiation detected by AMALi compared to the

emitted radiation. These areas with high depolarization ratio coincide with high ice indices derived from the SMART-Albedometer measurements. Therefore, these cloud parts are identified as pure ice clouds. The *in situ* instruments did probe solely the ice cloud at 79.0° N. Here, ice crystal number concentrations up to $N_{\text{tot}} = 4 \text{ cm}^{-3}$ were measured. Although the *in situ* measurements were taken at lower parts of this cloud the remote sensing measurements reveal that the ice crystals were present up to the cloud top. Similar to the ice cloud observed on flight # 5 for this ice cloud the retrieval of $\hat{\tau}_W$ overestimated the cloud optical thickness compared to $\hat{\tau}_I$.

The southern ice cloud was not completely sampled by the *in situ* measurements as the cloud top was significant lower at this location compared to the clouds observed in the surrounding area. The interruption of the cloud structure is visible at 78.5° N in the MODIS image taken at 10:00 UTC short before to the CALIPSO overpass (Figure 6.10). The lower cloud top and the ice crystals identified by the remote sensing instruments indicate that this part of the cloud mainly consists precipitating ice crystals which potentially have their origin in the surrounding clouds.

South to 78.4° N the comparison of CALIPSO, *in situ* and remote sensing measurements fails due to the long time difference between the measurements. At the location between 78.2° N and 78.4° N a large cloud gap has been observed by CALIPSO and *in situ* instruments while the AMALi and SMART-Albedometer measurements indicate mixed-phase clouds with liquid cloud top layer.

The slight differences in the ice indices observed in this area partly coincide with the retrieved cloud optical thickness. Higher $\hat{\tau}_W$ and $\hat{\tau}_I$ correlate with enhanced ice indices. This is consistent with the sensitivity study presented in Section 6.4. Therefore, the variations of the ice indices does not necessarily indicate higher ice concentrations. However, it has to be pointed out that contrarily the retrieval of $\hat{\tau}_W$ and $\hat{\tau}_I$ is affected by the cloud thermodynamic phase complicating the analysis in this regard.

This cloud scene observed on flight # 9 shows that Arctic boundary-layer clouds partly exhibit a high variability of cloud properties like cloud top altitude, thermodynamic phase and optical thickness. These heterogeneities potentially affects the 3D radiative transfer and consequently the remote sensing of cloud properties by measurements of reflected solar radiation as reported by *e.g.*, Cahalan *et al.* (1994); Rozwadowska and Cahalan (2002).

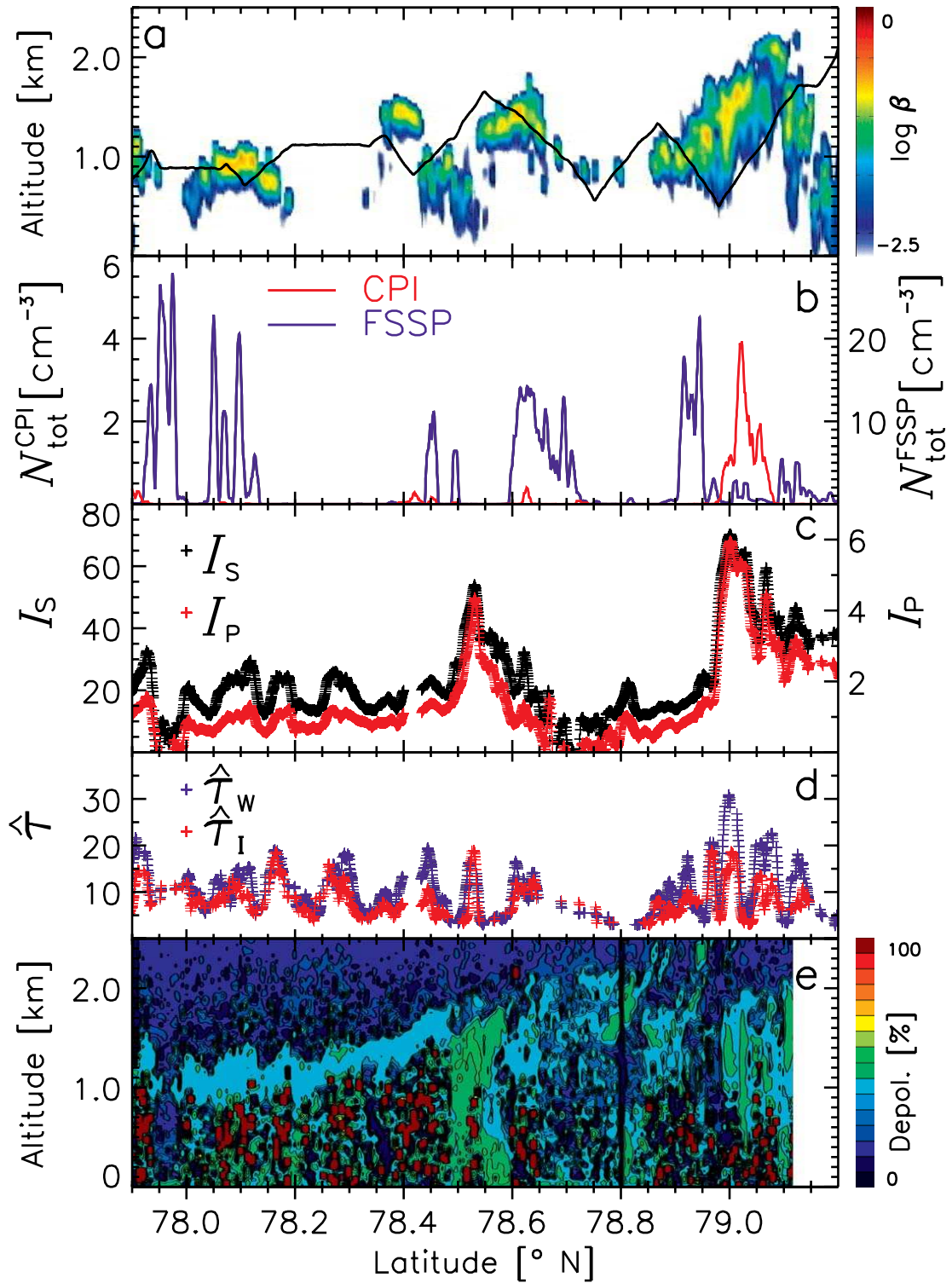


Figure 6.11: Same as Figure 6.8 for the clouds observed on flight #9. In addition the depolarization profile obtained from AMALi is given in panel e.

7 Vertical Structure of Arctic Boundary-Layer Mixed-Phase Clouds

For the ABM clouds investigated in this work the ice indices ($I_S = 29.8$ and $I_P = 2.3$) are slightly higher than expected for clouds with an optical thick liquid water layer at cloud top as shown in the sensitivity study in Section 6.4.2.

Therefore, in this section a closure study of the measured microphysical and radiative cloud properties is performed with focus on the vertical structure of ABM clouds. For this purpose the radiative transfer code and the required input described in Section 5.1 is used. In Section 7.1 and 7.2 the simulations are analyzed with regard to the cloud optical thickness and the ice optical fraction of the mixed-phase clouds.

The vertical distribution of the ice crystals within the cloud layer is retrieved from spectral differences of the cloud top reflectance. Therefore, additional radiative transfer simulations using 3D Monte Carlo radiative transfer models are applied. In Section 7.3 the vertical footprint of the measured SMART-Albedometer signal is derived from these simulations. This information is applied to modify the cloud model used in the radiative transfer simulations as described in Section 7.4. In Section 7.5 the backscatter glory observed at the cloud top of the ABM clouds is investigated in detail by 3D radiative transfer simulations.

7.1 Closure of Cloud Optical Thickness

The cloud was divided into two vertical sublayers representing the observed vertical structure of the ABM clouds. The cloud top layer (1200–1600 m) contains only liquid water droplets, whereas the cloud bottom (800–1200 m) contains both liquid water droplets and ice crystals. In Figure 7.1 the geometry of the cloud model used for the radiative transfer simulations is illustrated (left cloud). The microphysical and optical properties averaged over the *in situ* measurements taken in the sublayers are given in Table 7.1. For the liquid

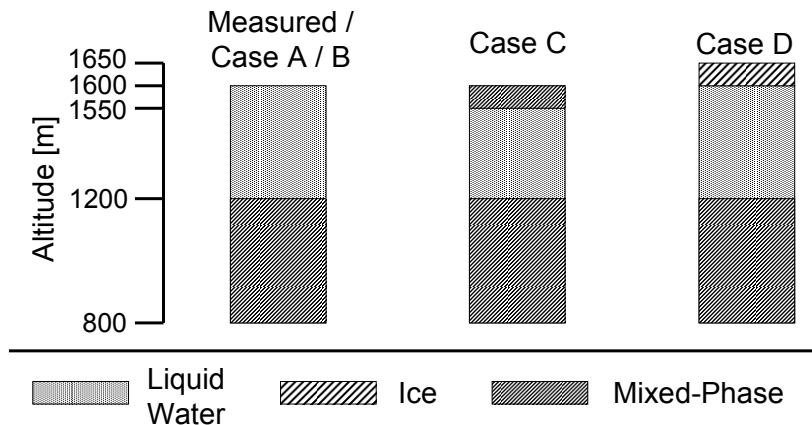


Figure 7.1: Cloud geometries as represented in the radiative transfer simulations for the cases A, B, C and D and for the simulations using the measured cloud properties.

Table 7.1: Microphysical and optical properties of the ABM cloud observed on flight # 5. For the closure study the cloud was divided into two sublayers, 800–1200 m and 1200–1600 m. The adjusted values are used in the simulations of Case A where the cloud optical thickness was scaled to the observed cloud top reflectance.

		Original	Scaled (Case A)
Liquid water 800–1600 m	τ_W	7.5	16.9
	LWP [g m ⁻²]	34.7	78.0
	D_{eff}^W [μm]	14.8	14.8
Ice 800–1200 m	τ_I	0.5	1.1
	IWP [g m ⁻²]	17.2	38.7
	D_{eff}^I [μm]	102.7	102.7
Total 800–1600 m	τ	8.0	18.0
	TWP [g m ⁻²]	51.9	116.7
	f_I^*	0.06	0.06
	f_I	0.33	0.33

water droplets the data were averaged over the entire cloud. A total optical thickness of 8 was derived from the *in situ* measurements with an ice optical fraction of 0.06. The total water path TWP amounts 51.9 g m⁻² with an ice volume fraction of 0.33.

The cloud top reflectance R simulated with the measured cloud optical properties is compared in Figure 7.2a to R measured by the SMART-Albedometer. The measurement uncertainty of R is indicated by the gray area. Especially for wavelengths shorter than 1800 nm the simulations (dashed line) range below the measured R and are outside the measurement uncertainties. This indicates that the cloud optical thickness is underestimated by the *in situ* measurements.

Beside the uncertainties of the *in situ* instruments, cloud inhomogeneities cause problems for deriving representative cloud optical properties. During the *in situ* probing several areas with low particle concentrations and low extinction coefficients b_{ext} were sampled related to the undulating structure of the clouds. By averaging the measurements over the total time when the Polar Nephelometer measured considerable amounts of cloud particles ($b_{\text{ext}} > 0.05 \text{ km}^{-1}$) the mean values of b_{ext} underestimate the total cloud optical thickness. Maximum values of $b_{\text{ext}} = 35 \text{ km}^{-1}$ and $b_{\text{ext}} = 20 \text{ km}^{-1}$ have been measured for the liquid water droplets by the FSSP and Polar Nephelometer, respectively. In the thin ice layer the extinction coefficient of the ice crystal population amounts up to $b_{\text{ext}} = 13 \text{ km}^{-1}$ as measured by the CPI. The underestimation of the cloud optical thickness due to cloud inhomogeneities can be reduced by an extended sampling time of the cloud. During ASTAR 2007 the clouds have been probed during descends and ascends of the POLAR 2 with climbing rates of 200 m min^{-1} which reduces the sampling time for the individual vertical cloud layers even more.

In order to adjust the results of the radiative transfer simulations to the measured R in the VIS wavelength range the cloud optical thickness is scaled in the following simulations. Therefore, N_{tot}^W and N_{tot}^I of the NSDs are varied. The scaling was applied by keeping

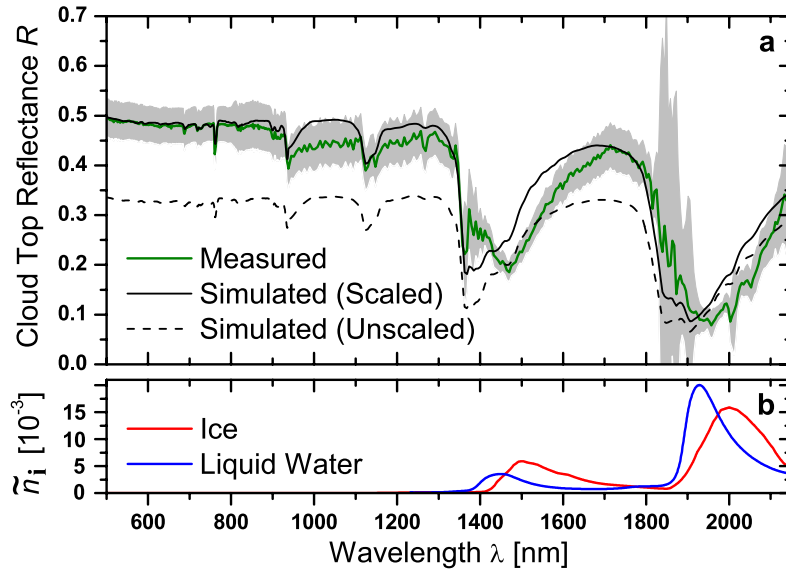


Figure 7.2: Simulated and measured spectral cloud top reflectance R (panel a). The measurement uncertainty is illustrated by the gray area. In panel b the refractive index \tilde{n}_i of liquid water (Wieliczka *et al.*, 1989) and ice (Warren and Brandt, 2008) is displayed.

cloud particle effective diameter, f_I^* and f_I unchanged. The microphysical and optical properties of the scaled cloud (hereafter referred as Case A) are given in Table 7.1. With $\tau = 18$ the scaled total cloud optical thickness is more than doubled compared to the values derived from the *in situ* measurements.

The results of the radiative transfer simulations for Case A are shown in Figure 7.2 as solid line. For wavelengths less than 1400 nm the simulated R ranges within the uncertainties of the SMART-Albedometer measurements. However, at wavelengths where ice absorption is strong, as indicated by the imaginary refractive index displayed in Figure 7.2b, the simulated R is higher than measured. This reveals that in the model cloud less ice crystals are present than indicated by the remote sensing measurements.

As shown in Section 6 the spectral slope ice index and the PC ice index obtained for the ABM cloud are $I_S = 30$ and $I_P = 2.3$, respectively. From the simulated cloud top reflectance (Case A) values of $I_S = 13.4$ and $I_P = 0.7$ were calculated. These values are in the range which is derived for pure liquid water clouds, what is not surprising as the ice optical fraction $f_I^* = 0.06$ of the simulated cloud is close to zero. Therefore, the uncertainties of the measured f_I^* deduced from the simultaneous FSSP and CPI measurements are addressed in the following Section.

7.2 Closure of Ice Optical Fraction

Based on the measured and scaled cloud optical properties of Case A the ice optical fraction f_I^* was varied between values corresponding to pure liquid water clouds ($f_I^* = 0.0$) and a pure ice cloud ($f_I^* = 1.0$). The microphysical and optical properties of the six simulated clouds referred as Case B1–B6 are given in Table 7.2. The cloud geometry and

Table 7.2: Microphysical and optical properties of ABM clouds Case B1–B6 characterized by different ice optical fractions f_1^* . The total cloud optical thickness is scaled to gain a cloud top reflectance in the VIS wavelength range similar to the observation of the ABM cloud on flight # 5.

		B1	B2	B3	B4	B5	B6
Liquid Water	τ_W	18.0	16.2	14.0	9.6	6.0	0.0
800–1600 m	LWP [g m ⁻²]	83.0	74.7	64.6	44.3	27.7	0.0
Ice	τ_I	0.0	1.8	3.5	6.4	9.0	9.0
800–1200 m	IWP [g m ⁻²]	0.0	61.4	119.3	218.2	306.9	306.9
Total	τ	18.0	18.0	17.5	16.0	15.0	9.0
800–1600 m	TWP [g m ⁻²]	83.0	136.1	183.9	262.5	334.6	306.9
	f_1^*	0.00	0.10	0.20	0.40	0.60	1.00
	f_1	0.0	0.45	0.65	0.83	0.92	1.00

Table 7.3: Spectral slope ice index I_S and PC ice index I_P for the simulations of the clouds Case B1–B6. Additionally the values obtained from the SMART-Albedometer measurements are given.

	B1	B2	B3	B4	B5	B6	Measured
I_S	11.4	14.3	16.2	20.4	26.9	56.2	29.8
I_P	0.5	0.8	1.0	1.5	2.2	5.0	2.3

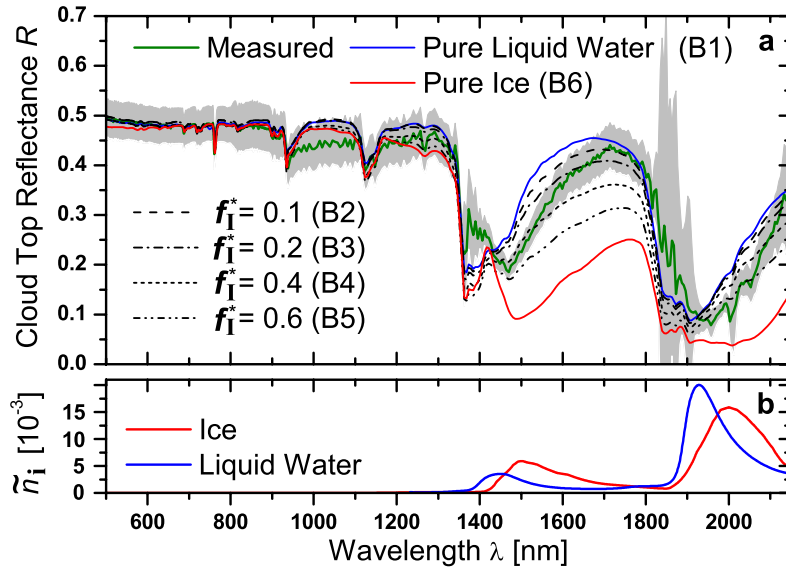


Figure 7.3: Measured spectral cloud top reflectance R and simulated R for mixed-phase clouds of different f_I^* (Case B1–B6). The measurement uncertainty is illustrated by the gray area. In panel b the refractive index \tilde{n}_i of liquid water (Wieliczka *et al.*, 1989) and ice (Warren and Brandt, 2008) is displayed.

the particle effective diameter D_{eff}^w , D_{eff}^I are identical to the cloud Case A. As shown in Section 5.7 (Figure 5.11) the cloud top reflectance increases with increasing f_I^* if the total cloud optical thickness is kept constant. In order to fit R in the VIS wavelength range to the measured values the total cloud optical thickness of Case B1–B6 was scaled for each cloud separately.

The results of the radiative transfer simulations are given in Figure 7.3a. All simulations range between the two extreme cases; the pure liquid water cloud (B1, blue line) and the pure ice cloud (B6, red line). The corresponding ice indices I_S and I_P calculated from the simulations are listed in Table 7.3. The comparison with the measured ice indices indicates that the simulated cloud Case B5 with $f_I^* = 0.6$ fits best to the measurements.

However, in Figure 7.3a the analysis of the spectral structure of R in the wavelength range dominated by ice and liquid water absorption between 1400 nm and 2150 nm reveals that none of the simulated cases matches the measurements at the entire wavelength range. For low ice optical fractions $f_I^* < 0.4$ the ice crystal concentration is too low and the resulting ice absorption too weak to reproduce the observed ice absorption minima. These minima were present in the measurements of the SMART-Albedometer at 1490 nm and 2000 nm wavelengths which agrees with the maxima in the refraction indices of ice plotted in Figure 7.3b. However, at wavelengths where ice absorption is less strong (1600–1800 nm) R is in the range of the measurement uncertainties of the measured R for $f_I^* < 0.4$. The opposite is obtained for the simulations with $f_I^* \geq 0.4$. For these cases the ice absorption is strong enough to reproduce the spectral measurements at the ice absorption minima. However, the increasing ice absorption additionally reduces the cloud top reflectance at

wavelengths between 1600 nm and 1800 nm. In this wavelength range the simulations with $f_1^* \geq 0.4$ fail to fit the measured R .

The conclusion is that there has to be another parameter which alters the spectral slope in the wavelength range dominated by ice and liquid water absorption (1400–2200 nm). From additional radiative transfer simulations using modified cloud models (not shown here) it was found that neither the particle effective diameter of the ice crystals and liquid water droplets nor the ice crystal shape are responsible for the observed spectral pattern of R . Therefore, in the following section the vertical footprint of the radiance measurement is investigated.

7.3 Vertical Footprint of Radiance Measurements

The relative contribution of individual cloud layers to the overall retrieval of cloud properties was investigated by Platnick (2000). He found for vertical inhomogeneous liquid water clouds that the vertical weighting for the cloud top reflectance measurements has a maximum at the cloud top layer of less than an optical thickness of 2. The calculated weighting functions strongly depend on the solar zenith angle and the wavelength used for the retrieval (1600 nm, 2200 nm or 3700 nm). The larger the wavelength and the solar zenith angle, the higher is the maximum of the weighting function and the closer this maximum is located to the cloud top. These spectral differences in the weighting functions at four different MODIS bands were utilized by Chang and Li (2002, 2003) and most recently by Chen *et al.* (2008) to estimate the vertical variation of the cloud droplet effective diameter from remote sensing.

These concepts are used in the following to study the vertical distribution of ice and liquid cloud particles in the observed ABM clouds. Therefore, the spectral difference of ice and liquid water absorption observed by the measurements of R is utilized. To quantify in which cloud layers the radiation is primarily absorbed the air mass factor (AMF) approach is applied. The air mass factor \hat{A} is a measure of the total path a photon undergoes until arriving at the instrument sensor as illustrated in Figure 7.4. It is defined as the ratio of the slant photon path L_S and the vertical photon path L_V measured between the top of the atmosphere and the Earth's surface and obtained for a cloud free atmosphere:

$$\hat{A} = \frac{L_S}{L_V} \quad (7.1)$$

From this definition follows that for $\hat{A} = 1$ the photon path is once the vertical extension of the Earth's atmosphere.

With regard to clouds each scattering process by cloud particles extends the photon path

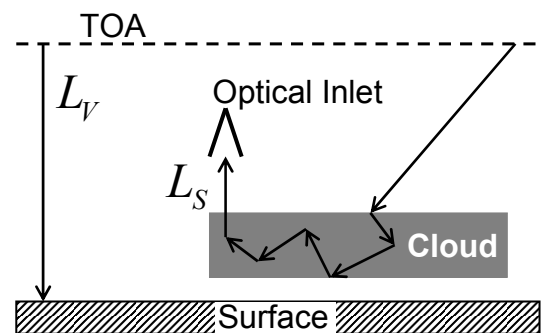


Figure 7.4: Definition of air mass factors.

and rises \hat{A} . If the scattering increases due to cloud particles the absorption of radiation increases too (*cf.* Eq. 3.18). Thus the air mass factor \hat{A} provides a measure for the absorption of radiation by cloud particles.

To quantify the contribution of distinct cloud layers to the measured absorption, box-AMFs \hat{a}_i are calculated as described by (Wagner *et al.*, 2007). For a homogeneous distribution of the cloud particles \hat{a}_i is defined by,

$$\hat{A} = \frac{1}{N} \cdot \sum_{i=1}^N \hat{a}_i \quad (7.2)$$

with i the index of distinct cloud layers considered in the calculations and N giving the total number of these layers. Assuming homogeneous cloud layers that are sufficiently thin ($N \rightarrow \infty$), the box-AMF $\hat{a}(z)$ can be defined for explicit altitudes z following,

$$\hat{A} = \frac{1}{z_{\text{top}} - z_{\text{base}}} \int_{z_{\text{base}}}^{z_{\text{top}}} \hat{a}(z) dz \quad (7.3)$$

with z_{base} and z_{top} defining the cloud base and cloud top.

The box-AMFs appropriate to the radiance measurements of the SMART-Albedometer are calculated by 3D Monte Carlo radiative transfer simulations. Therefore, the Monte Carlo radiative transfer inversion model McArtim was applied (Deutschmann, 2008). McArtim is an advanced version of the radiative transfer model TRACY-II developed by Deutschmann and Wagner (2006) and was involved in a comparison study of several radiative transfer models conducted by Wagner *et al.* (2007). For the simulations two wavelengths ($\lambda = 1510$ nm and $\lambda = 1710$ nm) where the refractive index of liquid water differs and absorption of atmospheric trace gases is weak were chosen.

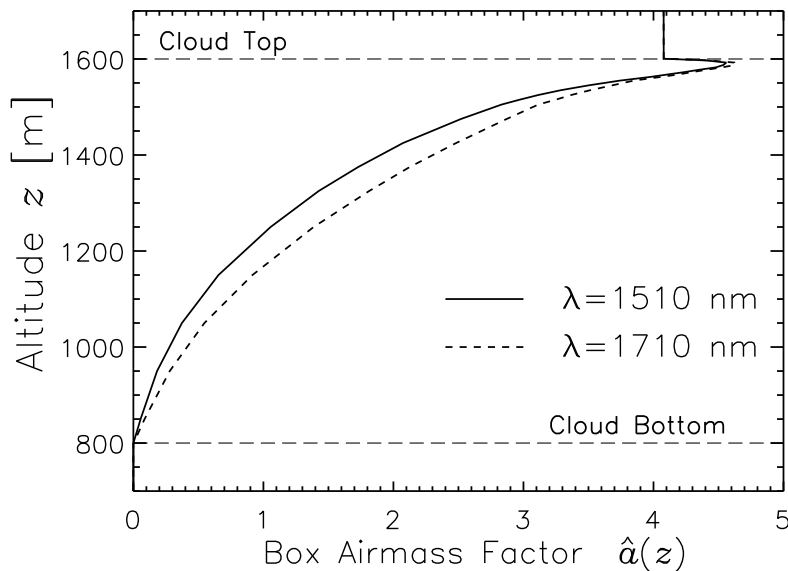


Figure 7.5: Box air mass factor $\hat{a}(z)$ simulated for Case A.

The input for the simulations was adapted from the clouds simulated above. For the SMART-Albedometer an opening angle of $\Delta = 2.1^\circ$ was used facing into nadir direction. According to the measurements presented in Section 5.1.2 the surface reflectance was set to zero. Thus no multiple reflections between the surface and the cloud layer occur in the simulations. The input for the cloud layer is identical to Case A matching the observed R at VIS wavelengths. The scattering phase functions of the ice crystals and liquid water droplets were represented by Henyey-Greenstein functions in McArtim.

The box-AMF $\hat{a}(z)$ of the simulated cloud is shown in Figure 7.5 for the two wavelengths $\lambda = 1510$ nm and $\lambda = 1710$ nm. In general $\hat{a}(z)$ is higher for $\lambda = 1710$ nm than for $\lambda = 1510$ nm. This results from the differences in the refractive indices of ice and liquid water which are both higher at $\lambda = 1510$ nm. With higher refractive index the probability that a photon is absorbed and does not reach the sensor of the instrument increases. Consequently, the path of photons that reach the sensor is shorter in average; $\hat{a}(z)$ is smaller.

The vertical profile of $\hat{a}(z)$ gives information on the contribution of each cloud layer to the absorption measured by the SMART-Albedometer. Figure 7.5 reveals that the highest $\hat{a}(z)$ are obtained close to the cloud top. Above the cloud $\hat{a} = 4.1$ was calculated. These values result from the low Sun ($\theta_0 = 71^\circ$). An estimate is the direct solar radiation reaching the surface for which the analytic relation $\hat{A} = 1/\cos\theta_0$ gives an air mass factor of 3.1. From cloud top $\hat{a}(z)$ increases within the first 10 m of the cloud to a maximum value of $\hat{a}(z) = 4.6$ for $\lambda = 1710$ nm. Below, $\hat{a}(z)$ decreases to zero at cloud bottom which is related to the surface albedo ($\rho = 0$) used in the simulations. This vertical profile implies that the information on the cloud particles retrieved from the absorption in the spectral cloud top reflectance is related to these layers. The cloud particles at lower altitudes have a weaker impact on the measurements.

To compare the results for the two wavelengths the box-AMFs were normalized by the total AMF \hat{A} (calculated with Eq. 7.3) and the geometric thickness of the cloud layer:

$$\hat{s}(z) = \frac{1}{z_{\text{top}} - z_{\text{base}}} \cdot \frac{\hat{a}(z)}{\hat{A}} \cdot 100\% \quad (7.4)$$

The resulting $\hat{s}(z)$ describes the normalized footprint in units of $\% \text{ m}^{-1}$ of the absorption measured by the SMART-Albedometer. The total AMF used for the normalization amounts to $\hat{A} = 1.24$ for $\lambda = 1510$ nm which is lower than $\hat{A} = 1.47$ obtained for $\lambda = 1710$ nm. The calculated footprints for the two wavelengths are given in Figure 7.6a. In Figure 7.6b $\hat{s}(z)$ is accumulated over the altitude starting with 0% at cloud top.

For both wavelengths the footprint shows the highest contribution for cloud layers close to the cloud top. The maximum values of $\hat{s}(z)$ are found to be higher for $\lambda = 1510$ nm than for $\lambda = 1710$ nm. With the higher values of $\hat{s}(z)$ the cloud top reflectance at $\lambda = 1510$ nm responds stronger to the size of the particles in the cloud top layer and is therefore more suitable for their retrieval than R at $\lambda = 1710$ nm.

A decrease of $\hat{s}(z)$ with increasing cloud depth is observed for both wavelengths. The accumulated footprint shows that 50% of the measured signal at 1710 nm wavelength is

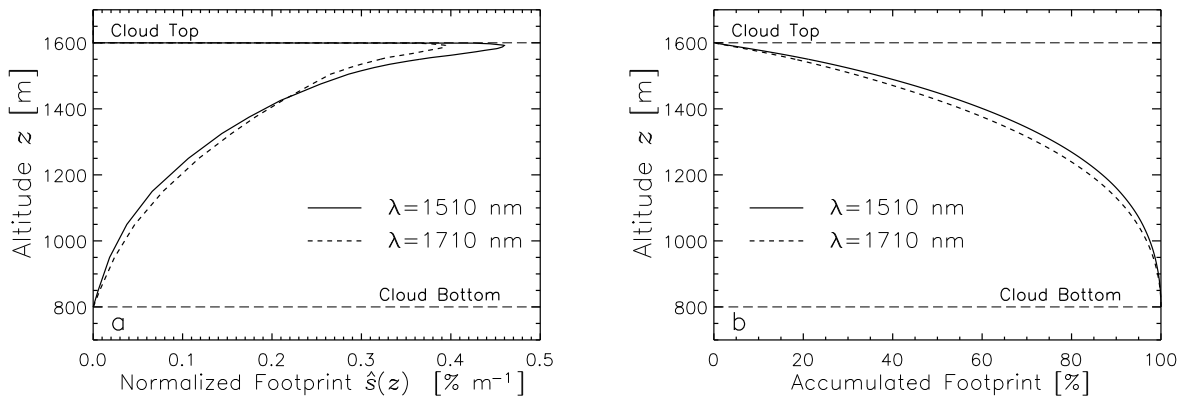


Figure 7.6: Vertical footprint $\hat{s}(z)$ for the radiance measurements of the SMART-Albedometer with respect to absorption by the cloud particles using the cloud Case A (panel a). The accumulated footprint is given in panel b.

related to the cloud layer above 1420 m. Only 10% correspond to the cloud layer below 1130 m. For $\lambda = 1510$ nm a steeper slope is obtained (50% at 1450 m). This amplifies the assumption that the observed absorption signal in the radiance measurements for $\lambda = 1490$ nm is related to layers close to the cloud top while the absorption observed at longer wavelengths about 1710 nm includes particles located at lower cloud layers.

These spectral differences in the footprint provide a tool to retrieve information on the vertical distribution of the cloud particle effective diameter, as described by Chen *et al.* (2007). Other than Chen *et al.* (2007) the investigations shown here are limited to a small wavelength range (1400–1800 nm). However, this range includes one spectral maximum and one spectral minimum of ice and liquid water absorption and is covered by the SMART-Albedometer measurements with sufficient spectral resolution to analyze these spectral differences. Wavelengths where liquid water and ice absorption are strong can be used to derive the particle properties at cloud top, whereas wavelengths with weaker absorption give information on particles located at lower cloud layers. Utilizing the spectral differences between the maxima of ice and liquid water absorption separate vertical profiles for ice crystals and liquid water droplets can be derived.

The SMART-Albedometer measurements of R presented in Figure 7.2a showed that for wavelengths below $\lambda = 1700$ nm stronger absorption is measured than shown by the simulations. The maximum differences overlap with the ice absorption maximum ($\lambda = 1490$ nm). At wavelengths between 1700–1800 nm weaker absorption is observed. Following the findings discussed above the strong absorption for $\lambda = 1490$ nm implies that large ice crystals are present in the uppermost cloud layers. On the other hand, the high values of R between 1700–1800 nm wavelength indicate small cloud particles at cloud top and at lower cloud layers. This conclusion differs from the vertical distribution of ice crystals and liquid water droplets obtained by the *in situ* measurements. This can explain the discrepancy between simulated and measured cloud top reflectance.

7.4 Ice Crystals at Cloud Top

The analysis of the vertical footprint calculated for the radiance measurements suggests that ice crystals might be present at cloud top of the ABM clouds observed on flight # 5. Therefore, the original cloud simulated with Case A was modified in Case C and D by adding a thin ice layer at cloud top. For Case C the ice layer is situated within the original cloud; for Case D an ice layer is added above the cloud top as illustrated in Figure 7.1. The optical thickness of the thin cloud layer was set to 0.5 with ice crystal effective diameter similar to the ice layer at cloud bottom ($D_{\text{eff}}^{\text{I}} = 103 \mu\text{m}$, column shape). Due to adding the ice layer, the total optical thickness of the cloud is adjusted to $\tau = 15.0$ for Case C and $\tau = 14.5$ for Case D.

The spectral cloud top reflectance R simulated for the two cases C and D is shown in Figure 7.7. For both cases almost identical results are obtained. Compared to the simulations presented above (Case A and B), the simulation fit for all wavelengths into the uncertainty range of the observed R . Especially the spectral pattern in the wavelength range dominated by ice and liquid water absorption is closer to the measurements as simulated without the additional ice layer. This reveals that ice crystals situated at cloud top are necessary to explain the observed absorption features with strong absorption at 1490 nm and weak absorption at wavelengths about 1750 nm.

From the *in situ* measurements of microphysical cloud properties no convincing evidence of ice crystals in the uppermost cloud layer above 1500 m altitude was found. In this cloud layer only 7 out of 69 measurements of the Polar Nephelometer indicated ice crystals with asymmetry parameters below 0.82 (*cf.* Figure 4.18). These measurements do not significantly alter the volumetric asymmetry parameter ($\langle g \rangle = 0.85$) calculated for this

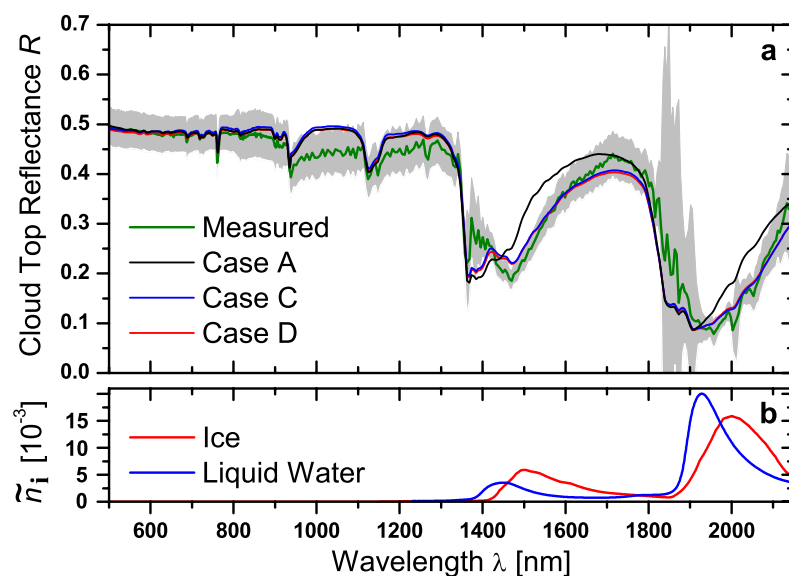


Figure 7.7: Measured and simulated spectral cloud top reflectance R for cases A, C and D (panel a). The measurement uncertainty is illustrated by the gray area. In panel b the refractive index \tilde{n}_i of liquid water (Wieliczka *et al.*, 1989) and ice (Warren and Brandt, 2008) is displayed.

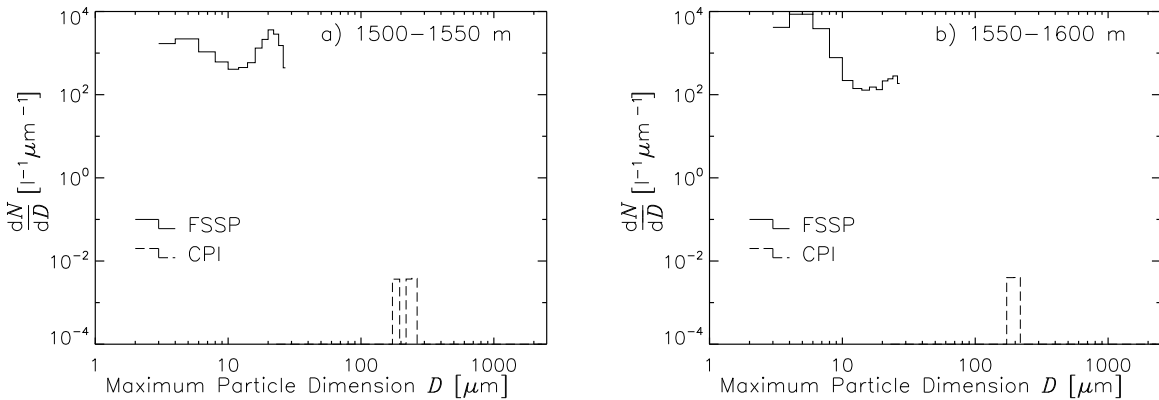


Figure 7.8: Particle number size distribution $\frac{dN}{dD}$ measured by FSSP and CPI within the cloud top layers of the cloud sampled on flight # 5 (c.f. Figure 4.18). The measurements are averaged between altitudes of 1500–1550 m (panel a) and 1550–1600 m (panel b).

cloud layer. The CPI registered ice particles only at five times. The mean number size distributions of the cloud particles measured by the FSSP in the uppermost cloud layers are analyzed in detail in Figure 7.8. The measurements are averaged for two layers between 1500–1550 m (36 measurements, panel a) and 1550–1600 m altitude (33 measurements, panel b). Both layers show a two modal particle distribution. For 1500–1550 m altitude the mode of the larger particles is dominant and has an effective diameter of $D_{\text{eff}} = 21.5 \mu\text{m}$ which is larger than the mean effective diameter of the liquid water droplets used in the simulations. This is consistent with the increase of the cloud droplet effective diameter towards cloud top for adiabatic cloud layers as reported by *e.g.*, Miles *et al.* (2000); Zuidema *et al.* (2005).

In the uppermost cloud layer (Figure 7.8b) a high concentration of small cloud particles ($D_{\text{eff}} = 6.5 \mu\text{m}$) has been observed. On the origin of this mode of small particle can be only speculated. Splashing of large liquid water droplets or shattering of ice crystals at the tip of the instrument housing might be a reason (*cf.* Section 4.3.1).

To analyze the thermodynamic phase of the small particle mode asymmetry parameter are calculated from the NSD presented in Figure 7.8 and compared to the Polar Nephelometer measurements. From the Polar Nephelometer values of $\langle g \rangle = 0.85$ and $\langle g \rangle = 0.84$ were obtained for the layers of 1500–1550 m and 1550–1600 m altitude, respectively. Assuming all particles to be liquid water droplets results in asymmetry parameters of 0.86 and 0.84, respectively, similar to the Polar Nephelometer. Assuming the mode of small particles ($D \leq 10 \mu\text{m}$) to be composed of ice crystals (columns) the calculated asymmetry parameter of the uppermost layer is reduced to $\langle g \rangle = 0.78$ while for the second layer (1500–1550 m) the asymmetry parameter does almost not change. This reveals that for the uppermost layer the small particle mode contribute significantly to the mean asymmetry parameter while for the second layer the larger particles are dominant.

In the Polar Nephelometer measurements within the uppermost cloud layer only five single measurements exhibit an asymmetry parameter lower than 0.82 with the majority being higher ($\langle g \rangle \approx 0.85$). Consequently the agreement between measured and calculated

asymmetry parameter (assuming all sampled particles to be liquid water droplets) suggest that the small particle mode is composed of liquid water droplets. However, the NSDs of the FSSP used for the calculation of g are cut at the maximum particle size ($28\ \mu\text{m}$) registered by the FSSP while the Polar Nephelometer measures particles up to about $800\ \mu\text{m}$ diameter. From the equation for the volumetric asymmetry parameter (*cf.* Eq. 3.40) follows that larger particles with higher scattering cross section have a larger impact on the volumetric asymmetry parameter than smaller cloud particles. Therefore, the truncation of larger cloud droplets not considered in the calculations of $\langle g \rangle$ may have biased the resulting $\langle g \rangle$ towards lower values. Due to these limitations of the *in situ* measurements the evidence of ice crystals at cloud top could neither been proven nor neglected by the analysis of the data. Nevertheless, with regard to the ice absorption observed in the SMART-Albedometer measurements and the radiative transfer simulations presented above an evidence of ice crystals at cloud top was found.

7.5 Observation of Glory

The backscatter glory is an optical phenomena based on single scattering processes and typical for liquid water clouds. The intensity variations of the reflected radiation reflects the single scattering phase function of the liquid water droplets located at cloud top. Therefore, the observations of backscatter glories are used by eg. Gedzelman (2003); Mayer *et al.* (2004) to retrieve the cloud droplet effective diameter.

During the measurement flights of ASTAR 2007 frequently backscatter glory have been observed by eye and photo camera. The photographs have not been taken systematically. However, two exemplary photographs taken on flight # 5 (April 7, 11:05 UTC, 78°N , 11.5°E) and flight # 10 (April 10, 11:31 UTC) are shown in Figure 7.9. The ice indices measured during the time periods at which the glories have been observed are $I_S = 26.0$, $I_P = 1.9$ and $I_S = 26.3$, $I_P = 2.9$ respectively. The ice indices are slightly lower than for the mixed-phase cloud for which the closure study is conducted. However, the values are higher than expected for pure liquid water clouds and indicate the presence of ice crystals

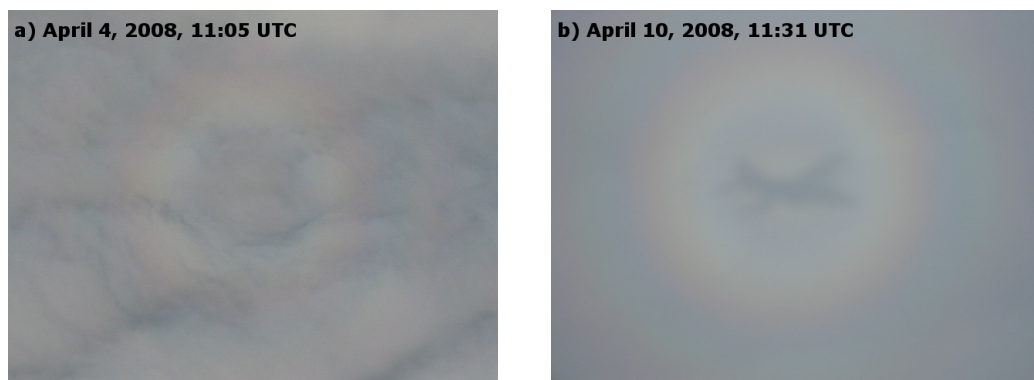


Figure 7.9: Photographs of backscatter glories at cloud top. The left photograph was taken on flight # 5 (April 7, 11:05 UTC), the right on flight # 10 (April 10, 11:31 UTC) from the POLAR 2 aircraft.

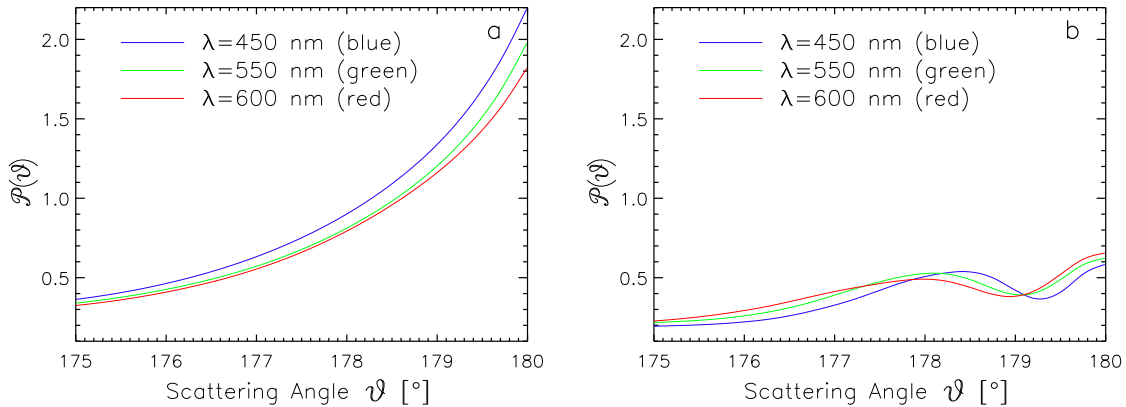


Figure 7.10: Scattering phase function $\mathcal{P}(\vartheta)$ at three different wavelengths representative for the blue (450 nm), green (550 nm) and red (600 nm) color. The backscattering range between scattering angles $\vartheta = 175\text{--}180^\circ$ is shown. In panel a $\mathcal{P}(\vartheta)$ is given for the ice crystal population (columns), in panel b for the liquid water droplet population used in the simulations.

at the same time the glories have been observed.

The presence of ice crystals at the cloud top of the observed ABM clouds was also concluded by the study shown above in Section 7.4. However, the observations of the backscatter glory puts this finding into question as the scattering phase function $\mathcal{P}(\vartheta)$ of ice crystals does not exhibit this feature. Figure 7.10 shows an extract of $\mathcal{P}(\vartheta)$ of the ice crystals (columns) and liquid water droplet populations used in the simulations analyzed above. Displayed are the three wavelengths $\lambda = 450$ nm, $\lambda = 550$ nm and $\lambda = 600$ nm representative for the blue, green and red color of the VIS solar radiation.

In Figure 7.10a $\mathcal{P}(\vartheta)$ of the ice crystals increases with increasing scattering angle. This is related to the large particle size of $D_{\text{eff}}^{\text{I}} = 103 \mu\text{m}$. The larger the particle size the higher the backscattering ($\vartheta = 180^\circ$) which is mainly caused by specular reflection at the ice crystal surface. Additional to the maximum at $\vartheta = 180^\circ$ liquid water droplets (Figure 7.10b) have a second maximum of $\mathcal{P}(\vartheta)$ at about $\vartheta = 178^\circ$ for 550 nm and 600 nm wavelengths and at about $\vartheta = 178.5^\circ$ for 450 nm. This second maximum causes the increased intensity of reflected radiation observed on the glory phenomena. The shift of the maximum for the different wavelengths produces the rainbow like colors of the glories.

3D Monte Carlo simulations have been performed to calculate the angular distribution of radiation scattered into the backscatter range $\vartheta \geq 175^\circ$. Considering the solar zenith angle of 71° this corresponds to viewing zenith angles between 71° and 76° . For the 3D radiative transfer simulations the MYSTIC code (Monte Carlo code for the physically correct tracing of photons in cloudy atmospheres) embedded in the *libRadtran* package was applied (Mayer, 1999, 2000). With MYSTIC the backscattered radiance was calculated for the flight altitude of 1800 m approximately 200 m above cloud top. In the simulations the angular extension of the solar disk of 0.5° is considered. Therefore, the radiance distribution is convoluted with $\sqrt{\theta_{\text{S}}^2 - (\theta - \theta_0)^2}$ where θ_0 is the solar zenith angle specified for the center of the solar disk and θ_{S} the angular radius of the solar disk. The convolution

causes a slight smoothing of the resulting radiance distribution which is not essential for the conclusions presented here but large enough to be considered.

Finally, the radiances were converted to color following the procedure by the Commission Internationale de l'Éclairage (CIE, CIE, 1986). The procedure is implemented in the C program *specrend.c* provided by CIE which was applied here (<http://www.fourmilab.ch/documents/specrend/>). In brief, the tristimulus values X , Y , and Z were derived by integrating the spectral radiance (calculated with a step of 5 nm between 380 nm and 780 nm) multiplied with the three color matching functions. X , Y , and Z are then converted to color (R,G,B) values using the CIE system matrix. The brightness is considered by multiplying (R,G,B) with the luminosity Y . A detailed description of the procedure is provided at the mentioned web page.

The angular distribution of the R,G,B colors were calculated for the three clouds Case A, C and D. Values of R,G,B normalized to the value at backscattering angle $\vartheta = 71^\circ$ are shown in the left panels of Figure 7.11 for a viewing azimuth angle parallel to the azimuth of the Sun. In the right panels R,G,B images are calculated by rotating the angular distributions shown in the left panels. The rotating of the simulations for one single viewing azimuth is justified as additional simulations showed that the glory is symmetrical to the backscattering angle. In the results simulated for the ABM cloud dominated by liquid water at cloud top (Case A) the backscatter glory is visible. Although the simulations exhibit some noise, the normalized radiance reflects the scattering phase function of the liquid water droplets (*cf.* Figure 7.10). The noise is due to the number of photons used in the Monte Carlo radiative transfer simulations but is not essential for the conclusions presented here. The wavelength shift of the secondary maximum is only weak in the simulations what results in the almost white color of the rotated image. This is due to the broad number size distribution of the liquid water droplets ($\sigma = 0.35$) used in the simulations (*cf.* Section 5.3). As shown by Mayer and Emde (2007) the colors of the backscatter glory are less pronounced if broad droplet size distributions are used. These findings are contrary to the glory photographs presented in Figure 7.9 but may result from the differences of the location of the *in situ* measurements and the location the photographs were taken.

For Case C where an ice layer of $\tau = 0.5$ is situated inside the uppermost cloud layer the backscatter glory is weaker than observed for Case A, but still visible in the rotated R,G,B image. Close to the backscattering angle the radiance is higher than in Case A. This spot is caused by the enhanced backscattering of the ice crystals. In airborne observations this spot is covered by the shadow of the aircraft and hence not visible. These results show that ice crystals of an optical thickness less than 0.5 situated inside the liquid water layer can reproduce the simultaneous observation of ice absorption and glory phenomena. Contrarily, Case D where the same ice layer is located above the liquid water layer the backscatter glory was not reproduced by the simulations. The angular distribution of the radiance shows similar characteristics as the scattering phase function of the ice crystals (*cf.* Figure 7.10). From this analysis it is concluded that Case D does not suit the remote sensing observation above ABM clouds obtained during ASTAR 2007.

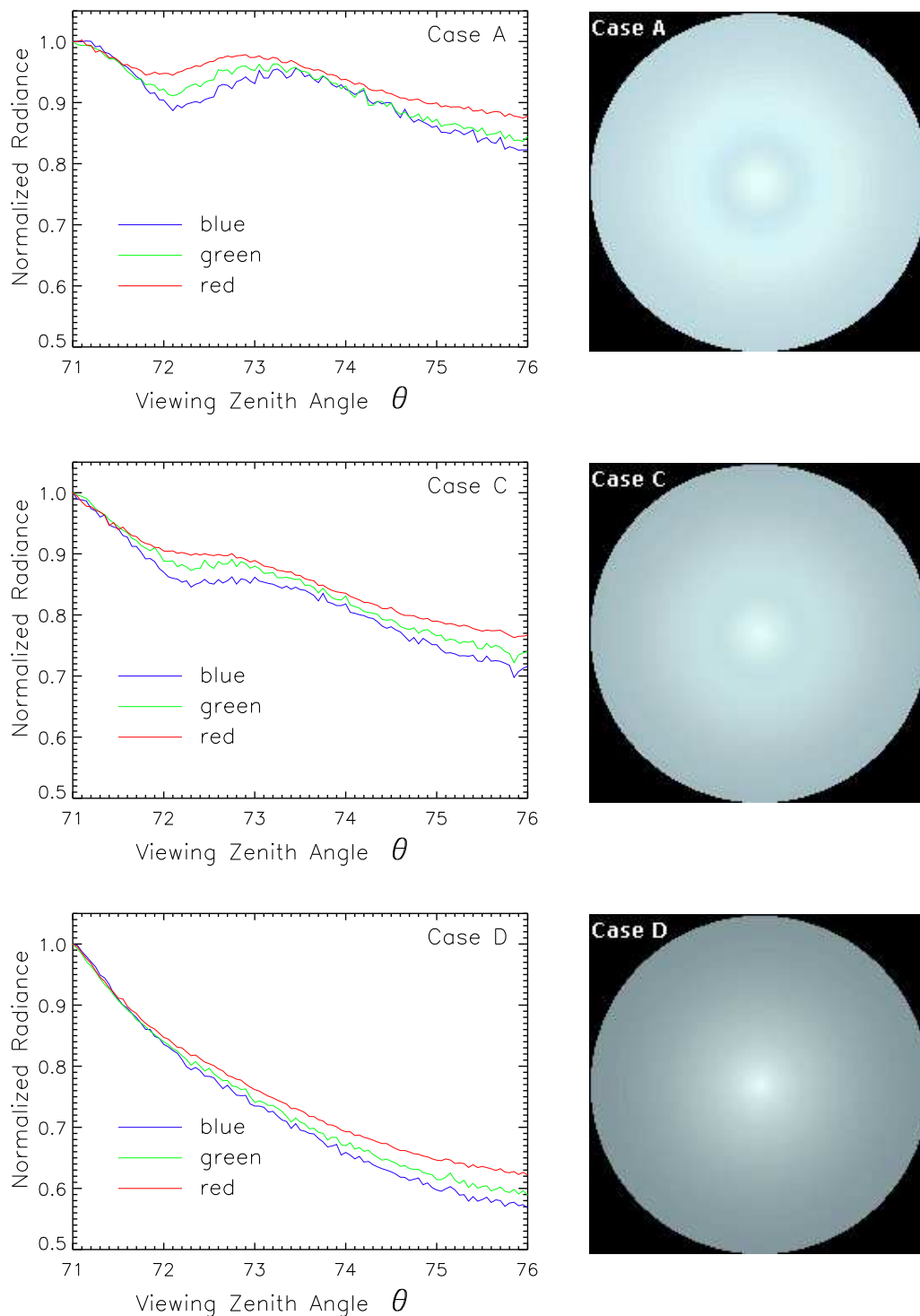


Figure 7.11: Radiative transfer simulations of the angular distribution of spectral radiances of the backscattering region. Results are shown for the three cases A, C and D. The left panels show the angular distribution converted into R,G,B colors. The visualization of the glory is given in the right panels.

8 Summary, Conclusions and Outlook

Within this work the radiative properties of ABM clouds have been investigated by radiative transfer simulations and respective airborne measurements of spectral solar radiation. The simulations of broadband solar and IR irradiances were used to characterize the cloud radiative forcing of the clouds as a function of ice crystal properties. From the airborne measurements information on the ice crystal properties were retrieved from different methods. These two issues are summarized in the following sections. Finally an outlook on a follow-up project is given.

Field Campaign

Boundary-layer clouds have been sampled during the ASTAR 2007 campaign in the vicinity of Svalbard. The clouds were generated over the open sea by a cold air outbreak with northerly winds. Besides the SMART-Albedometer, *in situ* instruments measuring microphysical properties of cloud particles and the airborne lidar AMALi were operated on board of the POLAR 2 aircraft. These instruments were used to derive independent information on the cloud thermodynamic phase. Predominantly, mixed-phase clouds were identified from the depolarization measurements of AMALi and the cloud microphysical properties (asymmetry parameter, ice crystal and liquid water droplet number concentrations). These data were used to define the cloud properties in the radiative transfer simulations.

Cloud Radiative Forcing

The radiative forcing of ABM clouds was investigated by extensive solar and IR radiative transfer simulations. In general it was found that the clouds cool the subjacent surface. However, the cooling strongly depends on the ice crystal properties such as ice crystal size, shape and number concentration. Therefore, the mixing state of the clouds was defined by two different approaches. The ice volume fraction $f_I = IWP/(IWP + LWP)$ relates the ice water path and the total water path while the ice optical fraction $f_I^* = \tau_I/(\tau_I + \tau_W)$ refers to the partial optical thickness of the ice and liquid water particles.

If the total water path is kept constant the variation of f_I significantly changes the cloud radiative forcing at the surface with the stronger cooling observed for pure liquid water clouds. It was found that these differences result from the different particle sizes of ice crystals and liquid water droplets. As ice crystals are typically larger, less ice crystals are required for the same total water path. Consequently, the cloud optical thickness and the radiative forcing are reduced. This relation is the stronger the larger the effective diameter of the ice crystals is in the simulations. For $D_{\text{eff}}^I = 150 \mu\text{m}$ the surface radiative forcing weakens from -240 W m^{-2} to -110 W m^{-2} between pure liquid water clouds and pure ice clouds.

These findings may have a significant impact on the physical processes which are responsible for the persistence of ABM clouds. A higher ice volume fraction reduces the solar

cooling of the surface. Consequently, for an unchanged IR radiative forcing (constant cloud temperature) the surface temperature increases and the temperature stability is reduced. This leads to enhanced updrafts and condensation of liquid water droplets which finally reduces f_{I} . This negative feedback suggests that a possible glaciation of ABM clouds is weakened due to radiative effects. However, simulations with cloud resolving dynamical models are necessary to confirm these findings quantitatively.

Furthermore, the impact of different ice crystal shapes on the radiative properties (layer reflectance, transmittance and absorptance) of ABM clouds was investigated. Similar to the variation of f_{I} it was found that the reduced volume of nonspherical ice crystals compared to spherical crystals reduces the cloud optical thickness and the cloud layer reflectance. The largest effects were found assuming aggregates as ice crystal habit while the results for column shaped ice crystals deviate less from the simulations assuming spherical ice crystals. These shape effects imply that processes by which the ice crystal shape changes (like aggregation of small ice crystals or splintering of ice crystals) may affect the cloud radiative forcing similar to the variation of f_{I} .

In a second approach the radiative forcing of mixed-phase clouds was calculated for clouds of various ice optical fractions f_{I}^* by keeping the total optical thickness of the clouds unchanged. The impact of f_{I}^* on the cloud radiative forcing was found to be less strong than for f_{I} . Only the differences in the scattering phase function and single scattering albedo of nonspherical ice crystals and liquid water droplets varied the cloud radiative forcing. The higher single scattering albedo of large ice crystals increases the absorption of radiation within the cloud compared to pure liquid water clouds and slightly increases the surface cooling from -235 W m^{-2} to -250 W m^{-2} . At the top of the atmosphere an increasing f_{I}^* was found to reduce the cooling effect from -220 W m^{-2} to -210 W m^{-2} . This effect is caused by the scattering phase function of nonspherical ice crystal which shows an enhanced sideward scattering. Therefore, for the low solar zenith angles persistent in Arctic regions the radiation reflected at cloud top increases with increasing f_{I}^* .

This effect caused by the different scattering phase functions is even more pronounced if the cloud top reflectance is considered. The spectral simulations of R revealed that an increasing f_{I}^* leads to an increase of R in the wavelength range below 1300 nm. For larger wavelengths the spectral pattern of R varies with f_{I}^* corresponding to the spectral absorption of ice and liquid water.

Remote Sensing of Ice Crystal Properties

Within this work the SMART-Albedometer was further developed to provide measurements of spectral radiances. From the simultaneous measurements of F_{λ}^{\downarrow} and I_{λ}^{\uparrow} the cloud top reflectance R was calculated. As satellite retrieval algorithms of cloud microphysical and optical properties are based on the measurements of R the radiance measurements with the SMART-Albedometer enables to apply satellite retrieval methods to the data. New radiance optical inlets have been constructed and characterized. The opening angle of these optical inlets depends on the diameter of the optical fiber connected to the inlet.

For the optical fibers used during the ASTAR 2007 campaign an opening angle of 2.1° was determined. The sharpness and wavelength dependence of the opening angle was improved by an additional aperture placed in front of the radiance optic.

For the absolute calibration of the radiance measurements two independent methods were applied. The calibration with an integrating sphere is limited due to the intensity of the sphere to wavelengths larger than 420 nm. For smaller wavelengths a calibration using a reflectance panel in combination with a 1000 W lamp as radiation source was applied.

The measurements of R obtained during the ASTAR 2007 campaign were analyzed with regard to information on the ice crystal properties of ABM clouds. To identify the cloud thermodynamic phase three different methods were applied. Two methods utilize the high spectral resolution of the measurements in the NIR wavelength range (1500–1800 nm) where spectral features of the ice and liquid water absorption are present in the measured R . From the analysis of the spectral slope in this wavelength range the ice index I_S was obtained similar to the cloud phase retrieval presented by Acarreta *et al.* (2004). The ice index I_P utilizes a principle component analysis of the spectral reflectance in the same wavelength range to subtract the magnitude of ice and liquid water absorption in the measurements. A third ice index I_A is based on the different sideward scattering of spherical liquid water particles and nonspherical ice crystals which was recorded in the VIS wavelength range of simultaneous measurements of spectral cloud top reflectance and albedo.

The analysis of I_S and I_P showed that both indices are capable to identify the cloud phase of Arctic boundary-layer clouds. In a case study (flight # 5) a pure ice cloud at the edge of a ABM cloud field also probed by *in situ* microphysical probes and observed by CALIPSO shows significantly higher values of I_S and I_P related to ice particles. The mixed-phase clouds inside the cloud field have lower ice indices than the ice cloud but higher values than expected for pure liquid water clouds. For a second case study (flight # 9) the ice indices were additionally compared to the depolarization signal measured by the airborne lidar system AMALi. The cloud parts where high depolarization indicates the presence of ice crystals are well correlated with high ice indices calculated from the SMART-Albedometer measurements.

A third ice index I_A based on the anisotropy of the reflected radiation and defined by the ratio between cloud top reflectance and albedo is not fully able to detect mixed-phase clouds. Simulations show that I_A is mainly affected by the uppermost cloud layers. The optical thickness of the relevant cloud layer is less than $\tau < 1.5$. Therefore, ABM clouds with liquid cloud top will be identified as pure liquid clouds. Nevertheless, for the edge of the cloud field observed on flight # 5 the presence of nonspherical ice crystals is confirmed.

At least for the cloud top layer the anisotropy ice index I_A is in theory a more robust indicator for the cloud phase than the spectral slope ice index I_S and the PCA ice index I_P . Sensitivity studies have shown that both indices I_S and I_P depend strongly on the ice particle effective diameter and less on the cloud optical thickness for $\tau < 5$. Nevertheless,

an ambiguity in the discrimination of ice and liquid water phase occurs only between pure ice clouds with small ice crystals and low τ and pure liquid water clouds of high τ . More crucial is the dependence on the ice particle effective diameter for the discrimination between mixed-phase and pure ice clouds. Here, *a priori* knowledge about the ice crystal dimensions is required.

The case study has shown, that the anisotropy ice index I_A is more difficult to interpret than I_S and I_P . The combination of three independent measurements and possible 3D radiative effects result in a higher uncertainty of this method. From a single measurement the retrieval of the cloud phase is not reliable. Cluster analysis or averaging is necessary.

In a second part measurements of R have been utilized to retrieve information on the vertical distribution of ice crystals in ABM clouds. Therefore, spectral radiative transfer simulations of R are performed and compared in a closure study to the measured R . The radiative transfer simulations based on the microphysical properties obtained during ASTAR 2007 underestimate R over the entire wavelength range covered by the SMART-Albedometer. This indicates that the cloud optical thickness is underestimated by the *in situ* measurements probably caused by cloud inhomogeneities which bias the averaged cloud microphysical properties. Scaling the cloud optical thickness the radiative transfer simulations failed to reproduce the spectral pattern of R observed in the wavelength range dominated by ice and liquid water absorption (1500–1800 nm). Varying the ice optical fraction did not improve the results significantly.

A good agreement between measurements and simulations was obtained when a thin ice layer of $\tau = 0.5$ is added in the simulations at cloud top and suggest that ice crystals were present in the uppermost layers of the observed ABM clouds. Detailed analysis of the *in situ* measurements could neither confirm nor reject these results. On top of the investigated clouds backscatter glories have been observed what generally indicates the presence of liquid water droplets at cloud top. This observation was validated by 3D radiative transfer simulations focusing on the radiation within the backscatter region. Adding ice crystals in the uppermost cloud layer but not above the liquid water layer reproduced a weak but visible backscatter glory and explains the observations. Situating the thin ice layer above the original cloud diminished the backscatter glory.

These investigations have shown that ice crystals at cloud top are missing in the microphysical properties derived from the *in situ* measurements. However, these data were used to define the cloud properties in the radiative transfer simulations. Consequently, the presence of ice crystals at cloud top may alter the calculated ice indices and the radiative forcing of ABM clouds. The enhanced ice absorption by these ice crystals will bias the ice indices of ABM clouds towards higher values. The radiative cooling by ABM cloud might be stronger than calculated due to the enhanced side scattering of ice crystals.

Furthermore, the evidence of ice crystals at the top of ABM clouds has implications for the physical processes occurring within these clouds. The common vertical structure of ABM clouds with a liquid water layer at cloud top and an ice layer with precipitating ice

crystals below as described by e. g., McFarquhar *et al.* (2007); Shupe *et al.* (2006) might be modified. Ice crystals are present within the entire cloud although liquid water droplets are dominant at cloud top. These findings suggest conclusions on the dominating physical ice production mechanisms. Durant and Shaw (2005) describe the ice nucleation mechanism due to evaporation freezing which occurs mainly at the cloud top and downdrafts where liquid water droplets evaporate. This process was analyzed by Fridlind *et al.* (2007) and Fan *et al.* (2008) for ABM clouds. The observed clouds were well reproduced by dynamical models if the enhanced ice nucleation by droplet evaporation freezing is considered. The location of the maximum ice nucleation rate is found near the cloud top and cloud bottom what is in agreement with the findings of this work. Contrarily, simulations neglecting evaporation freezing show ice crystals to be dominant at lower cloud layers only (*e.g.*, Harrington *et al.*, 1999; Morrison *et al.*, 2008; Avramov and Harrington, 2008).

The analysis of the spectral cloud top reflectance measured by the SMART-Albedometer has shown that the spectral information within the wavelength range 1500–1800 nm is essential to retrieve information on the ice crystal properties. In this regard the vertical footprint of the SMART-Albedometer measurements was investigated. Using the box airmass factor (box-AMF) approach presented by (Wagner *et al.*, 2007) the contribution of each cloud layer to the ice and liquid water absorption reflected in the measurements of R was quantified. The vertical profile of the box-AMF showed that the signal measured by the SMART-Albedometer is dominated by absorption processes within the uppermost cloud layers of less than 200 m thickness what is in agreement with the findings presented by Platnick (2000). However, box-AMF calculated for different wavelengths (1510 nm and 1710 nm) showed different vertical profiles related to different vertical footprints of the SMART-Albedometer measurements. These differences results from the spectral pattern of the ice and liquid water absorption. Consequently, by analyzing the spectral pattern of the measured R information on the vertical distribution of cloud particles can be retrieved.

Similar investigations have been conducted by *e.g.*, Chang and Li (2002, 2003) and Chen *et al.* (2008) who used four different wavelength bands of MODIS measurements (1250 nm, 1650 nm, 2150 nm and 3750 nm) to retrieve the vertical variation of the cloud droplet effective diameter from remote sensing. The investigations presented in this work suggest that these methods are adaptive to high spectral measurement of a small wavelength region as obtained by the SMART-Albedometer. The only requirement is that the measurements resolve changes in the spectral absorption of ice and liquid water.

Outlook

In this work detailed information on the vertical distribution of ice crystals and liquid water droplets within ABM clouds are obtained. These can be used to derive more accurate estimates of the net radiative forcing of ABM cloud. Simulations accounting for

different surface albedos and solar zenith angles will help to calculate annual values of the cloud radiative forcing. These are crucial for the prediction of the Arctic climate change. From the measurements obtained during ASTAR 2007, it was found that boundary-layer cloud fields show a high variability in the derived ice indices closely related to the ice optical and volume fraction. Considering the different radiative properties of clouds dominated by ice and liquid water it can be assumed that the heterogenous distribution of ice and liquid water in such cloud fields has an impact on the 3D radiative transfer. The cloud solar radiative forcing as well as satellite retrieval of cloud optical properties may be biased. This issue will be addressed in a follow-up project called SoRPIC (Solar Radiation and Phase Discrimination of Arctic Clouds) which includes an airborne field campaign in April 2010. During this campaign the SMART-Albedometer will be operated together with the hyperspectral camera system AISA EAGLE from SPECIM LTD. EAGLE is a linescanner using a CCD camera. It has a swath width of 36° with a horizontal resolution of 0.7 m at 1000 m flight altitude. For each pixel the spectral wavelength range between 400 nm and 970 nm is covered with 3 nm resolution. The high spacial and spectral resolution of EAGLE is suitable to investigate cloud inhomogeneities. Together with 3D radiative transfer simulation the measurements will help to estimate the impact of the inhomogeneous distribution of ice and liquid water particles on the radiative transfer.

List of Symbols

α_A	Ångstrom exponent	1
$\hat{\alpha}$	Parameter of Gamma-distribution	1
β	Total attenuated backscatter coefficient	$\text{sr}^{-1} \text{km}^{-1}$
β_A	Aerosol optical thickness at $\lambda = 1 \mu\text{m}$	1
β_I	Anisotropy factor	1
$\hat{\beta}$	Parameter of Gamma-distribution	1
γ_i	Component weightings (PCA)	1
γ_I	Component weightings for ice absorption	1
γ_W	Component weightings for liquid water absorption	1
$\hat{\gamma}$	Parameter of Gamma-distribution	l^{-1}
δ	Incident angle with respect to radiance optical inlet	$^\circ$
δ_{\min}	Minimum incident angle	$^\circ$
δ_{\max}	Maximum incident angle	$^\circ$
δ_D	Dirac-Delta-function	1
θ	Zenith angle	$^\circ$
θ_i	Zenith angle, incident direction	$^\circ$
θ_r	Zenith angle, reflected direction	$^\circ$
θ_0	Solar zenith angle	$^\circ$
θ_S	Angular radius of the solar disk	$^\circ$
ϑ	Scattering angle	$^\circ$
λ	Wavelength	nm or μm
λ_1	First wavelength used in I_P	nm
λ_2	Last wavelength used in I_P	nm
λ_a	First wavelength used in I_S	nm
λ_b	Last wavelength used in I_S	nm
μ	Cosine of the zenith angle θ	1
μ_i	Cosine of the zenith angle θ_i	1
μ_0	Cosine of the solar zenith angle θ_0	1
σ	Logarithmic width of log-normal distribution	1
τ	Cloud optical thickness	1
τ_W	Liquid water droplets partial optical thickness	1
τ_I	Ice crystals partial optical thickness	1
τ_W^{top}	Optical thickness of liquid water layer at cloud top	1
$\hat{\tau}_W$	Retrieved optical thickness (Liquid water cloud)	1
$\hat{\tau}_I$	Retrieved optical thickness (Ice cloud)	1
π	Circular constant 3.14159...	1
ρ	Albedo	1
φ	Azimuth angle	$^\circ$
φ_i	Azimuth angle, incident direction	$^\circ$

φ_r	Azimuth angle, reflected direction	$^\circ$
φ_0	Solar azimuth angle	$^\circ$
$\tilde{\omega}$	Single scattering albedo	1
$\tilde{\omega}'$	Delta-scaled single scattering albedo	1
$\langle \tilde{\omega} \rangle$	Volumetric single scattering albedo	1
$\langle \tilde{\omega} \rangle^I$	Volumetric single scattering albedo (ice mode)	1
$\langle \tilde{\omega} \rangle^W$	Volumetric single scattering albedo (water mode)	1
Γ	Gamma function	1
Δ	Opening angle of radiance optical inlet	$^\circ$
$\Delta\theta$	Horizontal aircraft misalignment	$^\circ$
Λ	Truncation order	1
Φ	Radiant energy flux	W
$\hat{\Omega}$	Direction of propagation	sr
$d\Omega$	Solid angle	sr
\hat{a}_i	Box air mass factor	1
b_{abs}	Volumetric absorption coefficient	m^{-1}
b_{ext}	Volumetric extinction coefficient	m^{-1}
b_{ext}^I	Volumetric extinction coefficient (ice mode)	m^{-1}
b_{ext}^W	Volumetric extinction coefficient (water mode)	m^{-1}
b_n	Moments of the Legendre expansion of \mathcal{P}	1
$\langle b_n \rangle$	Volumetric Legendre moments	1
b_{sca}	Volumetric scattering coefficient	m^{-1}
c_n	Moments of the Legendre expansion of h	1
d	Aperture diameter	cm
d_1	Horizontal footprint of radiance measurements	m
f_{dir}	Fractional amount of $F_{\text{dir}}^\downarrow$	1
f_I	Ice volume fraction	1
f_I^*	Ice optical fraction	1
f_{tr}	Fraction of truncated energy	1
g	Asymmetry parameter	1
$\langle g \rangle$	Volumetric asymmetry parameter	1
$\langle g \rangle^I$	Volumetric asymmetry parameter (ice mode)	1
$\langle g \rangle^W$	Volumetric asymmetry parameter (water mode)	1
h	Truncation function	1
i	Order of principle component analysis	1
l	Distance between lamp and reflectance panel	cm
l_0	Certified distance to the reflectance panel	cm
n	Order of the Legendre polynomials and moments	1
\hat{n}	Surface orientation of dA	1
\hat{n}_\perp	Surface orientation of dA_\perp	1

\tilde{n}_i	Imaginary part of the refractive index	1
r	Distance to the center of the radiance optic	mm
r_{\min}	Minimum distance to the center of the radiance optic	mm
r_{\max}	Maximum distance to the center of the radiance optic	mm
\hat{s}	Normalized vertical footprint	% m ⁻¹
z	Altitude	m
z_{top}	Cloud top altitude	m
z_{base}	Cloud base altitude	m
A	Particle cross section	m ²
\hat{A}	Air mass factor	1
A_{lens}	Total lens area	mm ²
A_S	Cross section of a sphere	m ²
dA	Unit surface	m ²
dA_{\perp}	Unit surface perpendicular to $\hat{\Omega}$	m ²
$C_{\lambda,P}$	Calibration factor (Panel)	W m ⁻² sr ⁻¹ nm ⁻¹
$C_{\lambda,S}$	Calibration factor (Sphere)	W m ⁻² sr ⁻¹ nm ⁻¹
C_T	Transfer calibration factor	
C_{abs}	Absorption cross section	m ²
C_{ext}	Extinction cross section	m ²
C_{sca}	Scattering cross section	m ²
C'_{abs}	Delta-scaled absorption cross section	m ²
C'_{sca}	Delta-scaled scattering cross section	m ²
D	Maximum particle dimension	μm
D_F	Diameter of optical fiber	mm
D_{eff}	Particle effective diameter	μm
D_{eff}^I	Ice crystal effective diameter	μm
D_{eff}^W	Liquid water droplet effective diameter	μm
D_m^I	Ice crystal mean diameter	μm
D_m^W	Liquid water droplet mean diameter	μm
D_M^W	Liquid water droplet median diameter	μm
E	Angular efficiency	1
F	Irradiance	W m ⁻²
F_i	Incident irradiance	W m ⁻²
F_{λ}	Spectral irradiance	W m ⁻² nm ⁻¹
$F_{\lambda,S}$	Spectral irradiance of a radiation source	W m ⁻² nm ⁻¹
$F_{A,\text{cloud}}$	Absorbed irradiance (cloudy case)	W m ²
$F_{A,\text{clear}}$	Absorbed irradiance (clear sky)	W m ²
$F_{A,\text{CL}}$	Absorbed irradiance by cloud layer	W m ²
F^{\downarrow}	Downward irradiance	W m ⁻²
F^{\uparrow}	Upward irradiance	W m ⁻²
$F_{\text{diff}}^{\downarrow}$	Diffuse downward irradiance	W m ⁻²

$F_{\text{dir}}^{\downarrow}$	Direct downward irradiance	W m^{-2}
F_{λ}^{\downarrow}	Spectral downward irradiance	$\text{W m}^{-2} \text{nm}^{-1}$
F_{λ}^{\uparrow}	Spectral upward irradiance	$\text{W m}^{-2} \text{nm}^{-1}$
I	Radiance	$\text{W m}^{-2} \text{sr}^{-1}$
I_0	Radiance for isotropy	$\text{W m}^{-2} \text{sr}^{-1}$
I_{λ}	Spectral radiance	$\text{W m}^{-2} \text{sr}^{-1} \text{nm}^{-1}$
$I_{\lambda, \text{S}}$	Spectral radiance of integrating sphere	$\text{W m}^{-2} \text{sr}^{-1} \text{nm}^{-1}$
I_{r}	Reflected radiance	$\text{W m}^{-2} \text{sr}^{-1}$
$I_{\text{r,L}}$	Lambertian reflected radiance	$\text{W m}^{-2} \text{sr}^{-1}$
I_{dir}	Direct radiance	$\text{W m}^{-2} \text{sr}^{-1}$
I_{diff}	Diffuse radiance	$\text{W m}^{-2} \text{sr}^{-1}$
I_{r}^{\uparrow}	Reflected radiance, nadir direction	$\text{W m}^{-2} \text{sr}^{-1}$
I_{λ}^{\downarrow}	Spectral downwelling radiance	$\text{W m}^{-2} \text{sr}^{-1} \text{nm}^{-1}$
I_{λ}^{\uparrow}	Spectral upwelling radiance	$\text{W m}^{-2} \text{sr}^{-1} \text{nm}^{-1}$
I_{A}	Anisotropy ice index	1
I_{P}	PCA ice index	1
I_{S}	Spectral slope ice index	1
$I_{\text{S}}^{\text{Knap}}$	Ice index (Knap <i>et al.</i> (2002))	1
J_{dir}	Single scattering term	$\text{W m}^{-2} \text{sr}^{-1}$
J_{diff}	Multiple scattering term	$\text{W m}^{-2} \text{sr}^{-1}$
L_{S}	Slant photon path	m
L_{V}	Vertical photon path	m
N	Number of cloud layers	1
N_{tot}	Total particle number concentration	l^{-1} or cm^{-3}
$N_{\text{tot}}^{\text{I}}$	Total ice crystal concentration from CPI	l^{-1} or cm^{-3}
$N_{\text{tot}}^{\text{W}}$	Total liquid water droplet concentration from CPI	l^{-1} or cm^{-3}
$N_{\text{tot}}^{\text{FSSP}}$	Total particle concentration from FSSP	l^{-1} or cm^{-3}
$N_{\text{tot}}^{\text{CPI}}$	Total particle concentration from CPI	l^{-1} or cm^{-3}
$\frac{dN}{dD}$	Particle number size distribution	$\text{l}^{-1} \mu\text{m}^{-1}$
$\left(\frac{dN}{dD}\right)^{\text{W}}$	Liquid water droplet number size distribution	$\text{l}^{-1} \mu\text{m}^{-1}$
$\left(\frac{dN}{dD}\right)^{\text{I}}$	Ice crystal number size distribution	$\text{l}^{-1} \mu\text{m}^{-1}$
P_n	Legendre polynomials	1
PC_i	Principle component	1
PC_{W}	Principle component for liquid water absorption	1
PC_{I}	Principle component for ice absorption	1
R	Reflectance	1
R_{P}	Reflectance panel	1
S	Digital spectrometer signal	1
S_0	Extraterrestrial solar irradiance	W m^{-2}
S_{lab}	Digital spectrometer signal, laboratory	1
S_{field}	Digital spectrometer signal, field	1
V	Particle Volume	m^3

V_S	Volume of a sphere	m^3
\mathcal{A}	Cloud layer absorptance	1
\mathcal{F}_Δ	Radiative forcing	W m^2
$\mathcal{F}_\Delta^{\text{sol}}$	Solar radiative forcing	W m^2
$\mathcal{F}_\Delta^{\text{IR}}$	Thermal IR radiative forcing	W m^2
\mathcal{P}	Scattering phase function	1
\mathcal{P}^*	Recalculated scattering phase function	1
\mathcal{P}_{tr}	Truncated scattering phase function	1
\mathcal{P}'_{tr}	Delta-scaled scattering phase function	1
$\langle \mathcal{P} \rangle$	Volumetric scattering phase function	1
$\langle \mathcal{P} \rangle^{\text{I}}$	Volumetric scattering phase function (ice mode)	1
$\langle \mathcal{P} \rangle^{\text{W}}$	Volumetric scattering phase function (water mode)	1
\mathcal{R}	Cloud layer reflectance	1
\mathcal{T}	Cloud layer transmittance	1
$BRDF$	Bidirectional reflectance distribution function	sr^{-1}
$BRDF_L$	Lambertian $BRDF$	sr^{-1}
BRF	Bidirectional reflectance factor	1
$FWHM$	Full width at half maximum	nm
IWC	Ice water content	mg l^{-1}
IWP	Ice water path	g m^{-2}
LWC	Liquid water content	mg l^{-1}
LWP	Liquid water path	g m^{-2}
TWP	Total water path	g m^{-2}

List of Abbreviations

1D	1-Dimensional
2D	2-Dimensional
3D	3-Dimensional
ABM	Arctic Boundary-layer Mixed-phase cloud
ACIA	Arctic Climate Impact Assessment
AMALi	Airborne Mobile Aerosol Lidar
AMF	Air Mass Factor
ASTAR	Arctic Study of Tropospheric Aerosol, Clouds and Radiation
AVIRIS	Airborne Visible and Infrared Imaging Spectrometer
AWI	Alfred Wegener Institute for Polar and Marine Research
CALIOP	Cloud-Aerosol Lidar with Orthogonal Polarization
CALIPSO	Cloud-Aerosol Lidar and Infrared Pathfinder Satellite Observation satellite
CCD	Charged-Coupled Device
CCN	Cloud Condensation Nuclei
CFDE	Canadian Freezing Drizzle Experiments
CIE	Commission Internationale de l'Éclairage
CPI	Cloud Particle Imager
DISORT	Discrete Ordinate Radiative Transfer solver
DKD	Deutscher Kalibrierdienst (German Calibration Service)
DLR	Deutsches Zentrum für Luft- und Raumfahrt (German Aerospace Center)
ENVISAT	Environmental Satellite
FIRE-ACE	Arctic Cloud Experiment of the First International satellite cloud climatology project Regional Experiment
FSSP	Forward Scattering Spectrometer Probe
GPS	Global Positioning System
IDL	Interactive Data Language
IPY	International Polar Year
IFT	Leibniz-Institute for Tropospheric research
IGOM	Improved Geometric Optics Method
IN	Ice Nuclei
INS	Inertial Navigation System
IR	Thermal Infrared wavelength range (here, 5–100 μm)
LaMP	Laboratoire de Météorologie Physique
<i>libRadtran</i>	Library for Radiative transfer
McArtim	Monte Carlo radiative transfer inversion model
MCS	Multi Channel Spectrometer

MELTEX	Impact of Melt ponds on Energy and momentum fluxes between atmosphere and ocean experiment
MISR	Multiangle Imaging Spectroradiometer
MODIS	Moderate Resolution Imaging Spectroradiometer
M-PACE	Mixed-Phase Arctic Clouds Experiment
MYSTIC	Monte Carlo code for the physically correct tracing of photons in cloudy atmospheres
NIST	National Institute of Standards and Technology
NIR	Near InfraRed wavelength range (here, 700–3000 nm)
<i>NIR</i>	Spectrometer covering the wavelength range 950–2200 nm
NSD	Number Size Distributions
POLDER	POLarization and Directionality of the Earth's Reflectances instrument
PMS	Particle Measuring System
PC	Personal Computer
PCA	Principle Component Analysis
PDA	Photo-Diode Array
PGS	Plane Grating Spectrometer
POLAR 2	AWI Polar Aircraft 2
PY-database	Database of ice crystal properties provided by Yang and Liou (1996a) and Yang <i>et al.</i> (2005)
R,G,B	Red, Green, Blue color model
RTE	Radiative Transfer Equation
SCIAMACHY	Scanning Imaging Absorption Spectrometer for Atmospheric Chartography
SHEBA	Surface Heat Budget of the Arctic Ocean experiment
SMART	Spectral Modular Airborne Radiation measurement sysTem
SNR	Signal to Noise Ratio
SoRPIC	Solar Radiation and Phase Discrimination of Arctic experiment
TOA	Top of the Atmosphere
UTC	Universal Time Coordinated
UV	Ultra Violet wavelength range (here, 100–380 nm)
VIS	Visible wavelength range (here, 380–700 nm)
<i>VIS</i>	Spectrometer covering the wavelength range 200–1050 nm
WBF	Wegener-Bergeron-Findeisen mechanism

List of Figures

1.1	Earth's and Arctic energy budget	2
1.2	Phase diagram of water	4
1.3	Mixed-phase cloud scheme	5
3.1	Geometry defining radiation quantities	10
3.2	Illustration of reflectance quantities	12
3.3	Spectral single scattering albedo of cloud particles	14
3.4	Scattering phase function of individual cloud particles	15
3.5	Legendre moments	17
3.6	Legendre moments - Delta-M scaled	19
3.7	Legendre moments - Delta-fit method	20
4.1	SMART-Albedometer basic setup	24
4.2	Radiance optical inlet - Photograph	25
4.3	Radiance optical inlet - Drawing	26
4.4	Ray tracing simulations for the radiance optical inlet	27
4.5	Footprint geometry	27
4.6	Opening angle of radiance optical inlet	28
4.7	Angular efficiency of the radiance optical inlet	29
4.8	Footprint of the radiance optical inlet	29
4.9	Calibration setup for radiance - A	30
4.10	Calibration setup for radiance - B	30
4.11	Radiance calibration factors	31
4.12	Technical drawings of SMART-Albedometer	32
4.13	Integration of SMART-Albedometer on POLAR 2	33
4.14	Transfer calibration factors	36
4.15	Spectral measurement uncertainty	37
4.16	Flight track of POLAR 2 aircraft on flight # 5	40
4.17	Separation of FSSP and CPI measurements	42
4.18	Profile of microphysical measurements (flight # 5)	43
4.19	Particle number size distribution (flight # 5)	44
4.20	Exemplary cloud top reflectance measurements.	47
4.21	Simultaneous measurements of cloud top reflectance and albedo.	47
5.1	Measured surface albedo and reflectance	49
5.2	Ice crystal shapes	51
5.3	Fitted particle number size distributions	52
5.4	Simulated cloud top reflectance using fitted NSDs	53
5.5	Impact of ice fraction on mixed-phase clouds	56
5.6	Relation between f_I and f_I^*	56
5.7	Volume and cross section of single particles of different shape	57
5.8	Solar radiative forcing of mixed-phase clouds	59
5.9	IR radiative forcing of mixed-phase clouds	61

5.10	Shape effect on cloud optical properties	63
5.11	Simulated spectral cloud top reflectance and albedo	65
6.1	Spectral slope ice index I_S	67
6.2	Component weightings from PCA of pure liquid water and ice clouds	68
6.3	PCA ice index I_P	69
6.4	Single scattering at cloud top	70
6.5	Scattering phase function of different individual cloud particles	70
6.6	Anisotropy factor for pure ice and liquid water clouds	72
6.7	Ice index I_P	73
6.8	Case study on flight # 5	76
6.9	Anisotropy factor for the case study on flight # 5	78
6.10	Flight track of POLAR 2 aircraft on flight # 9	79
6.11	Case study on flight # 9	81
7.1	Cloud geometries	82
7.2	Comparison of simulated and measured cloud top reflectance - A	84
7.3	Comparison of simulated and measured cloud top reflectance - B	86
7.4	Definition of the air mass factor	87
7.5	Box air mass factor simulated for Case A	88
7.6	Vertical footprint of radiance measurements	90
7.7	Comparison of simulated and measured cloud top reflectance - C	91
7.8	Particle size distribution at cloud top, flight # 5	92
7.9	Photographs of backscatter glory	93
7.10	Scattering phase function - Backscatter range	94
7.11	Glory simulations	96

List of Tables

4.1	SMART-Albedometer configuration.	34
4.2	Uncertainties of the SMART-Albedometer	35
4.3	Measurement flights ASTAR 2007	41
5.1	Measured surface albedo	48
5.2	Mean and effective particle diameter	63
6.1	Cloud properties used in radiative transfer simulations	66
6.2	Ice indices calculated from SMART-Albedometer measurements	67
6.3	Simulated ice indices	74
7.1	Closure of optical thickness	83
7.2	Closure of ice optical fraction	85
7.3	Ice indices for the simulations Case B1–B6	85

References

- Acarreta, J. R., Stammes, P., and Knap, W. H. (2004). First retrieval of cloud phase from SCIAMACHY spectra around $1.6\ \mu\text{m}$. *Atmos. Res.* **72**: 89–105.
- Allison, I., Beland, M., Alverson, K., Bell, R., Carlson, D., Danell, K., Ellis-Evans, C., Fahrback, E., Fanta, E., Fujii, Y., Glaser, G., Goldfarb, L., Hovelsrud, G., Huber, J., Kotlyakov, V., Krupnik, I., Lopez-Martinez, J., Mohr, T., Qin, D., Rachold, V., Rapley, C., Rogne, O., Sarukhajian, E., Summerhayes, C., and C., X. (2007). *The scope of science for the International Polar Year 2007–2008*. WMO/TD-No. 1364, 79 pp.
- Anderson, G., Clough, S., Kneizys, F., Chetwynd, J., and Shettle, E. (1986). *AFGL Atmospheric Constituent Profiles (0–120 km)*. Tech. Rep. AFGL-TR-86-0110, AFGL (OPI), Hanscom AFB, MA 01736.
- Avramov, A. and Harrington, J. Y. (2008). The influence of ice crystal habit on simulations of arctic mixed-phase clouds. In *Proceedings of the ICCP Conference*. Cancun, Mexico, July 7–11.
- Bergeron, T. (1935). On the physics of cloud and precipitation. In *Proceedings 5th Assembly U.G.G.I.*, p. 156–178. Lisbon, Portugal.
- Bierwirth, E. (2008). *Airborne Measurements of the Spectral Surface Albedo over Morocco and its Influence on the Radiative Forcing of Saharan Dust*. Ph.D. thesis, Johannes Gutenberg University Mainz, Germany.
- Bierwirth, E., Wendisch, M., Ehrlich, A., Heese, B., Tesche, M., Althausen, D., Schladitz, A., Müller, D., Otto, S., Trautmann, T., Dinter, T., von Hoyningen-Huene, W., and Kahn, R. (2009). Spectral surface albedo over Morocco and its impact on the radiative forcing of Saharan dust. *Tellus* **61B**: 252–269.
- Bohren, C. F. and Clothiaux, E. E. (2006). *Fundamentals of Atmospheric Radiation*. Wiley-VCH Verlag GmbH & Co. KGaA, Weinheim: 472 pp.
- Bohren, C. F. and Huffman, D. R. (1998). *Absorption and Scattering of Light by Small Particles*. Wiley-Interscience, New York: 530 pp.
- Boudala, F. S., Isaac, G. A., Cober, S. G., and Fu, Q. (2004). Liquid fraction in stratiform mixed-phase clouds from in situ observations. *Quart. J. Roy. Meteor. Soc.* **130**: 2.919–2.931.
- Buriez, J., Vanbauce, C., Parol, F., Goloub, P., Herman, M., Bonnel, B., Fouquart, Y., Couvert, P., and Seze, G. (1997). Cloud detection and derivation of cloud properties from POLDER. *Int. J. Remote Sensing* **18**: 2785–2813.
- Cahalan, R., Ridgway, W., Wiscombe, W., and Bell, T. (1994). The albedo of fractal stratocumulus clouds. *J. Atmos. Sci.* **51**: 2434–2455.

- Chang, F. L. and Li, Z. Q. (2002). Estimating the vertical variation of cloud droplet effective radius using multispectral near-infrared satellite measurements. *J. Geophys. Res.* **107**: 4257.
- Chang, F. L. and Li, Z. Q. (2003). Retrieving vertical profiles of water-cloud droplet effective radius: Algorithm modification and preliminary application. *J. Geophys. Res.* **108**: 4763.
- Chen, R. Y., Chang, F. L., Li, Z. Q., Ferraro, R., and Weng, F. Z. (2007). Impact of the vertical variation of cloud droplet size on the estimation of cloud liquid water path and rain detection. *J. Atmos. Sci.* **64**: 3843–3853.
- Chen, R. Y., Wood, R., Li, Z. Q., Ferraro, R., and Chang, F. L. (2008). Studying the vertical variation of cloud droplet effective radius using ship and space-borne remote sensing data. *J. Geophys. Res.* **113**: D00A02.
- Chepfer, H., Minnis, P., Young, D., Nguyen, L., and Arduini, R. F. (2002). Estimation of cirrus cloud effective ice crystal shapes using visible reflectances from dual-satellite measurements. *J. Geophys. Res.* **107**: 4730.
- Chou, M. D., Lee, K. T., and Yang, P. (2002). Parameterization of shortwave cloud optical properties for a mixture of ice particle habits for use in atmospheric models. *J. Geophys. Res.* **107**: Art. No. 4600.
- Chylek, P., Damiano, P., and Shettle, E. P. (1992). Infrared emittance of water clouds. *J. Atmos. Sci.* **49**: 1459–1472.
- Chylek, P., Robinson, S., Dubey, M. K., King, M. D., Fu, Q., and Clodius, W. B. (2006). Comparison of near-infrared and thermal infrared cloud phase detections. *J. Geophys. Res.* **111**: D20203.
- CIE (1986). *Standard on colorimetric observers*. Commission Internationale de l'Éclairage (CIE) cie s002 edition.
- Cober, S. G., Isaac, G. A., Korolev, A. V., and Strapp, J. W. (2001). Assessing cloud-phase conditions. *J. Appl. Meteor.* **40**: 1.967–1.983.
- Corell, R. (2004). *Arctic Climate Impact Assessment*. Cambridge University Press, Cambridge, UK: 139 pp.
- Crowther, B. (1997). *The Design, Construction, and Calibration of a Spectral Diffuse/Global Irradiance Meter*. Ph.D. thesis, University of Arizona.
- Curry, J. A., Ebert, E. E., and Herman, G. F. (1988). Mean and turbulence structure of the summertime Arctic cloudy boundary-layer. *Quart. J. Roy. Meteor. Soc.* **114**: 715–746.

- Curry, J. A., Rossow, W. B., Randall, D., and Schramm, J. L. (1996). Overview of Arctic cloud and radiation characteristics. *J. Climate* **9**: 1.731–1.764.
- Deutschmann, T. (2008). *The RTM McArtim*. Master’s thesis, University Heidelberg.
- Deutschmann, T. and Wagner, T. (2006). *TRACY-II User manual*, <http://joseba.mpch-mainz.mpg.de/Strahlungstransport.htm>.
- Dong, X. Q. and Mace, G. G. (2003). Arctic stratus cloud properties and radiative forcing derived from ground-based data collected at Barrow, Alaska. *J. Climate* **16**: 445–461.
- Durant, A. J. and Shaw, R. A. (2005). Evaporation freezing by contact nucleation inside-out. *Geophys. Res. Lett.* **32**: L20814.
- Ehrlich, A., Bierwirth, E., Wendisch, M., Gayet, J.-F., Mioche, G., Lampert, A., and Heintzenberg, J. (2008a). Cloud phase identification of arctic boundary-layer clouds from airborne spectral reflection measurements: Test of three approaches. *Atmos. Chem. Phys.* **8**: 7493–7505.
- Ehrlich, A., Wendisch, M., Bierwirth, E., Herber, A., and Schwarzenböck, A. (2008b). Ice crystal shape effects on solar radiative properties of Arctic mixed-phase clouds - Dependence on microphysical properties. *Atmos. Res.* **88**: 266–276.
- Fan, J., Ovtchinnikov, M., Comstock, J., McFarlane, S., and Khain, A. (2008). Modeling Arctic mixed-phase clouds and associated ice formation. In *Proceedings of the ICCP Conference*. Cancun, Mexico, July 7-11.
- Field, P. R., Wood, R., Brown, P. R. A., Kaye, P. H., Hirst, E., Greenaway, R., and Smith, J. A. (2003). Ice particle interarrival times measured with a fast FSSP. *J. Atmos. Oceanic Technol.* **20**: 249–261.
- Findeisen, W. (1938). Kolloidmeteorologische Vorgänge bei Niederschlagsbildung. *Meteor. Z.* **55**: 121–133.
- Fleishauer, R. P., Larson, V. E., and Vonder Haar, T. H. (2002). Observed microphysical structure of midlevel, mixed-phase clouds. *J. Atmos. Sci.* **59**: 1.779–1.804.
- Freedman, I. and Landsman, W. (1993). IDL procedure for principle component analysis *pca.pro*.
- Freese, D. and Kottmeier, C. (1998). Radiation exchange between stratus clouds and polar marine surfaces. *Bound.-Layer Meteor.* **87**: 331–356.
- Fridlind, A. M., Ackerman, A. S., McFarquhar, G., Zhang, G., Poellot, M. R., DeMott, P. J., Prenni, A. J., and Heymsfield, A. J. (2007). Ice properties of single-layer stratocumulus during the Mixed-Phase Arctic Cloud Experiment: 2. Model results. *J. Geophys. Res.* **112**: D24202.

- Garrett, T. J., Hobbs, P. V., and Gerber, H. (2001). Shortwave, single-scattering properties of arctic ice clouds. *J. Geophys. Res.* **106**: 15.155–15.172.
- Gayet, J., Crepel, O., Fournol, J., and Oshchepkov, S. (1997). A new airborne polar Nephelometer from the measurements of optical and microphysical cloud properties. Part I: Theoretical design. *Ann. Geophys.* **15**: 451–459.
- Gayet, J. F., Febvre, G., and Larsen, H. (1996). The reliability of the PMS FSSP in the presence of small ice crystals. *J. Atmos. Oceanic Technol.* **13**: 1.300–1.310.
- Gayet, J. F., Stachlewska, I. S., Jourdan, O., Shcherbakov, V., Schwarzenboeck, A., and Neuber, R. (2007). Microphysical and optical properties of precipitating drizzle and ice particles obtained from alternated lidar and in situ measurements. *Ann. Geophys.* **25**: 1487–1497.
- Gedzelman, S. D. (2003). Simulating glories and cloudbows in color. *Appl. Opt.* **42**: 429–435.
- Gerber, H., Takano, Y., Garrett, T. J., and Hobbs, P. V. (2000). Nephelometer measurements of the asymmetry parameter, volume extinction coefficient, and backscatter ratio in Arctic clouds. *J. Atmos. Sci.* **57**: 3.021–3.034.
- Giles, K. A., Laxon, S. W., and Ridout, A. L. (2008). Circumpolar thinning of Arctic sea ice following the 2007 record ice extent minimum. *Geophys. Res. Lett.* **35**: L22502.
- Glantz, P., Noone, K. J., and Osborne, S. R. (2003). Comparisons of airborne CVI and FSSP measurements of cloud droplet number concentrations in marine stratocumulus clouds. *J. Atmos. Oceanic Technol.* **20**: 133–142.
- Grenfell, T. C. and Warren, S. G. (1999). Representation of a nonspherical ice particle by a collection of independent spheres for scattering and absorption of radiation. *J. Geophys. Res.* **104**: 31.697–31.709.
- Hansen, J. (1971). Multiple scattering of polarized light in planetary atmospheres. Part II. Sunlight reflected by terrestrial water clouds. *J. Atmos. Sci.* **28**: 1400–1426.
- Harrington, J. Y., Reisin, T., Cotton, W. R., and Kreidenweis, S. M. (1999). Cloud resolving simulations of Arctic stratus - Part II: Transition-season clouds. *Atmos. Res.* **51**: 45–75.
- Herber, A., Thomason, L. W., Gernandt, H., Leiterer, U., Nagel, D., Schulz, K. H., Kaptur, J., Albrecht, T., and Notholt, J. (2002). Continuous day and night aerosol optical depth observations in the arctic between 1991 and 1999. *J. Geophys. Res.* **107**.
- Heymsfield, A. J., Bansemmer, A., Field, P. R., Durden, S. L., Stith, J. L., Dye, J. E., Hall, W., and Grainger, C. A. (2002). Observations and parameterizations of particle size distributions in deep tropical cirrus and stratiform precipitating clouds: Results from in situ observations in trmm field campaigns. *J. Atmos. Sci.* **59**: 3457–3491.

- Hu, Y., Vaughan, M., Liu, Z., Lin, B., Yang, P., Flittner, D., Hunt, B., Kuehn, R., Huang, J., Wu, D., Rodier, S., Powell, K., Treppe, C., and Winker, D. (2007). The depolarization attenuated backscatter relation: Calipso lidar measurements vs. theory. *Optics Express* **15**: 5327–5332.
- Hu, Y. X., Wielicki, B., Lin, B., Gibson, G., Tsay, S. C., Stammes, K., and Wong, T. (2000). delta-fit: A fast and accurate treatment of particle scattering phase functions with weighted singular-value decomposition least-squares fitting. *J. Quant. Spectrosc. Ra.* **65**: 681–690.
- Intrieri, J. M., Fairall, C. W., Shupe, M. D., Persson, P. O. G., Andreas, E. L., Guest, P. S., and Moritz, R. E. (2002). An annual cycle of Arctic surface cloud forcing at SHEBA. *J. Geophys. Res.* **107**: Art. No. 8039.
- Jäkel, E., Wendisch, M., Kniffka, A., and Trautmann, T. (2005). Airborne system for fast measurements of upwelling and downwelling spectral actinic flux densities. *Appl. Opt.* **44**: 434–444.
- Joseph, J. H., Wiscombe, W. J., and Weinman, J. A. (1976). Delta-Eddington approximation for radiative flux-transfer. *J. Atmos. Sci.* **33**: 2.452–2.459.
- Kay, J. E., L’Ecuyer, T., Gettelman, A., Stephens, G., and O’Dell, C. (2008). The contribution of cloud and radiation anomalies to the 2007 Arctic sea ice extent minimum. *Geophys. Res. Lett.* **35**: L08503.
- Key, J. R. and Intrieri, J. M. (2000). Cloud particle phase determination with the AVHRR. *J. Appl. Meteor.* **39**: 1797–1804.
- Key, J. R., Yang, P., Baum, B. A., and Nasiri, S. L. (2002). Parameterization of shortwave ice cloud optical properties for various particle habits. *J. Geophys. Res.* **107**: Art. No. 4181.
- King, M. D., Platnick, S., Yang, P., Arnold, G. T., Gray, M. A., Riedi, J. C., Ackerman, S. A., and Liou, K. N. (2004). Remote sensing of liquid water and ice cloud optical thickness and effective radius in the Arctic: Application of airborne multispectral MAS data. *J. Atmos. Oceanic Technol.* **21**: 857–875.
- Kinne, S. and Liou, K. N. (1989). The effects of the nonsphericity and size distribution of ice crystals on the radiative properties of cirrus clouds. *Atmos. Res.* **24**: 273–184.
- Klotzsche, S. and Macke, A. (2006). Influence of crystal tilt on solar irradiance of cirrus clouds. *Appl. Opt.* **45**: 1034–1040.
- Knap, W., Stammes, P., and Koelemeijer, R. (2002). Cloud thermodynamic-phase determination from near-infrared spectra of reflected sunlight. *J. Atmos. Sci.* **59**: 83–96.

- Knollenberg, R. G. (1976). Three new instruments for cloud physics measurements. In *Preprints Int. Conf. Cloud Physics*, pp. 545–561. Boulder, Amer. Meteor. Soc.
- Kokhanovsky, A. A., Rozanov, V. V., Nauss, T., Reudenbach, C., Daniel, J. S., Miller, H. L., and Burrows, J. P. (2006). The semianalytical cloud retrieval algorithm for SCIAMACHY - I. The validation. *Atmos. Chem. Phys.* **6**: 1905–1911.
- Korolev, A. and Field, P. R. (2008). The effect of dynamics on mixed-phase clouds: Theoretical considerations. *J. Atmos. Sci.* **65**: 66–86.
- Korolev, A. and Isaac, G. (2003). Phase transformation of mixed-phase clouds. *Quart. J. Roy. Meteor. Soc.* **129**: 19–38.
- Korolev, A. and Isaac, G. A. (2005). Shattering during sampling by OAPs and HVPS. Part I: Snow particles. *J. Atmos. Oceanic Technol.* **22**: 528–542.
- Korolev, A. and Mazin, I. (2003). Supersaturation of water vapor in clouds. *J. Atmos. Sci.* **60**: 2957–2974.
- Korolev, A. V., Isaac, G. A., Cober, S. G., Strapp, J. W., and Hallett, J. (2003). Microphysical characterization of mixed-phase clouds. *Quart. J. Roy. Meteor. Soc.* **129**: 39–65.
- Korolev, A. V., Isaac, G. A., and Hallett, J. (1999). Ice particle habits in Arctic clouds. *Geophys. Res. Lett.* **26**: 1.299–1.302.
- Korolev, A. V. and Mazin, I. P. (1993). Zones of increased and decreased droplet concentration in stratiform clouds. *J. Appl. Meteor.* **32**: 760–773.
- Korolev, A. V. and Strapp, J. W. (2002). Accuracy of measurements of cloud ice water content by the Nevzorov Probe. In *40th Aerospace Science Meeting & Exhibit*. Reno, Nevada, January 14-17.
- Korolev, A. V., Strapp, J. W., Isaac, G. A., and Nevzorov, A. N. (1998). The Nevzorov airborne hot-wire LWC-TWC probe: Principle of operation and performance characteristics. *J. Atmos. Oceanic Technol.* **15**: 1.495–1.510.
- Kylling, A., Stamnes, K., and Tsay, S.-C. (1995). A reliable and efficient two-stream algorithm for spherical radiative transfer: documentation of accuracy in realistic layered media. *J. Atmos. Chem.* **21**: 115–150.
- Lawson, R. P., Baker, B. A., Schmitt, C. G., and Jensen, T. L. (2001). An overview of microphysical properties of Arctic clouds observed in May and July 1998 during FIRE ACE. *J. Geophys. Res.* **106**: 14.989–15.014.
- Lee, J., Yang, P., Dessler, A. E., and Platnick, S. (2006). The influence of thermodynamic phase on the retrieval of mixed-phase cloud microphysical and optical properties in the visible and near-infrared region. *IEEE Geosci. Remote Sens. Lett.* **3**: 287–291.

- Liou, K. N. and Takano, Y. (1994). Light scattering by nonspherical particles: Remote sensing and climatic implications. *Atmos. Res.* **31**: 271–298.
- Macke, A. and Francis, P. N. (1998). The role of ice particle shapes and size distributions in the single scattering properties of cirrus clouds. *J. Atmos. Sci.* **55**: 2.874–2.883.
- Mayer, B. (1999). I3RC phase 1 results from the MYSTIC Monte Carlo model. In *Intercomparison of three-dimensional radiation codes: Abstracts of the first and second international workshops*, pp. 49–54. University of Arizona Press.
- Mayer, B. (2000). I3RC phase 2 results from the MYSTIC Monte Carlo model. In *Intercomparison of three-dimensional radiation codes: Abstracts of the first and second international workshops*, pp. 107–108. University of Arizona Press.
- Mayer, B. and Emde, C. (2007). Comment on "Glory phenomenon informs of presence and phase state of liquid water in cold clouds" by Anatoly N. Nevzorov. *Atmos. Res.* **84**: 410–419.
- Mayer, B. and Kylling, A. (2005). Technical note: The libRadtran software package for radiative transfer calculations - description and examples of use. *Atmos. Chem. Phys.* **5**: 1.855–1.877.
- Mayer, B., Schröder, M., Preusker, R., and Schüller, L. (2004). Remote sensing of water cloud droplet size distributions using the backscatter glory: A case study. *Atmos. Chem. Phys.* **4**: 1255–1263.
- McFarlane, S. A., Marchand, R. T., and Ackerman, T. P. (2005). Retrieval of cloud phase and crystal habit from Multiangle Imaging Spectroradiometer (MISR) and Moderate Resolution Imaging Spectroradiometer (MODIS) data. *J. Geophys. Res.* **110**: Art. No. D14201.
- McFarquhar, G. M. and Cober, S. G. (2004). Single-scattering properties of mixed-phase Arctic clouds at solar wavelengths: Impacts on radiative transfer. *J. Climate* **17**: 3.799–3.813.
- McFarquhar, G. M., Zhang, G., Poellot, M. R., Kok, G. L., McCoy, R., Tooman, T., Fridlind, A., and Heymsfield, A. J. (2007). Ice properties of single-layer stratocumulus during the Mixed-Phase Arctic Cloud Experiment: 1. Observations. *J. Geophys. Res.* **112**: D24201.
- Mie, G. (1908). Beiträge zur Optik trüber Medien, speziell kolloidaler Metallösungen. *Annalen der Physik, Vierte Folge* **25**: 377–445.
- Miles, N. L., Verlinde, J., and Clothiaux, E. E. (2000). Cloud droplet size distributions in low-level stratiform clouds. *J. Atmos. Sci.* **57**: 295–311.

- Minnett, P. J. (1999). The influence of solar zenith angle and cloud type on cloud radiative forcing at the surface in the Arctic. *J. Climate* **12**: 147–158.
- Mitchell, D. L. (2002). Effective diameter in radiation transfer: General definition, applications, and limitations. *J. Atmos. Sci.* **59**: 2330–2346.
- Morrison, H., Curry, J., and Khvorostyanov, V. (2005). A new double-moment microphysics parameterization for application in cloud and climate models. Part II: Single-column modeling of Arctic clouds. *J. Atmos. Sci.* **62**: 1678–1693.
- Morrison, H., Pinto, J. O., Curry, J. A., and McFarquhar, G. M. (2008). Sensitivity of modeled Arctic mixed-phase stratocumulus to cloud condensation and ice nuclei over regionally varying surface conditions. *J. Geophys. Res.* **113**: D05203.
- Murtagh, F. and Heck, A. (1987). *Multivariate Data Analysis*. Springer: 236 pp.
- Nakajima, T. and King, M. (1990). Determination of the optical thickness and effective particle radius of clouds from reflected solar radiation measurements. Part I: Theory. *J. Atmos. Sci.* **47**: 1878–1893.
- Nakajima, T. and Tanaka, M. (1988). Algorithms for radiative intensity calculations in moderately thick atmospheres using a truncation approximation. *J. Quant. Spectrosc. Radiat. Transfer* **40**: 51–69.
- Nicodemus, F., Richmond, J., Hsia, J., Ginsber, I. W., and Limperis, T. (1977). *Geometrical Considerations and Nomenclature for Reflectance*, vol. 160 of *NBS Monograph*. US Department of Commerce, Washington, D.C.: National Bureau of Standards.
- Olsson, P. Q., Harrington, J. Y., Feingold, G., Cotton, W. R., and Kreidenweis, S. M. (1998). Exploratory cloud-resolving simulations of boundary-layer Arctic stratus clouds Part I: Warm-season clouds. *Atmos. Res.* **48**: 573–597.
- Pearson, K. (1901). On lines and planes of closest fit to systems of points in space. *Philos. Mag.* **2**: 559–572.
- Petty, G. (2006). *A First Course in Atmospheric Radiation, 2nd Edition*. Sundog Publishing, Madison, Wisconsin: 460 pp.
- Pilewskie, P. and Twomey, S. (1987). Discrimination of ice from water in clouds by optical remote sensing. *Atmos. Res.* **21**: 113–122.
- Pinto, J. O. (1998). Autumnal mixed-phase cloudy boundary layers in the Arctic. *J. Atmos. Sci.* **55**: 2016–2038.
- Platnick, S. (2000). Vertical photon transport in cloud remote sensing problems. *J. Geophys. Res.* **105**: 22919–22935.

- Potter, J. (1970). The delta function approximation in radiative transfer theory. *J. Atmos. Sci.* **27**: 943–949.
- Prenni, A. J., Harrington, J. Y., Tjernstrom, M., DeMott, P. J., Avramov, A., Long, C. N., Kreidenweis, S. M., Olsson, P. Q., and Verlinde, J. (2007). Can ice-nucleating aerosols affect Arctic seasonal climate? *Bull. Amer. Meteor. Soc.* **88**: 541.
- Pruppacher, H. and Klett, J. (1997). *Microphysics of Clouds and Precipitation*. Kluwer Academic: 976 pp.
- Rabbette, M. and Pilewskie, P. (2001). Multivariate analysis of solar spectral irradiance measurements. *J. Geophys. Res.* **106**: 9685–9696.
- Rinke, A. and Dethloff, K. (1997). Simulation and validation of Arctic radiation and clouds in a regional climate model. *J. Geophys. Res.* **102**: 29833–29847.
- Rozwadowska, A. and Cahalan, R. F. (2002). Plane-parallel biases computed from inhomogeneous Arctic clouds and sea ice. *J. Geophys. Res.* **107**: 4384.
- Sassen, K. and Wang, Z. (2008). Classifying clouds around the globe with the CloudSat radar: 1-year of results. *Geophys. Res. Lett.* **35**: L04805.
- Schaepman-Strub, G., Schaepman, M. E., Painter, T. H., Dangel, S., and Martonchik, J. V. (2006). Reflectance quantities in optical remote sensing—definitions and case studies. *Remote Sens. Environ.* **103**: 27–42.
- Schweiger, A. and Key, J. (1994). Arctic ocean radiative fluxes and cloud forcing estimated from the ISCCP C2 cloud dataset, 1983–1990. *J. Appl. Meteorol.* **33**: 948–963.
- Serreze, M. C., Barrett, A. P., Slater, A. G., Steele, M., Zhang, J. L., and Trenberth, K. E. (2007). The large-scale energy budget of the Arctic. *J. Geophys. Res.* **112**: D11122.
- Shettle, E. (1989). Comments on the use of LOWTRAN in transmission calculations for sites with the ground elevated relative to sea level. *Appl. Opt.* **28**: 1451–1452.
- Shupe, M. D., Daniel, J. S., de Boer, G., Eloranta, E. W., Kollias, P., Long, C. N., Luke, E. P., Turner, D. D., and Verlinde, J. (2008a). A focus on mixed-phase clouds: The status of ground-based observational methods. *Bull. Amer. Meteor. Soc.* **89**: 1549.
- Shupe, M. D. and Intrieri, J. M. (2004). Cloud radiative forcing of the Arctic surface: The influence of cloud properties, surface albedo, and solar zenith angle. *J. Climate* **17**: 616–628.
- Shupe, M. D., Kollias, P., Persson, P. O. G., and McFarquhar, G. M. (2008b). Vertical motions in Arctic mixed-phase stratiform clouds. *J. Atmos. Sci.* **65**: 1304–1322.
- Shupe, M. D., Matrosov, S. Y., and Uttal, T. (2006). Arctic mixed-phase cloud properties derived from surface-based sensors at SHEBA. *J. Atmos. Sci.* **63**: 697–711.

- Shupe, M. D., Uttal, T., and Matrosov, S. Y. (2005). Arctic cloud microphysics retrievals from surface-based remote sensors at SHEBA. *J. Appl. Meteor.* **44**: 1544–1562.
- Slingo, A. (1990). Sensitivity of the Earth's radiation budget to changes in low clouds. *Nature* **343**: 49–51.
- Smedsrud, L. H., Sorteberg, A., and Kloster, K. (2008). Recent and future changes of the Arctic sea-ice cover. *Geophys. Res. Lett.* **35**: L20503.
- Stachlewska, I., Wehrle, G., Stein, B., and Neuber, R. (2004). Airborne Mobile Aerosol Lidar for measurements of Arctic aerosols. *Proceedings of 22nd International Laser Radar Conference (ILRC2004), ESA SP-561* **1**: 87–89.
- Stachlewska, I. S. (2006). *Investigation of tropospheric Arctic aerosol and mixed-phase clouds using airborne lidar technique*. Ph.D. thesis, University Potsdam.
- Stamnes, K., Tsay, S., Wiscombe, W., and Jayaweera, K. (1988). A numerically stable algorithm for discrete-ordinate-method radiative transfer in multiple scattering and emitting layered media. *Appl. Opt.* **27**: 2502–2509.
- Stephens, G., Vane, D., Boain, R., Mace, G., Sassen, K., Wang, Z., Illingworth, A., O'Connor, E., Rossow, W., Durden, S., Miller, S., Austin, R., Benedetti, A., Mitrescu, C., and the CloudSat Science Team (2002). The CloudSat mission and the A-train. *Bull. Amer. Meteorol. Soc.* **83**: 1771–1790.
- Sun, Z. and Shine, K. P. (1994). Studies of the radiative properties of ice and mixed-phase clouds. *Quart. J. Roy. Meteor. Soc.* **120**: 111–137.
- Takano, Y. and Liou, K.-N. (1989). Solar radiative transfer in cirrus clouds. Part I: Single-scattering and optical properties of hexagonal ice crystals. *J. Atmos. Sci.* **46**: 1–19.
- Takano, Y. and Liou, K. N. (1995). Radiative-transfer in cirrus clouds. Part III. Light scattering by irregular ice crystals. *J. Atmos. Sci.* **52**: 818–837.
- Trenberth, K. E., Fasullo, J. T., and Kiehl, J. (2009). Earth's global energy budget. *accepted for Bull. Amer. Meteorol. Soc.* .
- Turner, D. D., Ackerman, S. A., Baum, B. A., Revercomb, H. E., and Yang, P. (2003). Cloud phase determination using ground-based AERI observations at SHEBA. *J. Appl. Meteor.* **42**: 701–715.
- Verlinde, J., Harrington, J. Y., McFarquhar, G. M., Yannuzzi, V. T., Avramov, A., Greenberg, S., Johnson, N., Zhang, G., Poellot, M. R., Mather, J. H., Turner, D. D., Eloranta, E. W., Zak, B. D., Prenni, A. J., Daniel, J. S., Kok, G. L., Tobin, D. C., Holz, R., Sassen, K., Spangenberg, D., Minnis, P., Tooman, T. P., Ivey, M. D., Richardson, S. J., Bahrmann, C. P., Shupe, M., DeMott, P. J., Heymsfield, A. J., and Schofield, R. (2007). The mixed-phase Arctic cloud experiment. *Bull. Amer. Meteor. Soc.* **88**: 205.

- Wagner, T., Burrows, J. P., Deutschmann, T., Dix, B., von Friedeburg, C., Friess, U., Hendrick, F., Heue, K. P., Irie, H., Iwabuchi, H., Kanaya, Y., Keller, J., McLinden, C. A., Oetjen, H., Palazzi, E., Petritoli, A., Platt, U., Postylyakov, O., Pukite, J., Richter, A., van Roozendaal, M., Rozanov, A., Rozanov, V., Sinreich, R., Sanghavi, S., and Wittrock, F. (2007). Comparison of box-air-mass-factors and radiances for Multiple-Axis Differential Optical Absorption Spectroscopy (MAX-DOAS) geometries calculated from different UV/visible radiative transfer models. *Atmos. Chem. Phys.* **7**: 1809–1833.
- Warren, S. G. and Brandt, R. E. (2008). Optical constants of ice from the ultraviolet to the microwave: A revised compilation. *J. Geophys. Res.* **113**: Art. No. D14220.
- Wegener, A. (1911). *Thermodynamik der Atmosphäre*. J. A. Barth Verlag: 311 pp.
- Wendisch, M. (2002). *Absorption of Solar Radiation in the Cloudless and Cloudy Atmosphere*. Habilitation thesis, 174 pp., Univ. of Leipzig, Leipzig, Germany.
- Wendisch, M., Keil, A., and Korolev, A. (1996). FSSP characterization with monodisperse water droplets. *J. Atmos. Oceanic Technol.* **13**: 1152–1165.
- Wendisch, M., Keil, A., Müller, D., Wandinger, U., Wendling, P., Stifter, A., Petzold, A., Fiebig, M., Wiegner, M., Freudenthaler, V., Armbruster, W., von Hoyningen-Huene, W., and Leiterer, U. (2002). Aerosol-radiation interaction in the cloudless atmosphere during LACE 98. Part 1: Measured and calculated broadband solar and spectral surface insulations. *J. Geophys. Res.* **107**: Art. No. 8124.
- Wendisch, M. and Mayer, B. (2003). Vertical distribution of spectral solar irradiance in the cloudless sky: A case study. *Geophys. Res. Lett.* **30**: Art. No. 1183.
- Wendisch, M., Müller, D., Schell, D., and Heintzenberg, J. (2001). An airborne spectral albedometer with active horizontal stabilization. *J. Atmos. Oceanic Technol.* **18**: 1856–1866.
- Wendisch, M., Pilewskie, P., Jäkel, E., Schmidt, S., Pommier, J., Howard, S., Jonsson, H. H., Guan, H., Schroder, M., and Mayer, B. (2004). Airborne measurements of areal spectral surface albedo over different sea and land surfaces. *J. Geophys. Res.* **109**: Art. No. D08203.
- Wendisch, M., Pilewskie, P., Pommier, J., Howard, S., Yang, P., Heymsfield, A. J., Schmitt, C. G., Baumgardner, D., and Mayer, B. (2005). Impact of cirrus crystal shape on solar spectral irradiance: A case study for subtropical cirrus. *J. Geophys. Res.* **110**: Art. No. D03202.
- Wendisch, M., Yang, P., and Pilewskie, P. (2007). Effects of ice crystal habit on thermal infrared radiative properties and forcing of cirrus. *J. Geophys. Res.* **112**: D03202.

- Wieliczka, D. M., Weng, S. S., and Querry, M. R. (1989). Wedge shaped cell for highly absorbent liquids - Infrared optical-constants of water. *Appl. Opt.* **28**: 1714–1719.
- Winker, D. M., Hunt, W. H., and McGill, M. J. (2007). Initial performance assessment of CALIOP. *Geophys. Res. Lett.* **34**: Art. No. L19803.
- Winker, D. M., Pelon, J., and McCormick, M. P. (2003). The CALIPSO mission: Spaceborne lidar for observation of aerosols and clouds. *Proc. SPIE* **4893**: 1–11.
- Wiscombe, W. (1977). The delta-M method: Rapid yet accurate radiative flux calculations for strongly asymmetric phase functions. *J. Atmos. Sci.* **34**: 1408–1421.
- Wyser, K. (1999). Ice crystal habits and solar radiation. *Tellus Series A-Dynamic Meteorology And Oceanography* **51**: 937–950.
- Yamanouchi, T., Treffeisen, R., Herber, A., Shiobara, M., Yamagata, S., Hara, K., Sato, K., Yabuki, M., Tomikawa, Y., Rinke, A., Neuber, R., Schumacher, R., Kriews, M., Strom, J., Schrems, O., and Gernandt, H. (2005). Arctic Study of Tropospheric Aerosol and Radiation (ASTAR) 2000: Arctic haze case study. *Tellus B* **57**: 141–152.
- Yang, P. and Liou, K. N. (1996a). Finite-difference time domain method for light scattering by small ice crystals in three-dimensional space. *J. Opt. Soc. Am. A.* **13**: 2.072–2.085.
- Yang, P. and Liou, K. N. (1996b). Geometric-optics-integral-equation method for light scattering by nonspherical ice crystals. *Appl. Opt.* **35**: 6.568–6.584.
- Yang, P., Wei, H. L., Huang, H. L., Baum, B. A., Hu, Y. X., Kattawar, G. W., Mishchenko, M. I., and Fu, Q. (2005). Scattering and absorption property database for nonspherical ice particles in the near- through far-infrared spectral region. *Appl. Opt.* **44**: 5512–5523.
- Yoshida, Y. and Asano, S. (2005). Effects of the vertical profiles of cloud droplets and ice particles on the visible and near-infrared radiative properties of mixed-phase stratocumulus clouds. *J. Meteor. Soc. Japan* **83**: 471–480.
- Zhang, Y., Macke, A., and Albers, F. (1999). Effect of crystal size spectrum and crystal shape on stratiform cirrus radiative forcing. *Atmos. Res.* **52**: 59–75.
- Zuidema, P., Baker, B., Han, Y., Intrieri, J., Key, J., Lawson, P., Matrosov, S., Shupe, M., Stone, R., and Uttal, T. (2005). An Arctic springtime mixed-phase cloudy boundary layer observed during SHEBA. *J. Atmos. Sci.* **62**: 160–176.